

141p.

42 141

MECHANICAL

N64-21465

CODE-1 cat 17

TECHNOLOGY

INCORPORATED

OTS PRICE

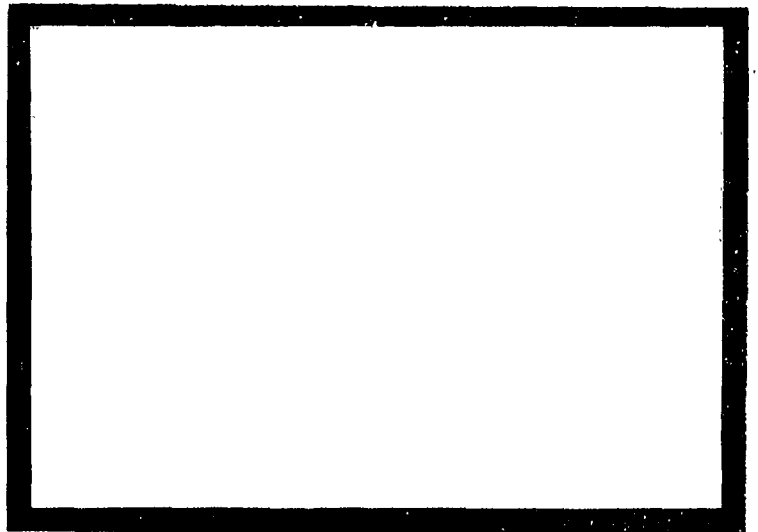
XEROX

\$

MICROFILM

\$

11.00 pd
none



CASE COPY

NOTICE

This report was prepared as an account of Government sponsored work. Neither the United States, nor the National Aeronautics and Space Administration (NASA), nor any person acting on behalf of NASA:

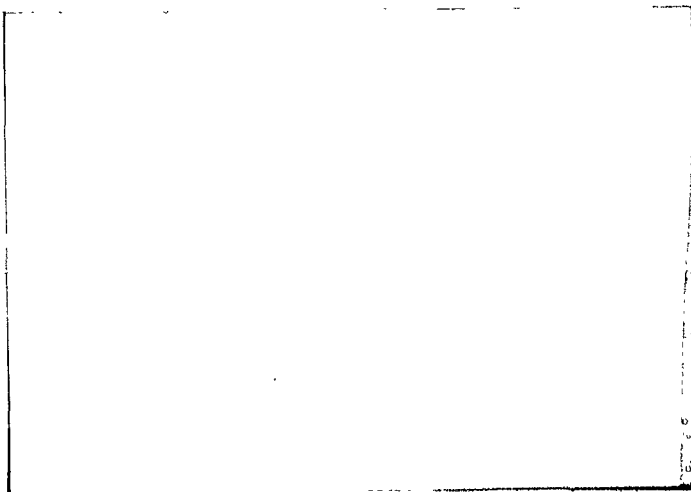
- A.) Makes any warranty or representation, expressed or implied, with respect to the accuracy, completeness, or usefulness of the information contained in this report, or that the use of any information, apparatus, method, or process disclosed in this report may not infringe privately owned rights; or
- B.) Assumes any liabilities with respect to the use of, or for damages resulting from the use of any information, apparatus, method or process disclosed in this report.

As used above, "person acting on behalf of NASA" includes any employee or contractor of NASA, or employee of such contractor, to the extent that such employee or contractor of NASA, or employee of such contractor prepares, disseminates, or provides access to, any information pursuant to his employment or contract with NASA, or his employment with such contractor.

Requests for copies of this report should be referred to:

National Aeronautics and Space Administration
Office of Scientific and Technical Information
Washington 25, D. C.

Attention: AFSS-A



2603

MECHANICAL TECHNOLOGY INC.
968 Albany-Shaker Rd.
Latham, N.Y.

MTI 64TR19
ANALYSIS OF TURBULENT LUBRICATION
Volume 1
THE STATIC AND DYNAMIC PROPERTIES OF JOURNAL
BEARINGS IN LAMINAR AND TURBULENT REGIMES
(Vol. 1 of Final Report on NASA
Contract NAS-w-771)


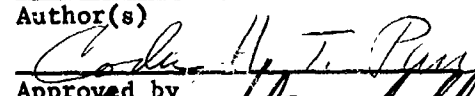

by

F. K. Orcutt
E. B. Arwas

ANALYSIS OF TURBULENT LUBRICATION
Volume 1
THE STATIC AND DYNAMIC PROPERTIES OF JOURNAL
BEARINGS IN LAMINAR AND TURBULENT REGIMES

by

F. K. Orcutt
E. B. Arwas

 E. B. Arwas
Author(s)

Approved by

Approved by

Prepared for

NATIONAL AERONAUTICS AND SPACE ADMINISTRATION

Prepared under

NASA Contract NAS w - 771

Technical Manager
NASA - Lewis Research Center
Space Electric Power Office
Joseph P. Joyce
Robert T. Wainwright

ABSTRACT

21465

Steady state and dynamic characteristics of two basic journal bearing geometries have been obtained both theoretically and experimentally, in laminar and super-laminar flow regimes. This data covers the ranges of eccentricity ratios up to 0.9 and of Reynolds Numbers up to 13,400. Comparison of the theoretical and experimental data is presented to check the validity of turbulent lubrication theory. The parameters investigated include: steady state load, attitude angle, film pressure distribution, fluid film stiffness, fluid film damping, and dynamic force and displacement orbits as functions of journal eccentricity and fluid film Reynolds Number.

author

TABLE OF CONTENTS

i

FOREWORD	ii
I. INTRODUCTION	1
II. SUMMARY CONCLUSIONS AND RECOMMENDATIONS	2
III. CALCULATED JOURNAL BEARING DESIGN CHARTS	4
IV. DYNAMIC LOAD BEARING APPARATUS	6
1. Mechanical Features of Apparatus	6
2. Instrumentation	9
V. BEARING STATIC LOAD PROPERTIES	13
1. Partial Arc Bearing Static Load Capacity	13
2. 360 Degree Bearing Static Load Capacity	14
3. Bearing Film Pressure	15
VI. PROCEDURE FOR DETERMINING BEARING DYNAMIC PROPERTIES	17
VII. MEASUREMENT OF BEARING DYNAMIC PROPERTIES	20
1. Laminar Flow Results	20
2. Partial Arc Bearing Results in Turbulent Flow Regime ..	21
3. Full Cylindrical Bearing in Turbulent Regime	24
4. Experiments with Counter Rotating Load	25
VIII. DISCUSSION OF DYNAMIC LOAD RESULTS	28
APPENDIX 1:	30
1. Nomenclature	30
2. Introduction	32
3. Stiffness and Damping Coefficients of a Journal Bearing	34
4. Numerical Solution of the Incompressible Lubrication : Equation	37
APPENDIX 2	45
REFERENCES	51
FIGURES	

Foreword

In classical analysis of fluid bearings, it is assumed that the lubricant flow in the clearance space is laminar. This is generally true of conventional bearings which have small clearance (of the order of 10^{-3} inches) and which are lubricated with hydrocarbon oils whose kinematic viscosity is high (of the order of 10^{-2} to 10^{-1} in²/sec).

In recent years, however, there have been an increasing number of applications where, due to high speed operation and use of unconventional, low viscosity lubricants, the bearing clearance flow is in the super-laminar regime. These applications have generally been associated with process fluid lubrication, where the cycle fluid is used also to lubricate the bearings of the system. Process Fluid lubrication is sometimes necessary because environmental conditions, such as extremes of temperature or radio-activity preclude the use of a hydrocarbon oil system for lubrication. In other cases, process fluid lubrication is used in order to remove a contamination hazard and/or to achieve the potential gains in efficiency, compactness and reliability that are made possible by elimination of an auxilliary fluid system and of cycle fluid to oil seals.

An important application of process fluid lubrication is Rankine Cycle turbo-machinery for dynamic power conversion in space vehicles. Such turbo-machinery is now under development, using mercury and alkali metals as cycle fluids. Rational design data for super-laminar flow bearings is necessary to prevent costly trial and error bearing development for this turbo-machinery and to allow selection of optimum bearing designs.

The program reported here was undertaken to investigate journal bearing performance in the super-laminar flow regime. Emphasis in the investigations was placed on the following:

1. Dynamic properties of journal bearings in super-laminar regime.
2. Fluid film phenomena in super-laminar regime.

Super-laminar flow occurs in high speed bearings. The problems encountered are therefore those associated with rotor bearing dynamics such as:

- a) rotor-bearing critical speeds
- b) fluid film response to dynamic loads
- c) fluid film instabilities

rather than with steady state load capacity. Thus, steady state data is not sufficient for design of high speed rotating machinery. The response of the fluid film to dynamic loads must also be defined. In the investigation that is reported here the stiffness and damping coefficients (as well as steady state load capacity and attitude angles) of basic bearing geometries were computed from theory and measured in a specially constructed test rig.

The starting part of the theoretical investigations was the turbulent lubrication equation that had previously been derived (Ref.4). Extensive comparisons were made between theoretical prediction and experimental findings in order to establish a level of confidence for the theoretical analysis of turbulent lubrication. In all parts of this study, the theoretical and experimental investigations in super-laminar flow regime were preceded by similar investigations in the well understood laminar flow regime. These preliminary laminar flow studies provided early verifications of the test rig, instrumentation and experimental procedure.

The conclusion of this work is that the turbulent lubrication theory that was derived in Ref. 4 predicts journal bearing performance in super-laminar flow regimes quite well. Equally good agreement was obtained when comparing turbulent lubrication theory with experimental data in super-laminar flow regime, as was obtained between laminar flow theory and tests data in laminar regime. Thus, it is now possible to proceed with generation of design data for optimized bearing configurations for high speed, low viscosity operation. Optimization of design is particularly important here to avoid fluid film instabilities and to minimize the power losses due to the sharp rise in friction that accompanies transition to super-laminar operation.

This work, including a set of design charts for two basic bearing geometries in laminar and super-laminar regimes (up to a Reynolds Number of 13000), is described in this volume of the final report.

The second part of the work recently completed, was concerned with detailed study of the fluid film phenomena in superlaminar regime. Super-laminar flow in journal bearings is complicated by the fact that there are two distinct modes of such flow. The first is vortex flow that occurs in an annular gap between a rotating inner cylinder and a stationary outer one. Above a critical value of Reynolds number which, for a concentric annulus, is given by:

$$Re_{crit.} = \left(\frac{VC}{\nu}\right)_{crit.} = 41.1 \sqrt{\frac{R}{C}}$$

where:

Re = Reynolds Number
 V = Surface speed of shaft (in./sec)
 C = Radial clearance (in.)
 ν = Kinematic viscosity (in²/sec)
 R = Shaft radius (in) ,

pairs of torroidal vortices are formed in the clearance space due to centrifugal forces on the fluid. Vortex formation is accompanied by a sharp rise in friction. While this is not a true hydrodynamic instability, it produces, similar effect, when occurring in a journal bearing, i.e. high friction, increased load capacity and higher attitude angles. The rotation speed at which vortices are formed is affected by both circumferential and axial pressure gradients and they can be inhibited by a strong axial flow.

Fully developed turbulence, on the other hand, will set in when:

$$\frac{Vh}{\nu} > 1000 \text{ to } 1500$$

where h = film thickness (in.)

Thus, depending on the value of the clearance ratio $\left(\frac{C}{R}\right)$, either vortex flow or fully developed turbulence can first occur. In addition, under eccentric conditions the bearing (i.e. when the journal center is displaced relative to the bearing center due to an imposed load), both the film thickness and

the pressure gradients vary around the annular space such that different flow regimes (laminar, vortex and true turbulence) may occur in different regions of the film.

In order to better define the complex, physical conditions in super-laminar bearing films and to define the ranges of applicability of the laminar and turbulent theories, a study of the film phenomena was conducted. The clearance used in these tests was much larger than conventional bearing clearances, to permit visual study. Accurate torque measurements were used to detect transition speeds as a function of eccentricity and axial flow. Visual studies were also made of the flow in the different regimes. In particular, accurate determination of friction torque was obtained for Reynolds Numbers up to 40,000 and eccentricity ratios up to 0.89. This work is described in the second volume of the final report. A motion picture record of the visual studies of vortex flow and turbulence in annular films was also made and issued to N.A.S.A. as part of the reporting on this program.

I. INTRODUCTION

Prior to the investigation reported here, there had been only very limited accurate experimental work conducted with journal bearings operating in super-laminar regime (Refs. 1,2 and 3) and there had been no published test data on performance of such bearings under dynamic loads. Thus, it was not possible to properly assess the validity of turbulent lubrication theory from which rational design data could be obtained for journal bearings operating at high speed with low kinematic viscosity lubricants.

In the investigation reported here, the steady state and dynamic performance of basic bearing configurations were both determined experimentally and calculated using the eddy viscosity, turbulent lubrication theory (Ref. 4). The major part of the work was concerned with dynamic behavior of the bearings, since this is the critical area in high speed journal bearing operation. The dynamic properties of bearings permit calculation of rotor response to dynamic loads, rotor-bearing critical speeds and fluid film instabilities.

The computations and tests were limited to two basic bearing configurations:

- a) plain circular,
- b) 100° , centrally loaded, partial arc,

in order to insure that comparison between theory and test could be accurately made over a wide range of Reynolds Numbers. Design charts have been prepared for these bearings for steady-state (load and attitude angle vs eccentricity ratio and Reynolds Number) and dynamic (stiffness and damping coefficients vs Sommerfeld Number and Reynolds Number) operation.

The tests were made for the following conditions:

Bearing:	Arc Length, Degrees	360	100	100
	L/D	1	1	1
	C/R, in/in	4×10^{-3}	2×10^{-3}	4×10^{-3}
	Speed	2000 to 11,000 rpm		
	Unidirectional Load	to 1000 lb		
	Rotating Load	to 100 lb		
	Rotating Load Frequency	2000 to 24,000 cpm		
	Lubricant	0.65 c.s. silicone (77F)		
	viscosity temperature coefficient	$(1 - \frac{\text{viscosity at } 210\text{F}}{\text{viscosity at } 100\text{F}}) = 0.31$		

II SUMMARY, CONCLUSIONS AND RECOMMENDATIONS

The steady state and dynamic characteristics of two basic journal bearing configurations have been analyzed both theoretically and experimentally, with laminar and super-laminar flow in the fluid film.

The analysis and comparisons between theory and test were made for the following parameters:

1. Steady state load vs Eccentricity ratio and Reynolds number.
2. Steady state attitude angle vs Eccentricity ratio and Reynolds number.
3. Steady state pressure distribution vs Excentricity ratio and Reynolds number.
4. Fluid Film Stiffness vs Sommerfeld Number and Reynolds Number.
5. Fluid Film Damping vs Sommerfeld Number and Reynolds Number.
6. Dynamic Force and displacement orbits for the range of eccentricity ratios and Reynolds numbers of the tests.

The investigations were carried to eccentricity ratios of 0.9 and Reynolds numbers of 13,400.

It is concluded from this work that the present theory of turbulent lubrication predicts the steady state and dynamic journal bearing performance in super-laminar regions with good accuracy. In fact, the results have shown that agreement between turbulent bearing theory and super-laminar film bearing tests was equally as good as that between laminar theory and laminar flow tests. Since the present turbulent lubrication theory is free of factors which are functions of bearing geometry, it is felt that this theory can now be used to generate design data for the more complex bearing geometries that should be used for high speed turbo-machinery operating with low viscosity fluids. In such turbo-machinery, the dynamic characteristics of the bearings are particularly important since the critical problem areas are those of rotor-bearing dynamics, rather than of steady state load capacity.

Continued work on dynamics of rotor-bearing systems with super-laminar flow in the bearing film should now be conducted in the following areas:

1. Theoretical and experimental analysis of pressure generation in the vortex flow region, since this aspect of super-laminar bearing operation is still improperly defined.
2. Design and test of practical bearings for high speed, low viscosity operation. Such bearings need to be inherently stable (or at least have a threshold of stability which is higher than the maximum operating speed). Also, in view of the sharp rise in fluid film friction that accompanies transition to super-laminar flow, optimum design has to be selected from the standpoint of minimum friction power loss. This is a critical factor in future Rankine Cycle turbomachinery for dynamic power conversion in space vehicles, since poorly designed bearings can consume a significant fraction of the power output. In addition, to reduced system efficiency, such high friction power loss poses problems of life and reliability due to high local temperatures and temperature gradients.
3. Comparison of the calculated and measured steady state and dynamic performance of such optimized bearings, in order to insure that the theory and design calculation methods that are available correctly predict performance of complex bearing geometries in super-laminar flow regions.
4. Preparation of design charts for the range of practical bearing geometries and sizes useful for space power turbo-machinery.

III. CALCULATED JOURNAL BEARING DESIGN CHARTS

The turbulent lubrication equation was previously derived in Ref. 4. The mathematical analysis leading to it was also given in an Appendix of Ref. 5 and will not be repeated here. The procedure for the numerical integration of this equation, to calculate pressure distribution, load capacity and attitude angle as well as the stiffness and damping coefficients, is described in Appendix 1 of this report. This Appendix also discusses the dynamic characteristics of journal bearings and the use of these in rotor-bearing dynamics analysis.

In this program, the calculations were made for the following bearing geometries:

1. 360° , plain circular, $L/D = 1$
2. 100° arc, centrally loaded, $L/D = 1$

for comparison with the tests data.

The results of the calculations are plotted in dimensionless form in Figs. 1 through 32. The symbols used in the charts are defined in the Nomenclature of Appendix 1.

Figures 1 and 17, show, respectively, the eccentricity ratio-attitude angle loci for the full circular and the 100° arc bearings. These figures show that there is an increase in attitude angle that accompanies transition to turbulent flow in the film, thereafter however the rate of increase of the attitude angle with Reynolds number is quite small.

Figures 3 through 17 and 19 through 32 show the stiffness and damping coefficients for the full circular and the 100° arc bearings respectively, as functions of the steady state Sommerfeld Number and the mean clearance Reynolds Number. As shown in Appendix 1, four stiffness coefficients, (K_{xx}, K_{xy}, K_{yx} and K_{yy}) and four damping coefficients (C_{xx}, C_{xy}, C_{yx} and C_{yy}) are required to define the response of the fluid film forces to dynamic loads. The stiffness coefficients are the gradients of the fluid film

force vs journal center displacement curves, calculated about the steady state position of the journal center. The damping coefficients are the gradients of the fluid film force vs journal center velocity curves, also calculated about the steady state position of the journal center.

It should be noted that eight coefficients are required because the change in fluid film force that accompanies a displacement or velocity of the journal center is not co-linear with the displacement or velocity. Thus, if the journal center is displaced along any given axis (or if a velocity is imparted to it), the resulting change in the fluid film force will have components both parallel and normal to the direction of the displacement (or velocity).

The stiffness and damping coefficients plotted in Figs. 3 through 18 and 19 through 32 have been calculated for the (x,y) coordinate axes shown in Fig. 79, where the x axis is parallel to the direction of the steady state load and the y axis is normal to it. In each coefficient, the first subscript defines the direction of the fluid film force, while the second subscript defines the direction of the displacement or velocity. Thus,

$$\begin{aligned} \bar{K}_{xx} &= \frac{C}{W} K_{xx} = \frac{C}{W} \frac{\partial F_x}{\partial x} & ; & & \bar{C}_{xx} &= \frac{C\omega}{W} C_{xx} = \frac{C\omega}{W} \frac{\partial F_x}{\partial \dot{x}} \\ \bar{K}_{xy} &= \frac{C}{W} K_{xy} = \frac{C}{W} \frac{\partial F_x}{\partial y} & ; & & \bar{C}_{xy} &= \frac{C\omega}{W} C_{xy} = \frac{C\omega}{W} \frac{\partial F_x}{\partial \dot{y}} \end{aligned}$$

and, similarly, for the other coefficients.

IV. DYNAMIC LOAD BEARING APPARATUS

1. Mechanical Features of Apparatus

The basic mechanical arrangement of the apparatus consists of one support bearing and one test bearing each located near the ends of a long shaft. The shaft is driven from the support bearing end and rotating and uni-directional loads are applied at the test bearing end. Figure 33 shows the general layout of the main components and Fig. 34 is a photograph of the completed apparatus.

It is desirable to work with a relatively large diameter test bearing from consideration of access for instrumentation, low power consumption to obtain a given concentric film Reynold's number for a bearing of fixed C/R, and to obtain amplitudes of shaft motion which can be accurately measured with readily available instrumentation. A long span between test and support bearings is desirable to maintain alignment of the shaft and test bearing as the shaft center moves around the bearing clearance, and to minimize interaction of dynamic effects between bearings. A four inch diameter test bearing with a span between bearings of 10 times shaft diameter was chosen as representing a good balance between these considerations and those of overall apparatus size, the magnitude of required applied loads, and shaft stiffness.

Intepretation of the data from this apparatus could be made easier by placing the test bearing at the center of percussion of the shaft so that there will be no rotating load reaction forces on the support bearing. Determination of the forces acting on the test bearing is greatly simplified if this is possible within the framework of other practical design considerations. From a brief analysis it was apparent that it was not practically possible to locate the test bearing at the center of percussion. Consequently arrangements were made to measure force at the test bearing directly.

The natural frequencies of the shaft as a spring supported rigid beam and as a simply supported flexible beam were calculated. The simply support flexible

shaft natural frequency is about 100,000 cpm, nearly an order of magnitude above the maximum operating speed. From estimated values of test and support bearing stiffness, there should be one and perhaps two rigid body critical frequencies in the operating speed range.

The main drive for the shaft is a 1770 to 11,500 rpm, 7-1/2 HP variable speed electric drive which is coupled to the shaft at the support bearing end through a dynamically balanced, flexible disk coupling. The support bearing consists of a preloaded pair of super precision, 107 size, angular contact ball bearings. If the shaft is perfectly aligned when in the center of the test bearing, a 10 mil clearance radius represents a misalignment angle of less than 0.05 degrees so there should be very little restraint to shaft motion in the test bearing from the support bearing end. The force required to move the shaft around the test bearing clearance with no rotation is less than 1-1/2 lbs. variation about the 50 lbs. required to just lift the shaft off the bottom of the bearing. The test bearing pedestal is designed to accept bearings with L/D of up to 1-1/2. In all cases the bearing outer envelope is a cylinder of 6 inches O.D. The test bearing is made of leaded bronze and is held in the pedestal by two force gages oriented at right angles which force the bearing under preload against two short locating arcs positioned opposite each force gage in the pedestal. That is, the bearing is held at four points in two orthogonal planes with one force gage located at the axial mid-point and one locating arc opposite and extending over the entire length of the bearing in each plane.

Alignment of the test and support bearings is obviously a matter of great importance in the design and construction of an apparatus of this type. The base plate on which the bearing pedestals are mounted was planed flat within 0.002 inch total and a straight edge keyway was cut into its top surface extending over its full length. Matching keyways are cut into the bottom surface of the bearing pedestals and the bearing locating surfaces are reinforced from the bottom and keyway surfaces. Alignment is checked each time the bearing is changed by several methods including dial indicating from the shaft to the bearing face which is machined on the same setting as the bore, and comparison

of the clearance circle as measured by the proximity sensors while rolling the shaft in the bearing with the clearance determined from separate measurements of shaft and bearing diameters. There has been no difficulty in obtaining bearing face runouts of less than 0.0005 TIR and no measurable departure from expected clearances.

The shaft is made of steel tubing with shrink fitted end sections, Fig. 33, The shaft O.D. is coated with flame plated tungsten carbide in the test bearing area to avoid damage to the shaft in the event of a test bearing failure. Finish specifications for the shaft include concentricity of test bearing and support bearing diameters of 0.0002 inch TIR, roundness and uniformity of diameter in the test bearing area within 0.0002 inch total and concentricity of all remaining diameters including the tubing bore of 0.001 inch TIR. The shaft was balanced first in a balance stand at low speeds and then in place in the apparatus of speeds up to 11,000 rpm. Fortunately, the unbalance was small, appeared to be evenly distributed along the shaft, and acted in the same direction at all planes. Evidently it was caused by slight non-concentricity of the tubing bore and O.D. This made it comparatively easy to distribute the corrective weight changes along the shaft length with about the same distribution as the original unbalance. Failure to do so would result in shaft bending moments so that the shaft could be well balanced at one speed and badly out of balance at higher and lower speeds.

Unidirectional, downward load is applied to the inboard ball bearing at the test bearing end of the shaft, Fig.33 by a cable which goes around a pulley to a large, low spring rate (125 lb/in) compression spring on the test bearing end of the apparatus base. Rotating load is applied in one of two ways. For independent control of load frequency and direction, unbalance weights are attached to the housing mounted on the outer race of the outboard ball bearing, Fig.1, and the housing and outer race are driven in either direction by a small universal electric motor through a flexible disk coupling. Synchronous unbalance load is applied by replacing the rotating load bearing with a disk to which unbalance weights can be attached.

Lubricant is supplied to the test bearing by an internal gear pump driven by an air motor for variable volume delivery. The pump is submerged in the sump which is equipped with a heater. A cold water to oil heat exchanger is located in the delivery line with temperature measuring instrumentation at its outlet. Temperature is measured also at the trailing edge of the partial arc bearings, and at the same position on the 360 degree bearing, by a thermocouple flush with the bearing surface. Lubricant temperature rise from inlet to trailing edge is normally quite small and the temperature midway between is taken for determination of lubricant viscosity.

Initially the partial arc bearing design consisted of a cylinder with its I.D. relieved except for the bearing arc. Preliminary experiments showed that there was a substantial effect of velocity head generated in the relief area ahead of the step at the bearing inlet. Attitude angles in excess of 90 degrees were obtained at most eccentricity ratios below about .7. To correct this, relief slots were machined into both sides of the bearing under the bearing arc so that any pressure at inlet is relieved by bypass flow to the arc exit. Figure 35 is a photograph of modified partial arc bearing which is also equipped with taps for pressure measurement. The bypass slots extend into with 1/2 inch of the bearing centerline so the bearing pad is held by a 1 inch wide web at the centerline.

2. Instrumentation

To obtain the static and dynamic properties of the test bearing the following measurements were desired:

- (a) Locus of the shaft center within the bearing clearance.
- (b) Dynamic component of force applied by the shaft to the bearing.
- (c) Dynamic motion of the shaft at test bearing and support bearing ends.
- (d) Steady state and rotating load magnitude.
- (e) Markers to indicate when the dynamic load vector is in each of two known directions.
- (d) Oil film pressures.
- (e) Shaft and dynamic load speeds.

Eddy current displacement probes were used for shaft locus measurements. Probes were located to measure vertical and horizontal displacement at both ends of the test bearing with outputs of the probes in the same plane averaged by summing amplifiers to effectively eliminate nonlinearity in dynamic response at very high eccentricities caused by bending of the shaft. Probes were also located at the support bearing end of the shaft so the overall shaft motion could be determined. The displacement probes were calibrated in a bench micrometer fixture with direct reading divisions of 1 micron using same material as the shaft is made of for the reference surface. The sensitivity of all probes was adjusted to give matched outputs of 0.004 inches \pm 0.0001 inches per volt. The displacement probes at the test bearing are located in special mounting rings at either end of the bearing housing, outboard of the seal and scavenging rings, where effects of temperature change are minimal and the gap between probe tip and reference surface is free of lubricant.

The force gages used to hold the test bearing in place and measure the dynamic force transmitted to the bearing from the shaft were piezoelectric crystal gages. The high stiffness, 5×10^6 lb/in and great sensitivity to dynamic load changes, 10mv/lb output, together with high static load capacity, 5000 lbs., of these gages fitted them extremely well for this application. The force gages were calibrated by applying known loads in known directions to the shaft through the steady state load bearing with the shaft rotating and recording the reaction on the oscilloscope.

Displacement and force measurements were displayed on an oscilloscope with horizontal and vertical components fed into the x-y axis. Shaft center locus within the test bearing clearance is displayed at all times on one oscilloscope. Any of the two sets of displacement measurements or one set of force measurements can be switched onto a second oscilloscope with AC coupling and high gain to measure dynamic components. Variable electronic filters set for band pass operation are placed ahead of the inputs to the oscilloscope used for measurement of dynamic components. A low pass filtering operation is needed to eliminate high frequency random fluctuation from the signal which

are caused by small inhomogenities or stray magnetic fields in the shaft which were not eliminated by a demagnetization treatment. The high pass operation is needed to reject the fluctuation caused by limited amplitude fractional frequency whirl which exists over part of the operating range. When displayed on the x and y axis of the scope, the characteristic force or displacement locus pattern is an ellipse. This ellipse can be described completely if the x and y coordinates of two points which are separated by a known angle are given. The two magnetic pickups which mark the passage of the rotating load vector are used to indicate measurement points of known angular separation. This is done either by superimposing the pickup outputs onto the force or displacement signals briefly to mark the measurement positions on the ellipse or by feeding the amplified pickup output onto the scope z axis to momentarily brighten the trace at the measurement position.

There is some interaction of the horizontal and vertical force gages for the mounting method which was used. That is, a vertically directed force will result in some reaction from the horizontal gage also so that the direction indicated on the oscilloscope is at a small angle to the vertical, about 15 degrees. This is caused by elastic deflections of the bearing and housing and by the fact that the gages are sensitive to shear loading. According to calibration experiments, the effect is uniform for all directions of force application so correction is made simply by shifting the coordinates on the oscilloscope screen by the correct angle to bring the reference and indicated directions into conformity.

Unidirectional load magnitude was determined from measured deflection of the load spring which was calibrated in a universal test machine. Rotating load magnitude is determined from unbalance mass, radius of the point of attachment to the shaft and frequency of rotation. Shaft speed and load rotation speed were measured by a frequency meter with magnetic pickups sensing set screw markers as the input. Magnetic pickups were used also to mark the precise time at which the rotating load was in each of two orthogonal positions by sensing passage of the cap screw which served as the exciting force.

Bearing oil film pressure was measured by taps connected to 4-1/2 inch test quality pressure gages. The taps were installed in one bearing of 100 degree arc with C/R of 4×10^{-3} in/in. They were arranged in a cross formation with 5 taps around the bearing arc at the midplane and 5 taps across the bearing length at the center of the arc. In this and all experiments with partial arc bearings, the unidirectional load line passed through the center of the bearing arc. No attempt was made to measure fluctuation in response to dynamic load.

V. BEARING STATIC LOAD PROPERTIES

Measurements of steady state load capacity have been made for 100 degree partial arc bearings of $C/R = 2 \times 10^{-3}$ in/in and $C/R = 4 \times 10^{-3}$ in/in and for the 360 degree, $C/R = 4 \times 10^{-3}$ in/in bearing covering a range of Reynolds Numbers (based on concentric bearing clearance) from laminar flow to 13,300. In addition the static load pressure distribution in a partial arc bearing was measured for a range of values of Reynolds number and eccentricity ratio.

1. Partial-Arc Bearing Static Load Capacity

Unidirectional, steady state load capacity experimental data points are superimposed on the corresponding theoretical curves of dimensionless load parameter plotted against eccentricity ratio, Figs.36 through 40. In all cases the load line bisects the bearing arc. The laminar flow theoretical curve is included in each figure for comparison with the results at various Reynolds numbers. Laminar flow experimental data is plotted along with the $Re = 1665$ data in Fig. 36. The correlation between theory and experiment is excellent, especially at higher values of ϵ . The experimental load capacity becomes somewhat higher than the theoretical curve at values of ϵ below about .5 probably because the applied unit load has become quite small (usually only a few psi) and the effects of even a very small velocity head at the bearing inlet are felt.

There is a small but consistent difference in experimental results for the two values of C/R . The measured load capacity, in terms of dimensionless load, of the 4 mil C/R bearing is slightly higher than that of the 2 mil C/R bearing. This may be a real effect attributable to a difference in Taylor numbers, and thus to a difference in vortex flow characteristics, even though the Reynolds numbers are equal. The difference might also be explained by an error in clearance measurement. A reduction in the value of clearance of about 4 percent or .32 mils for the 4 mil C/R bearing would bring the results into close agreement. Such an error is possible but not very likely considering the accuracy of the gaging equipment used in inspection of the shaft and bearing.

Attitude angle-eccentricity data are given in Figs. 41 and 42. Here again agreement is good, though the effects of Reynolds number are not apparent as they were in the load capacity data due to much smaller variation in attitude angle with Reynolds number and somewhat more experimental data scatter.

2. 360 Degree Bearing Static Load Capacity

Steady state load capacity data and theoretical curves for the 360 degree bearing are given in Figs. 43 through 46. Agreement with the theory is not as good for this bearing. The correlation between experimental and theoretical attitude angle-eccentricity results (Fig. 47) in particular is not as good as it was for the partial arc bearing. The explanation for this is associated with lubricant supply conditions and conditions in the unloaded part of the bearing where film rupture is expected to occur.

The boundary conditions for the 360 degree bearing in the turbulent flow theory as well as in the classical laminar flow analysis are that the load carrying film begins with $p = 0$ at the point where the surfaces begin to converge and ends with $p = \frac{dp}{d\theta} = 0$ at some angle behind the load line. In order to maintain this assumed film extent a specific lubricant supply rate is required. In ordinary bearing applications it makes little difference if the actual lubricant supply rate differs some from the assumed, especially in the direction of oversupply. Some change in active arc length will result but the pressure gradients and pressures are small where the film begins so it is usually considered that any small error in pressure distribution at that point will have little effect. Likewise, film pressures in the loaded arc of the bearing are usually many atmospheres so if the pressure in the film rupture region is not exactly atmospheric as assumed in the theory there is no noticeable effect. Unfortunately, the pressures in the loaded region of the film are unusually low for the bearing and conditions used here because of extremely low kinematic viscosity of the lubricant and comparatively large clearance ratio which are used to achieve high values of Reynolds number. The load capacity and especially the attitude angle of the 360 degree bearing in these experiments were influenced significantly by lubricant supply rate. This dependence on lubricant supply is attributable to changes in

active film arc length and in pressure in the unloaded portion of the film. Depending on the lubricant supply rate which was used, results could be obtained which were characteristic of either starved supply operation or oversupply operation. There was no clearly defined and reasonably broad range of supply rates at which operation conformed to that predicted by theory. From observation of shaft locus measurements it was possible to adjust the lubricant delivery rate for each load and speed to conform approximately to that corresponding to the theoretical boundary conditions. However, prolonged periods of trial and error adjustment would have been required and the results which were obtained would have been of questionable value. Therefore, the lubricant supply was adjusted once for each speed by raising the flow until a stable shaft locus was obtained (irregular, transient small shifts in locus occur under starved supply conditions) at low eccentricity. No further adjustments were made for other loads. Some of the data exhibit the higher load capacity and attitude angles characteristic of over supply, Figs. 43, 44 and 45 and some indicated slight lubricant starvation, Fig. 46.

3. Bearing Film Pressure

Bearing film pressure measurements were desired for additional verification of the steady state load turbulent flow lubrication theory. Because of the difficulties which were experienced with lubricant supply conditions and relatively poor correlation between theoretical and experimental load capacity of the 360 degree bearing, the 100 degree partial arc bearing, $C/R = 4 \times 10^{-3}$ in/in was chosen for these measurements. Pressure taps (.040 inch dia.) were installed in the bearing in the form of a cross with five evenly spaced taps around the arc at the bearing centerline and five evenly spaced taps across the bearing width at the midplane.

Laminar flow data obtained with 5.0 c.s. silicone fluid at 200 rpm is shown in Figs. 48 and 49. Agreement is quite good except for the case of $\epsilon = .8$ where the measurements show lower pressures near the bearing center and somewhat higher pressures at the leading and trailing edge of the pad than the theory predicts. At higher values of ϵ , very small irregularities in arc profile such as might be caused by elastic deformation can significantly alter the exact distribution of pressure.

Theoretical pressure profiles obtained from the eddy viscosity turbulent flow theory (4) are shown in Figs. 50 through 55 along with corresponding experimental measurements for eccentricity ratios of .35, .15 and .18 and a range of Reynolds numbers. There are no experimental data for $\epsilon = .35$, $Re = 13,304$ because of excessive whirl amplitudes. Small whirl orbits prevailed for the $\epsilon = .35$, $Re = 8314$, and 5820 and $\epsilon = .15$, $Re = 13,304$ conditions. The bearing pad was refinished between the laminar and turbulent flow experiments due to a mishap which caused some deformation of the pad.

The correlation between theory and experiment is good, corresponding to the good agreement in measured and calculated steady state load capacity data. There is some evidence of shaft bending from the axial direction profiles for high load conditions, Fig. 55. The direction of the asymmetry in measured pressures is correct for the expected direction of shaft bending (outboard edge of bearing is at left side). In the circumferential direction, the pressures near the arc entrance are generally slightly higher comparatively than those in the downstream region. This may be an effect of a small irregularity in bearing radius of curvature or, it may be a result of a small velocity head at the bearing arc inlet region.

VI. PROCEDURE FOR DETERMINING BEARING DYNAMIC PROPERTIES *

The essential dynamic characteristics of a fluid film bearing can be represented as a group of springs and dash pots arranged as shown in Fig. 56. There are two pairs, each consisting of one spring and one dash pot, to describe the bearing characteristics in each of the two principal orthogonal directions and two additional pairs to describe the cross coupling effects between the two principal directions. Given these eight spring and damping coefficients, the bearing response to a dynamic force acting in any direction or at any frequency can be determined. The forces acting on the shaft are shown together with a typical locus path of the shaft center for a rigid shaft with rotating load in Fig. 57. The motion of the shaft center describes an elliptical path typical of a partial arc bearing or full cylindrical bearing under steady state load since the bearing dynamic properties vary with the direction in which the force is applied for these cases. The forces involved are the rotating unbalance or exciting force, the oil film elastic and damping forces and the rotor inertia force which is directed at the local center of curvature of the locus path. For a given exciting force magnitude and frequency and effective shaft mass, the shaft center locus path will depend on the oil film forces as determined by the bearing spring and damping coefficients. If there are sufficient independent data points, the bearing coefficients can be determined from simultaneous measurements of shaft center locus, and the force applied to the bearing through summation of forces as follows:

$$\begin{aligned} K_{xx}\ddot{x} + K_{xy}\ddot{y} + C_{xx}\dot{x} + C_{xy}\dot{y} &= -F_x + F_o \\ K_{yy}\ddot{y} + K_{yx}\ddot{x} + C_{yy}\dot{y} + C_{yx}\dot{x} &= -F_y \end{aligned}$$

where K and C are the fluid film stiffness and damping coefficients respectively. There are eight coefficients so it is necessary to have eight independent data points. From a given displacement orbit it is possible to extract just 4 independent data points (x and y coordinates at each of two points on the ellipse). Four more can be had if a separate, independent ellipse can be obtained without changing the bearing Reynolds number or the location of the ellipse center within the bearing clearance. This should be possible if the frequency or direction

* See Nomenclature of Appendix 1.

of rotation of the exciting force are changed (a change in rotating load magnitude or in the direction of shaft rotation does not yield an independent locus path). Unless the shape or orientation of the two ellipses are significantly different, very large errors in values of the coefficients will result from small experimental errors. Significant differences in orientation should result from reversing the direction of load rotation with respect to shaft rotation and this is the procedure which was attempted with results which will be described in a later section.

Because of concern over the prospects for obtaining satisfactory results with the direct approach to obtaining the bearing dynamic properties, an alternate approach was prepared which does not require bearing force measurements or counter rotating load data. Instead of eight direct and cross coupling coefficients describing the bearing dynamic properties completely, the alternate approach yields four "effective" coefficients in which direct and cross coupling effects are lumped together and which are strictly valid only for synchronous load and the dynamic system from which they are obtained. As before, the shaft center locus path is described by measurement of the coordinates of two points on the path which are separated by a known angular displacement of the exciting force. In the analysis, described in detail in Appendix 2, the shaft system equations of motion are reduced to simpler equations describing an equivalent system. These equations are of the form:

$$\begin{aligned} M\ddot{x} + K'_x x + C'_x \dot{x} &= \cos \omega t \\ M\ddot{y} + K'_y y + C'_y \dot{y} &= \sin \omega t \end{aligned}$$

where M , K' and C' are equivalent mass, stiffness and damping coefficients respectively. Two independent sets of values x , \dot{x} , \ddot{x} , y , \dot{y} and \ddot{y} are obtained from the shaft locus measurements and the equivalent system, or "effective" coefficients are obtained.

The direct and cross coupling coefficients obtained from the turbulent bearing theory can be reduced to effective coefficients for comparison with the experimental results. The procedure for so doing is outlined in Appendix 2. The

reverse procedure is not possible with one set of effective coefficients since there is no unique solution.

For reasons which will be described, the alternate approach leading to effective coefficients has been used for data reduction. A computer program was written to accomplish the data reduction using the IBM 1620. The program determines the experimental effective coefficients; reduces the theoretical coefficients to effective coefficients; and calculates the experimental and theoretical shaft locus orbits for each operating condition.

VII MEASUREMENT OF BEARING DYNAMIC PROPERTIES

Experimental data have been obtained and reduced to effective coefficients for two partial arc and one cylindrical bearing covering Reynolds numbers, based on mean clearance, from 1665 to 13,304. In addition, some data have been obtained for the partial arc bearing in the laminar flow regime. Theoretical and experimental shaft response orbits are presented for typical cases to illustrate the correlation in this respect. Whirl instability onset conditions have been calculated using theoretical dynamic properties and compared with experimental measurements for some selected conditions.

The effective dynamic coefficients of the bearings were obtained in the experiments because attempts to obtain the complete set of eight direct and cross coupling coefficients from measurements of bearing force and shaft displacement with both synchronous and counter rotating dynamic load resulted in very large scatter and poor agreement. The reasons for this are discussed in a section dealing with counter rotating load.

1. Laminar Flow Results

Theoretical curves and experimental data points of effective spring and damping coefficients were obtained in the laminar flow regime. The results cover a range of Sommerfeld numbers by varying static load at constant speed (2000 rpm) using 5.0 c.s. silicone lubricant ($Re = 216$). This was done to permit comparison of the agreement between theory and experimental in turbulent and laminar flow regimes. Results are given in Figs. 58 and 59 in the form of dimensionless coefficients plotted against Sommerfeld number. The trends as Sommerfeld number varies are very similar for experiment and theory and there is substantial agreement in absolute values for the coefficients. However, the agreement is not as good as that obtained for static load properties, for example. There are a number of reasons why this is to be expected and these will be discussed after presentation of the turbulent flow data.

A second purpose for obtaining data in the laminar flow regime is to compare the agreement between experiment and theory with that obtained by Lund and Sternlicht (6) using their laminar flow theory and the experimental measurements of Hagg and Sankey (7) which are the only other experimental measurements of bearing dynamic response coefficients which have been published. A direct comparison of experimental measurements with those of Hagg and Sankey is not valid since in both cases effective coefficients are obtained and as such they are dependent on the dynamic characteristics of the experimental apparatus on which they were obtained. The curves shown in Fig. 60 were taken from Ref. 6. Scatter in the data points around the smooth curves which are shown was frequently on the order of 2 to 1. Discrepancies between theory and experiment of the same or greater magnitude as were obtained in this work are evident.

2. Partial Arc Bearing Results in Turbulent Flow Regime

Experimentally and theoretically derived effective spring and damping coefficients are shown for the $\beta = 100^\circ$, $C/R = 4 \times 10^{-3}$ in/in bearing in Figs. 61 through 64 and those for the $\beta = 100^\circ$, $C/R = 2 \times 10^{-3}$ in/in bearing are given in Figs. 65 through 68. In each figure one coefficient is plotted in dimensionless form for the range of Sommerfeld numbers covered by the experiment and for the Reynolds numbers used for that bearing. Since these are effective coefficients, they are dependent on the load frequency and certain characteristics of the system including bearing clearance. Therefore, different results are obtained for the two bearings of different C/R even though the Reynolds and Sommerfeld numbers are the same. The dimensionless bearing stiffnesses decrease and the damping coefficients increase with increasing Reynolds number at fixed Sommerfeld number. This is because the mean eccentricity ratio becomes smaller as Reynolds number is increased at constant Sommerfeld number (see static load capacity results). Certain experimental data, specifically the motion of the shaft at the support bearing end, is required to reduce the theoretical dynamic properties to the effective coefficients which are plotted in Figs. 61 through 68. For this reason there are slight irregularities among the theoretical curves which would not be expected of results obtained solely by calculation. For the same reason the theoretical coefficients cover only the range of Sommerfeld numbers for which experimental data were obtained.

The experimental points generally form reasonably continuous curves with sufficiently small experimental scatter to make identification of trends clear. Considering the nature of the data being compared, there is acceptable, even good, correlation between theoretical and experimental results. Except for a few instances the trend of the experimental points is similar to that of the theoretical curve. A particular exception is the stiffness normal to load line for $C/R = 4 \times 10^{-3}$, Fig. 62, where there is a regularly increasing difference in experimental and theoretical trend as Reynolds number is increased until at $Re \approx 13,304$ they are nearly orthogonal. There is an unusually large amount of scatter and some evidence of a similar deviation in trend at high Reynolds numbers for the same coefficients with the $C/R \approx 2 \times 10^{-3}$ in/in bearing, Fig. 66. With few exceptions, the effect of Reynolds number on the theoretical coefficients is large compared to the experimental scatter and a similar effect of Reynolds number can be identified in the experimental results. This situation implies that it is worthwhile to consider turbulence and introduce Reynolds number as a variable in determining bearing dynamic properties for low kinematic viscosity lubricant applications.

In general, agreement between theory and experiment is somewhat better with respect to damping coefficients than it is for stiffness coefficients. This is rather surprising since bearing damping should be very sensitive to attitude angle and there was somewhat better agreement between eccentricity ratios than there was between attitude angles in the static load results.

It can and has been said that the agreement between experimental and theoretical dynamic coefficients is good for this type of data. However, what is important is whether the theoretical dynamic load coefficients can be used to accurately predict the shaft response, critical speeds and stability characteristics. The theoretical and experimental shaft response orbits were calculated for each operating condition as part of the data reduction program. These orbits are superimposed for comparison for a series of Sommerfeld numbers for several different Reynolds numbers in Figs. 69 through 74. These results are typical. It should be recognized that only

the dynamic components of the shaft locus are compared; there are differences in the experimental and theoretical ellipse center locations within the bearing clearance of the same general magnitude as those reported earlier under static load properties. The agreement between theoretical and measured response is very good except for an intermediate range of Sommerfeld number where the theoretical response goes through a maximum while the measured ellipses continuously grow smaller with decreasing Sommerfeld number. Evidently the theoretical coefficients indicate a damped rigid body critical speed at some value of Sommerfeld number in the range of 0.2 to 0.5 with the exact value depending on Reynolds number and C/R. There was no corresponding increase in experimental response dimensions in this range of Sommerfeld numbers. However, from notation of the positions of the unbalance force markers on the response ellipse, a smooth gradual shift in the angle between the exciting force and the displacement (angle ϕ in Fig. 57) of 180 degrees was observed experimentally as the load was varied through the same general range of Sommerfeld numbers as those at which the peak response is predicted by theory. Evidently the bearing does pass through a rigid body critical speed under these conditions but it is so highly damped as to be unnoticeable in the shaft response.

The theoretical spring and damping coefficients were used to compute the predicted load for onset of half frequency whirl at several speeds for the partial arc bearing, $C/R = 4 \times 10^{-3}$ in/in and 0.65 c.s. lubricant using the approach described in Ref. 8. Experimental determinations of whirl onset were made at fixed speed to maintain constant Reynolds number. Initially the load was raised until eccentricity was .8 or higher and there was no whirl. With the electronic filters set to pass frequencies only in a band around half synchronous speed, the load was gradually reduced until a regular orbital movement of the shaft locus point on the oscilloscope screen could be detected. This was taken as the whirl onset condition. The effects of substantial damping of the bearing film were evident in a very slow increase in whirl orbit size as load was decreased further. The results are summarized in Table 1.

TABLE 1

Reynolds Number	Shaft Speed rpm	Load at Onset of Fractional Frequency Whirl - lbs.	
		Experiment	Theory
5820	3500	132	110
8314	5000	198	175
13,304	8000	312	350

Agreement between results derived from the theoretical coefficients and the direct experimental measurements is good, again indicating that the theoretical coefficients are of practical value.

3. Full Cylindrical Bearing in Turbulent Regime

Effective spring and damping coefficients have been determined from the theory and by experiment for the 360 degree plain bearing for Reynolds numbers from 3326 to 13,304. The agreement between theory and experiment is generally poor as is shown by the results for 5820 and 13,304 Reynolds number, Figs. 72 through 75. The experimental damping coefficients are substantially higher than the theoretical values and there is a good deal of experimental scatter. There are several explanations for these poor results:

1. Agreement between theory and experiment for static load is not very good, especially with respect to attitude angles. Bearing damping in particular is quite sensitive to attitude angle so there should be differences in dynamic properties when the static load properties are not in close agreement.
2. In the theory it is assumed that there is no contribution to bearing damping or stiffness from those areas where the film is assumed to be ruptured. In actual fact there will be substantial areas where the film is continuous between the surfaces since rupture should take the form of striations or streamers.

The effect of pressure in the unloaded region and of the accompanying shift in mean shaft locus was investigated for two data points at $Re = 5820$ ($\epsilon = .58$ and $.87$). The pressure at which rupture is assumed to occur was adjusted until the theoretical attitude angle corresponded with the measured value. Pressures in the rupture zone of 4.7 and 6.7 psia were required for the low and high ϵ cases respectively. This resulted in a change in calculated load capacity also which brought the theory into excellent agreement with the experiment at these points. The theoretical dynamic load coefficients changed as expected in the correct direction to bring them into closer agreement with the experimental results. Agreement with respect to stiffness coefficients had been acceptable and was improved slightly. Theoretical damping coefficients had been far below the experimental values and the change was too small to achieve even fair agreement. The results indicate that there is a substantial contribution to damping from the film rupture region of the bearing or from some other, unknown, source.

Agreement between theoretical and experimental response orbits, Fig. 76, reflects the poor correlation between coefficients, but even so it is good enough to indicate that the theoretical dynamic properties can be useful in spite of significant differences in assumed and real lubricant supply and boundary conditions.

4. Experiments with Counter Rotating Load

Initial plans called for experiments with forward and counter-rotating loads at each condition of Reynolds number and load to obtain two independent, and different, shaft response orbits. Eight independent data points and thus the eight direct and cross coupling bearing coefficients could be obtained directly in this way.

When a counter-rotating load at the speed of shaft rotation was applied, two apparently anomalous effects were observed:

1. The shaft center moves around its elliptical orbit in the direction in which the shaft is rotating and not in the direction in which the applied force is rotating. Referring to Fig. 57, the unbalance

force vector rotates in one direction while the journal mass moves around its path in the other direction. Intuition argues strongly that they should go in the same direction. When the shaft is simply hung in the bearing clearance without rotation and the rotating load is applied by running the rotating load motor, the observations support the intuitive expectation of the same direction for load vector and shaft locus rotation.

2. Unless the rotating load and shaft rotation frequencies are exactly equal there is a beat effect causing the response orbit to change cyclically between two extremes in size and shape. If the frequencies are matched exactly, a stable orbit can be obtained, or more properly, any one of a great many stable orbits can be obtained representing all of the variations encountered during the beat effect.

Typical oscilloscope photographs of forward and counter rotating orbits for the same operating conditions are shown in Fig. 77. The two orbits on the photograph for counter rotation were taken with separate exposures and displacement of the orbit center on the screen to show the extremes in size and shape encountered during the slow beat. As expected, the ellipses obtained from forward and counter rotating load are quite different and it seems that reasonably good results should have been obtained if there were no cyclic variation in the response ellipse with counter rotating load.

If it is granted that the directions of rotation of the exciting load vector and shaft locus point will be reversed, an explanation for the beat effect is available. The bearing sees the effects of two rotating loads; the exciting load which is driven externally in one direction and the inertia force of the shaft as its mass center moves about its orbit, in this case in the opposite direction. Since the bearing dynamic properties are anisotropic, the shaft response will depend on the directions with respect to the bearing of these two force vectors when they are exactly out of phase; or exactly in phase; or at any other relative position which may be chosen for reference. If they are in phase when directed along the steady state load line the response

will be different than it will be if they are in phase when directed at right angles to the load line.

The theoretical and experimental shaft response for a number of cases with counter rotational load were calculated. To do this appropriate changes were made in the signs and directions of the cross coupling coefficients to provide for a change in the direction of shaft rotation (because the mean shaft locus changes from one side of the bearing centerline to the other) while maintaining the same rotating load direction. The initial (time = 0) positions of the exciting force and shaft inertia force in the response program was such that for the theoretical response the forces were in phase when their direction was horizontal and exactly out of phase when vertical. The results are shown in the plotted response orbits, Fig. 78, for the same conditions for both forward and counter rotating load derived from the theory and from experimental measurements. There are two experimental orbits representing the extremes of the beat effect. Arrows indicate the direction in which the shaft center moves around the orbits in each case. Remembering that the shaft rotation was reversed while the load rotation direction was the same, it is clear that the theory predicts the same effect seen in the experiments; with counter rotating load the shaft orbits in the forward direction or the direction of shaft rotation. There is still no simple explanation for this in physical terms. Mathematically, an inspection of the response equations shows that the effect is caused by the cross coupling coefficients. This result helps confirm the validity of the theoretical model used to describe the bearing dynamic properties; that is, the concept of direct and cross coupling spring and damping coefficients.

The experimental observations for the counter rotating load cases have been explained but this has not immediately altered the difficulty in obtaining the complete bearing properties directly from experiments. Some way is needed of indicating what the orientation of the shaft inertia and rotating load forces is with respect to the bearing when measurements are taken. Means of accomplishing this could surely be devised. However, there was insufficient time in this program to accomplish this so the alternate approach involving effective coefficients was used.

VIII. DISCUSSION OF DYNAMIC LOAD RESULTS

The intent of the dynamic load investigation was to obtain spring and damping coefficients for several fundamental bearing configurations by experiment and compare these with the same coefficients derived from the turbulent flow lubrication theory. Failing this, the experimental data was to serve as a self sufficient body of empirical information. The agreement which was obtained is considered to be good for this type of data. There are discrepancies between experiment and theory and these may occur because of differences in the theoretical model and the actual physical situation in the areas of turbulent flow lubrication and rotor-bearing dynamics. Other possible reasons for differences include errors in control of experimental conditions and in reading experimental results and simplifications resorted to in order to achieve a mathematical solution of the turbulent flow theoretical model.

The assumptions and simplifications of the turbulent flow lubrication theory and their significance are discussed in some detail in Ref. 4.. Briefly, this is a linearized treatment in which mean fluid velocity is assumed to be a linear function of pressure. This assumption appears to hold up very well for the conditions characteristic of lubrication practice. The flow transition region is treated as a smooth, regular change from laminar to turbulent friction characteristics while the transition observed in pipe flow and Couette flow experiments is sudden and well defined. Also there is no means of considering the effects of vortex flow in either the laminar or fully turbulent flow regimes. Excellent correlation with experiment in static load properties suggests that there are no serious discrepancies in the turbulent flow theory, at least for these conditions. Also, the agreement between theory and experiment in dynamic load properties with turbulent flow is of the same general degree of goodness as is the agreement for laminar conditions.

The response analysis for reduction of experimental measurements to effective coefficients and for reduction of the complete set of theoretical coefficients

to comparable effective coefficients makes a number of assumptions regarding the dynamic characteristics of the apparatus:

1. The shaft is perfectly rigid.
2. There is no restraint to motion of the shaft in the test bearing clearance from the support bearing or the coupling.
3. Stiffness and damping at the test bearing end come from the bearing pad only.
4. The deliberately applied exciting force is the only external source of dynamic load.

There is a rather consistent tendency for the experimental damping coefficients to be higher than the theoretical coefficients and for the experimental response orbits to be smaller than the theoretical orbits. This seems to be indicative of some restraint to angular motion of the shaft at the support bearing end or, more likely, of additional damping from the relieved area outside the test bearing arc and from the seal rings at each end of the bearing. There is some bending of the shaft; at high eccentricity ratios and higher speeds distortion of the response ellipse because of nonlinearity introduced by bending was observable.

The end uses of dynamic bearing properties are in calculation of response orbits as a function of operating conditions and in prediction of bearing hydrodynamic instability characteristics. The theoretical coefficients produce results which are in substantial agreement with the experimental observations when they are applied for these purposes. This firmly supports the conclusion that the turbulent flow lubrication theory of Ref. 4 can be used confidently in design calculations involving static and dynamic loading at least for fundamental bearing configuration of the type used in this work.

APPENDIX 1

Dynamic Analysis of Journal Bearings

1. Nomenclature

C	Radial clearance	inches
$C_{xx}, C_{xy}, C_{yx}, C_{yy}$	Damping coefficients	lb sec/inch
D	Diameter	inches
e	Eccentricity	inches
F	Fluid film force	lbs
\bar{f}	$(= \frac{F}{\mu NLD} (\frac{R}{C})^2)$ Dimensionless force	
h	Film thickness	
$K_{xx}, K_{xy}, K_{yx}, K_{yy}$	Stiffness coefficients	lbs/inch
L	Length	
N	Speed	R.P.S.
P	Pressure	lb/in ²
R	Radius	inches
Re	$(= \frac{VC}{\nu})$ Reynolds Number based on mean clearance	
Re_h	$(= \frac{Vh}{\nu})$ Reynolds Number based on local film thickness	
S	$(= \frac{\mu NLD}{W} (\frac{R}{C})^2)$ Sommerfeld Number	
t	Time	seconds
V	$(= \pi DN)$ Surface velocity	in/sec.
W	Load	lbs
x	Coordinate, in direction of steady state load (also used in Equations A-3, to denote circumferential direction.)	inches
y	Coordinate, normal to direction of steady state load,	inches
z	Coordinate, in axial direction	inches

ϵ	$(= \frac{e}{C})$ eccentricity ratio	
θ	Circumferential coordinate	radians
λ	$(= \frac{\mu DL}{2\pi} (\frac{R}{C})^2)$, Coefficient (see Eq. A-12)	lb.sec.
μ	Absolute viscosity	lb.sec./in ²
ν	Kinematic viscosity	in ² /sec.
ϕ	Attitude angle	radians
ω	Angular velocity	radians/sec.

Superscripts

—	Dimensionless quantity (see Eqs. A-3c,13,14,29, & 30).
.	Time derivative

Subscripts

r	Component in radial direction
t	Component in tangential direction
x	Component in direction of steady state load
y	Component in direction normal to steady state load
o	Steady state value

2. Introduction

The resultant of the fluid film pressures generated by hydrodynamic action in a journal bearing is a non-linear function of the displacement, attitude and velocity of the journal center. This non-linearity precludes exact analysis by superposition of the characteristics of the components of the system (shaft, bearings and pedestals). Instead, an exact analysis would require solution of the coupled equations of motion of all three components. Such an analysis is too complex to undertake. Moreover, individual solutions would be of little value for design purposes because of the very large number of shaft, bearing and pedestal parameters.

Analytical solutions are therefore based on examination of small motions of the journal center about its equilibrium position. By this means, the fluid film force vector is reduced to a set of spring and dashpot type force coefficients; the local values of these coefficients being the gradients of the force-displacement and force-velocity curves, calculated at the equilibrium position of the journal center. These coefficients describe the journal bearing characteristics. For purposes of dynamic analysis of rotating machinery, the shaft characteristics are similarly represented by the stiffness, mass and inertia distributions while the pedestal characteristics are described by their masses and by a second set of spring and dashpot force coefficients, in series with those of the fluid film. The equations of motion of the complete system can then be written in terms of the linearized characteristics of the three components and solved to calculate the dynamic performance of rotating machinery, i.e.

- a) critical speeds
- b) rotor response to dynamic loads
- c) boundaries of the regions of stable operation.

Such analysis is, of course, strictly valid only for infinitesimal motions of the journal center. The degree of agreement between the linearized analysis and practical rotor systems will depend on how closely the fluid film force vs shaft center displacement curve approaches linearity in the region of interest. Thus, the curvature (second derivative) of the force vs displace-

ment curve is a measure of the agreement expected between the analysis and the practical system; provided that the curvature is moderate, agreement with practice should be quite good. In most hydrodynamic journal bearings, this condition is satisfied up to eccentricity ratios as high as 0.7 or even 0.8. Above these values however, the curve becomes extremely steep (theoretically, the force becomes infinite at an eccentricity ratio of 1), so that the linear analysis breaks down completely. High thermal gradients and deformations of the shaft and bearing surfaces further complicate the problem in the high eccentricity ratio range.

The observation noted in the above paragraph is supported by experimental evidence. For example, the experimental studies conducted in the program reported here showed satisfactory agreement between the calculated and the measured elliptical shaft center orbits, up to eccentricity ratios of 0.8. At higher values of eccentricity ratio however, there was a pronounced flattening of the lower part of these orbits due to high non-linearity.

The linearized analysis has been developed by several investigators, and is described in various degrees of detail in, for example, Refs. 4, 6, and 9. An outline of it, based on the work of Lund (Refs. 4 & 10) is provided here for ease of reference. All these previous references provided only the data necessary for design of rotor-bearings systems which operate with laminar flow journal bearings. In the currently completed program, the data (Figs. 1 through 32) is presented for turbulent as well as for laminar flow bearings.

3. Stiffness and Damping Coefficients of a Journal Bearing

With a perfectly balanced rotor the journal center will occupy a fixed position in the journal bearing, that is determined by the: rotation speed, magnitude of the steady state load, bearing size and geometry and the lubricant viscosity. Figure 79, shows a journal in such an equilibrium position, defined by its eccentricity " e_o " and attitude angle " ϕ_o ". The equilibrium positions of the shaft are obtained from numerical solution of the steady state lubrication equation as discussed a little later in this appendix. They were calculated in this study for plain circular and 100° , centrally loaded partial arc journal bearings (with $L/D = 1$ in both cases), for both laminar and turbulent films. This steady state design data is plotted in dimensionless form in Figs. 1,2,17 and 18.

In practice, of course, the shaft will have some residual unbalance. The resulting centrifugal force causes the journal center to orbit around the steady state position, at a speed which is synchronous with the rotation speed. Additional pressures are generated in the fluid film to counterbalance the forces due to the unbalance load and the inertia of the whirling rotor. These additional pressures vary with time and are functions of both the whirl amplitude and whirl velocity. For small motions of the journal center, the resultant of these dynamic pressures can be considered to be proportional to the whirl amplitude and velocity. The coefficients of proportionality are the spring and damping coefficients of the bearing. There is a set of such coefficients for each bearing geometry and each location (e_o, ϕ_o) of the journal center.

A stationary (x,y), coordinate axis system is shown in Figure 79 with its origin at the equilibrium position of the shaft center. Decomposing: the dynamical fluid film force (resultant of the dynamic component, of the fluid film pressures), the whirl displacement and the whirl velocity along the x and y coordinates, we have:

$$\begin{aligned} F_x - F_o &= -K_{xx} \ddot{x} - C_{xx} \dot{x} - K_{xy} \ddot{y} - C_{xy} \dot{y} \\ F_y &= -K_{yx} \ddot{x} - C_{yx} \dot{x} - K_{yy} \ddot{y} - C_{yy} \dot{y} \end{aligned} \quad (A-1)$$

where:

F_0 is the steady state fluid film force ($=-W$)

F_x, F_y are the fluid film components

x, y are the components of journal center displacement

\dot{x}, \dot{y} are the components of journal center velocity

$K_{xx}, K_{xy}, K_{yx}, K_{yy}$ are the stiffness coefficients, where the first subscript defines the direction of force and the second subscript describes the direction of the displacement.

$C_{xx}, C_{xy}, C_{yx}, C_{yy}$ are the damping coefficients, where the first subscript defines the direction of force and the second subscript defines the direction of velocity.

Although, in principle, this is analogous to a mechanical system of springs and dashpots, there is a significant difference that is caused by the cross coupling effect. The cross coupling effect arises from the fact that the resultant of the fluid pressures that are caused by a displacement (or velocity) of the journal center, is not co-linear with the displacement (or velocity). Thus, if the journal center is displaced (or if a velocity is imparted to it), the resulting change in the fluid film force will have components both along and normal to the direction of the displacement (or velocity). In addition, due to the non-linear nature of force vs displacement and the force vs velocity curves, the spring and damping coefficients are not constants, but vary with the steady state position (e_0, θ_0) of the journal center.

The stiffness and damping coefficients are obtained from the slopes of the force vs displacement and the force vs velocity curves, i.e., in the (x,y) coordinate system defined above:

$$\begin{aligned} K_{xx} &= \frac{\partial F_x}{\partial x} & ; & & C_{xx} &= \frac{\partial F_x}{\partial \dot{x}} \\ K_{xy} &= \frac{\partial F_x}{\partial y} & ; & & C_{xy} &= \frac{\partial F_x}{\partial \dot{y}} \\ K_{yx} &= \frac{\partial F_y}{\partial x} & ; & & C_{yx} &= \frac{\partial F_y}{\partial \dot{x}} \\ K_{yy} &= \frac{\partial F_y}{\partial y} & ; & & C_{yy} &= \frac{\partial F_y}{\partial \dot{y}} \end{aligned} \quad (A-2)$$

These coefficients are calculated for each particular bearing geometry, from the computer solutions of the lubrication equation, as described later in this appendix. In the current study, they were obtained for the plain circular and 100° , centrally loaded, partial arc bearings for both laminar and turbulent flow in the fluid film. The data is given, in dimensionless form, in Figs. 3 through 16 and 19 through 32.

Using linear vibration theory and introducing the calculated values of the fluid film stiffness and damping coefficients, the whirl orbits of a rotor in response to dynamic loads can be calculated. The calculations are performed using any standard methods for computing the vibrations of a beam supported in journal bearings which are defined by the set of stiffness and damping coefficients. The rotor itself is treated as a set of masses and inertias, as in the Holzer or Myklestad-Prohl analyses. Computer programs have been developed for treating rotors of arbitrary shape.

The whirl orbits are computed for each operating speed. (This was done, for example, in the current study for comparison with the measured whirl orbits, see Figs. 69 through 71). The system critical speeds are determined by computing the whirl orbits over a range of speeds and by determining the speed at which the amplitude of the orbits peaks.

4. Numerical Solution of the Incompressible Lubrication Equation

The incompressible lubrication equation for turbulent flow in the fluid film, was derived under another program in Ref. 4.. The derivation was also given in an appendix of Ref. 5. This equation is (see coordinate system defined in Fig.80).

$$\frac{\partial}{\partial x} \left[\frac{h^3 G(x)}{\mu} \frac{\partial P}{\partial x} \right] + \frac{\partial}{\partial z} \left[\frac{h^3 G(z)}{\mu} \frac{\partial P}{\partial z} \right] = \frac{V}{2} \frac{\partial h}{\partial x} \frac{\partial h}{\partial t} \quad (A-3a)$$

Where $G(x)$ and $G(z)$ are functions of the local Reynolds Number ($Re_h = \frac{Vh}{\nu}$). At small values of local Reynolds Number, both $G(x)$ and $G(z)$ approach the value $\frac{1}{12}$ so that Equation (A-3) reduces, under laminar flow conditions in the film, to the conventional Reynolds Equation.

Substituting the relations:

$$V = R\omega$$

$$\text{and } h = C \left[1 + \epsilon \cos(\theta - \phi) \right]$$

into the right hand side of Eq. (A-3), we obtain:

$$\frac{\partial}{\partial x} \left[\frac{h^3 G(x)}{\mu} \frac{\partial P}{\partial x} \right] + \frac{\partial}{\partial z} \left[\frac{h^3 G(z)}{\mu} \frac{\partial P}{\partial z} \right] = c\omega \left(1 - 2 \frac{\dot{\phi}}{\omega} \right) \left[\frac{\left(\frac{\epsilon}{\omega} \right)}{\left(1 - 2 \frac{\dot{\phi}}{\omega} \right)} \cos(\theta - \phi) - \frac{\epsilon}{2} \sin(\theta - \phi) \right] \quad (A-3b)$$

Equation (A-3a) is made non-dimensional by the following substitutions:

$$\begin{aligned} h &= \bar{h}C \\ x &= \bar{x}D \\ z &= \bar{z}L \\ P &= \bar{P} \cdot \mu N \left(\frac{R}{C} \right)^2 = \bar{P} \cdot \frac{\mu \omega D^2}{8\pi C^2} \end{aligned} \quad (A-3c)$$

The turbulent lubrication in non-dimensional form is then:

$$\frac{\partial}{\partial \bar{x}} \left[\bar{h}^3 G(x) \frac{\partial \bar{P}}{\partial \bar{x}} \right] + \left(\frac{D}{L} \right)^2 \frac{\partial}{\partial \bar{z}} \left[\bar{h}^3 G(z) \frac{\partial \bar{P}}{\partial \bar{z}} \right] = 8\pi \left(1 - 2 \frac{\dot{\phi}}{\omega} \right) \left[\frac{\left(\frac{\epsilon}{\omega} \right)}{\left(1 - 2 \frac{\dot{\phi}}{\omega} \right)} \cos(\theta - \phi) - \frac{\epsilon}{2} \sin(\theta - \phi) \right] \quad (A-3d)$$

The finite difference form of this equation is programmed for numerical integration on the I.B.M. 7094 computer. The input quantities for individual calculations are:

$$\theta_{in}, \bar{P}_{in}, \theta_{out}, \bar{P}_{out}, \left(\frac{L}{D}\right), \epsilon, \phi, Re, \left(\frac{\dot{\epsilon}}{\omega}\right), \left(\frac{\dot{\phi}}{\omega}\right)$$

where $\theta_{in} (=2\bar{x}_{in})$ and $\theta_{out} (=2\bar{x}_{out})$ are, respectively, the coordinates of the inlet and outlet edges of each bearing pad. Thus, the calculations can be conducted either for a 360° bearing or for any other bearing arc length.

\bar{P}_{in} and \bar{P}_{out} , are, respectively, the dimensionless values of lubricant pressure at inlet and outlet of the bearing. This permits the calculations to be made for pressurized, as well as unpressurized bearings.

Two points should be noted with regard to the bearings calculations:

1. As noted above, $G(x)$ and $G(z)$ are functions of the local Reynolds Number, $\frac{Vh}{v}$. These have been derived for values of $\frac{Vh}{v}$ up to 10^5 and are introduced into the computer programs as "look up" tables (Ref. 4). In the computer program, the values of $\frac{Vh}{v}$ at each mesh point are calculated and the corresponding values of $G(x)$ and $G(z)$ are used. The local Reynolds Number is:

$$Re_h = \frac{Vh}{v} = \frac{VC}{v} \cdot [1 + \epsilon \cos(\theta - \phi)] = Re \cdot [1 + \epsilon \cos(\theta - \phi)] \quad (A-4)$$

The local Reynolds Number is thus computed automatically in the program at each mesh point, since Re , ϵ and ϕ are all input quantities.

2. The attitude angle ϕ is generally not known in advance. An iteration procedure is therefore used, wherein an assumed value of ϕ is used as input and compared with the calculated value of attitude angle obtained from the program. This procedure is repeated until the assumed and calculated values of ϕ are equal within predetermined allowable error, (generally about 0.02 degrees).

The output from the program is:

1. The pressure map, $\bar{P}(\bar{x}, \bar{z})$
2. The radial and tangential components of force:

$$\bar{f}_r = - \int_{-\frac{1}{2}}^{+\frac{1}{2}} \int_{\bar{x}_{in}}^{\bar{x}_{out}} \bar{P} \cos(\theta - \phi) d\bar{x} d\bar{z}$$

(A-5a)

$$\bar{f}_t = \int_{-\frac{1}{2}}^{+\frac{1}{2}} \int_{\bar{x}_{in}}^{\bar{x}_{out}} \bar{P} \sin(\theta - \phi) d\bar{x} d\bar{z}$$

3. The total fluid film force and the calculated attitude angle:

$$\bar{f} = (\bar{f}_r^2 + \bar{f}_t^2)^{1/2}$$

(A-5b)

$$\phi = \tan^{-1} \frac{\bar{f}_t}{\bar{f}_r}$$

For dynamical analysis of journal bearings, the program is also used to calculate the eight stiffness and damping coefficients about the steady state position (ϵ_0, ϕ_0) , in the radial and tangential directions. These are:

$$\left. \frac{\partial \bar{f}_r}{\partial \epsilon} \right|_{(\epsilon_0, \phi_0)} = \frac{\left. \bar{f}_r \right|_{\epsilon = \epsilon_0 + \Delta \epsilon} - \left. \bar{f}_r \right|_{\epsilon = \epsilon_0 - \Delta \epsilon}}{2 \Delta \epsilon} \quad \left. \begin{array}{l} \phi = \phi_0 \\ \frac{\dot{\epsilon}}{\omega} = \frac{\dot{\phi}}{\omega} = 0 \end{array} \right|$$

$$\left. \frac{\partial \bar{f}_r}{\partial \phi} \right|_{(\epsilon_0, \phi_0)} = \frac{\left. \bar{f}_r \right|_{\phi = \phi_0 + \Delta \phi} - \left. \bar{f}_r \right|_{\phi = \phi_0 - \Delta \phi}}{2 \Delta \phi} \quad \left. \begin{array}{l} \epsilon = \epsilon_0 \\ \frac{\dot{\epsilon}}{\omega} = \frac{\dot{\phi}}{\omega} = 0 \end{array} \right|$$

$$\frac{\partial \bar{f}_r}{\partial \left(\frac{\dot{\epsilon}}{\omega}\right)} = \frac{\bar{f}_r \Big|_{\Delta \left(\frac{\dot{\epsilon}}{\omega}\right)} - \bar{f}_r \Big|_{-\Delta \left(\frac{\dot{\epsilon}}{\omega}\right)}}{2 \Delta \left(\frac{\dot{\epsilon}}{\omega}\right)} \quad \left| \begin{array}{l} \epsilon = \epsilon_0 \\ \phi = \phi_0 \\ \frac{\dot{\phi}}{\omega} = 0 \end{array} \right.$$

$$\frac{\partial \bar{f}_r}{\partial \left(\frac{\dot{\phi}}{\omega}\right)} = \frac{\bar{f}_r \Big|_{\Delta \left(\frac{\dot{\phi}}{\omega}\right)} - \bar{f}_r \Big|_{-\Delta \left(\frac{\dot{\phi}}{\omega}\right)}}{2 \Delta \left(\frac{\dot{\phi}}{\omega}\right)} \quad \left| \begin{array}{l} \epsilon = \epsilon_0 \\ \phi = \phi_0 \\ \left(\frac{\dot{\epsilon}}{\omega}\right) = 0 \end{array} \right. \quad (A-6a)$$

(where: $\Delta\epsilon$, $\Delta\phi$, $\Delta\left(\frac{\dot{\epsilon}}{\omega}\right)$ and $\Delta\left(\frac{\dot{\phi}}{\omega}\right)$ are small quantities, generally 10^{-3})

The four derivatives of \bar{f}_t are similarly obtained.

The radial and tangential coordinate axes are not generally the most useful axes for rotor-bearing dynamics analysis. For example, in the case of a multi bearing system, where the bearings are not identical or where the bearings do not carry equal loads, the radial and tangential directions will vary from bearing to bearing. Thus, for the purpose of presenting generalized bearing data, an (x,y) coordinate system, as shown in Figure 79 is preferred, where the "x" axis is parallel to the steady state load direction. In this case we have

$$\bar{f}_x = \bar{f}$$

and

$$\bar{f}_y = 0 \quad (A-6b)$$

The eight corresponding stiffness and damping coefficients are obtained as described in the next section of this appendix.

5. Calculation of the Stiffness and Damping Coefficients

The stiffness and damping coefficients along the reference (x,y) axes of Figure 79, should now be obtained from the derivatives along the radial and tangential directions, that were defined above.

The fluid film force has components F_x and F_y . Under steady state conditions, when the journal center is at $(e_o = ce_o, \phi_o)$ we have $F_x = -W$ and $F_y = 0$, where W is the steady state load on the bearing. Converting from the radial and tangential coordinate system, to the (x,y) coordinate system, we have:

$$\begin{Bmatrix} F_x \\ F_y \end{Bmatrix} = \begin{Bmatrix} -W \\ 0 \end{Bmatrix} = - \begin{Bmatrix} \cos \phi & \sin \phi \\ \sin \phi & -\cos \phi \end{Bmatrix} \cdot \begin{Bmatrix} F_r \\ F_t \end{Bmatrix} \quad (A-7)$$

For an infinitesimally small motion around the state state position the dynamic forces become from Eq. (A-7).

$$\begin{Bmatrix} dF_x \\ dF_y \end{Bmatrix} = - \begin{Bmatrix} \cos \phi & \sin \phi \\ \sin \phi & \cos \phi \end{Bmatrix} \cdot \begin{Bmatrix} dF_r + F_t d\phi \\ dF_t - F_r d\phi \end{Bmatrix} \quad (A-8)$$

The infinitesimal dynamic motion of the journal center is described by the coordinates (x,y):

$$x = d(e \cos \phi) \quad y = d(e \sin \phi)$$

or

$$\begin{Bmatrix} de \\ ed\phi \end{Bmatrix} = \begin{Bmatrix} \cos \phi & \sin \phi \\ -\sin \phi & \cos \phi \end{Bmatrix} \cdot \begin{Bmatrix} x \\ y \end{Bmatrix} \quad (A-9)$$

The velocities transform similarly:

$$\begin{Bmatrix} \dot{de} \\ ed\dot{\phi} \end{Bmatrix} = \begin{Bmatrix} \cos \phi & \sin \phi \\ -\sin \phi & \cos \phi \end{Bmatrix} \cdot \begin{Bmatrix} \dot{x} \\ \dot{y} \end{Bmatrix} \quad (A-10)$$

The dynamic force components dF_r and dF_t may be expressed in terms of the dynamic amplitudes. From Equations (A-3b, c & d) can be shown that the fluid film force F can be written:

$$\begin{aligned} F_r &= \lambda \omega (1 - 2 \frac{\dot{\phi}}{\omega}) \cdot \bar{f}_r(\epsilon, \phi, \frac{\dot{\epsilon}}{\omega}) / (1 - 2 \frac{\dot{\phi}}{\omega}) \\ \text{and} \\ F_t &= \lambda \omega (1 - 2 \frac{\dot{\phi}}{\omega}) \cdot \bar{f}_t(\epsilon, \phi, \frac{\dot{\epsilon}}{\omega}) / (1 - 2 \frac{\dot{\phi}}{\omega}) \end{aligned} \quad (A-11)$$

where:

$$\lambda = \frac{\mu R L}{\pi} \left(\frac{R}{C} \right)^2 \quad (A-12)$$

$$\bar{f}_r = \frac{F_r}{\mu N D L} \left(\frac{C}{R} \right)^2 \quad (A-13)$$

$$\bar{f}_t = \frac{F_t}{\mu N D L} \left(\frac{C}{R} \right)^2 \quad (A-14)$$

Therefore:

$$dF_r = \lambda \omega \left[\left(1 - 2 \frac{\dot{\phi}}{\omega} \right) \frac{\partial \bar{f}_r}{\partial \epsilon} d\epsilon + \frac{\partial \bar{f}_r}{\partial \phi} \epsilon d\phi + \frac{\partial \bar{f}_r}{\partial (\frac{\dot{\epsilon}}{\omega} / (1 - 2 \frac{\dot{\phi}}{\omega}))} d \left(\frac{\frac{\dot{\epsilon}}{\omega}}{1 - 2 \frac{\dot{\phi}}{\omega}} \right) - \frac{2 \bar{f}_r}{\omega \epsilon} \epsilon d\phi \right] \quad (A-15)$$

and similarly for dF_t

Now, at the steady state position, (ϵ_o, ϕ_o) :

$$d \left(\frac{\frac{\dot{\epsilon}}{\omega}}{1 - 2 \frac{\dot{\phi}}{\omega}} \right) = \frac{1}{1 - 2 \frac{\dot{\phi}}{\omega}} d \left(\frac{\dot{\epsilon}}{\omega} \right) + \frac{2 \frac{\dot{\epsilon}}{\omega}}{(1 - 2 \frac{\dot{\phi}}{\omega})^2} d \left(\frac{\dot{\phi}}{\omega} \right) = d \left(\frac{\dot{\epsilon}}{\omega} \right)$$

because at the equilibrium position $\dot{\epsilon}_o = \dot{\phi}_o = 0$. Hence Eq. (A-15) reduces to:

$$dF_r = \frac{1}{C} \lambda \omega \left[\frac{\partial \bar{f}_r}{\partial \epsilon} d\epsilon + \frac{\partial \bar{f}_r}{\partial \phi} \epsilon d\phi + \frac{1}{\omega} \frac{\partial \bar{f}_r}{\partial (\frac{\dot{\epsilon}}{\omega})} d\epsilon - \frac{1}{\omega} \frac{2 \bar{f}_r}{\epsilon} \epsilon d\phi \right] \quad (A-16)$$

and similarly for dF_t .

By substitution of Eq. (A-16) into Eq. (A-8).

$$\begin{bmatrix} dF_x \\ dF_y \end{bmatrix} = - \frac{1}{C} \lambda \omega \begin{bmatrix} \cos \phi & \sin \phi \\ \sin \phi & -\cos \phi \end{bmatrix} \cdot \left\{ \begin{bmatrix} \frac{\partial \bar{f}_r}{\partial \epsilon} & \frac{\partial \bar{f}_r}{\partial \phi} + \frac{\bar{f}_t}{\epsilon} \\ \frac{\partial \bar{f}_t}{\partial \epsilon} & \left(\frac{\partial \bar{f}_t}{\partial \phi} - \frac{\bar{f}_r}{\epsilon} \right) \end{bmatrix} \begin{bmatrix} d\epsilon \\ \epsilon d\phi \end{bmatrix} + \frac{1}{\omega} \begin{bmatrix} \frac{\partial \bar{f}_r}{\partial (\frac{\dot{\epsilon}}{\omega})} - \frac{2 \bar{f}_r}{\epsilon} \\ \frac{\partial \bar{f}_t}{\partial (\frac{\dot{\epsilon}}{\omega})} - \frac{2 \bar{f}_t}{\epsilon} \end{bmatrix} \begin{bmatrix} d\epsilon \\ \epsilon d\phi \end{bmatrix} \right\} \quad (A-17)$$

The stiffness and damping coefficients are defined by:

$$\begin{aligned} dF_x &= -K_{xx}\dot{x} - C_{xx}\ddot{x} - K_{xy}\dot{y} - C_{xy}\ddot{y} \\ dF_y &= -K_{yx}\dot{x} - C_{yx}\ddot{x} - K_{yy}\dot{y} - C_{yy}\ddot{y} \end{aligned} \quad (A-18)$$

To determine the 8 coefficients, substitute Eq. (A-9) and (A-10) into Eq. (A-17) and collect the terms in accordance with Eq. (A-18) to get:

$$K_{xx} = \frac{1}{C} \lambda \omega \left[\frac{\partial \bar{f}_r}{\partial \epsilon} \cos^2 \phi - \frac{\partial \bar{f}_t}{\epsilon \partial \phi} \sin^2 \phi - \left(\frac{\partial \bar{f}_r}{\epsilon \partial \phi} - \frac{\partial \bar{f}_t}{\partial \epsilon} \cos \phi \sin \phi - \frac{\bar{f}_y}{\epsilon} \sin \phi \right) \right] \quad (A-19)$$

$$\omega C_{xx} = \frac{1}{C} \lambda \omega \left[\frac{\partial \bar{f}_r}{\partial (\frac{\dot{\epsilon}}{\omega})} \cos^2 \phi + \frac{\partial \bar{f}_t}{\partial (\frac{\dot{\epsilon}}{\omega})} \cos \phi \sin \phi - \frac{\partial \bar{f}_x}{\epsilon} \sin \phi \right] \quad (A-20)$$

$$K_{xy} = \frac{1}{C} \lambda \omega \left[\frac{\partial \bar{f}_r}{\epsilon \partial \phi} \cos^2 \phi + \frac{\partial \bar{f}_t}{\partial \epsilon} \sin^2 \phi + \left(\frac{\partial \bar{f}_t}{\epsilon \partial \phi} + \frac{\partial \bar{f}_r}{\partial \epsilon} \right) \cos \phi \sin \phi + \frac{\bar{f}_y}{\epsilon} \cos \phi \right] \quad (A-21)$$

$$\omega C_{xy} = \frac{1}{C} \lambda \omega \left[\frac{\partial \bar{f}_t}{\partial (\frac{\dot{\epsilon}}{\omega})} \sin^2 \phi + \frac{\partial \bar{f}_r}{\partial (\frac{\dot{\epsilon}}{\omega})} \cos \phi \sin \phi + \frac{2\bar{f}_x}{\epsilon} \cos \phi \right] \quad (A-22)$$

$$K_{yx} = \frac{1}{C} \lambda \omega \left[-\frac{\partial \bar{f}_t}{\partial \epsilon} \cos^2 \phi - \frac{\partial \bar{f}_r}{\epsilon \partial \phi} \sin^2 \phi + \left(\frac{\partial \bar{f}_t}{\epsilon \partial \phi} + \frac{\partial \bar{f}_r}{\partial \epsilon} \right) \cos \phi \sin \phi + \frac{\bar{f}_x}{\epsilon} \sin \phi \right] \quad (A-23)$$

$$\omega C_{yx} = \frac{1}{C} \lambda \omega \left[-\frac{\partial \bar{f}_t}{\partial (\frac{\dot{\epsilon}}{\omega})} \cos^2 \phi + \frac{\partial \bar{f}_r}{\partial (\frac{\dot{\epsilon}}{\omega})} \cos \phi \sin \phi - \frac{2\bar{f}_y}{\epsilon} \sin \phi \right] \quad (A-24)$$

$$K_{yy} = \frac{1}{C} \lambda \omega \left[-\frac{\partial \bar{f}_t}{\epsilon \partial \phi} \cos^2 \phi + \frac{\partial \bar{f}_r}{\partial \epsilon} \sin^2 \phi + \left(\frac{\partial \bar{f}_r}{\epsilon \partial \phi} - \frac{\partial \bar{f}_t}{\partial \epsilon} \right) \cos \phi \sin \phi - \frac{\bar{f}_x}{\epsilon} \cos \phi \right] \quad (A-25)$$

$$\omega C_{yy} = \frac{1}{C} \lambda \omega \left[\frac{\partial \bar{f}_r}{\partial (\frac{\dot{\epsilon}}{\omega})} \sin^2 \phi - \frac{\partial \bar{f}_t}{\partial (\frac{\dot{\epsilon}}{\omega})} \cos \phi \sin \phi + \frac{2\bar{f}_y}{\epsilon} \cos \phi \right] \quad (A-26)$$

where, in the coordinate system selected,

$$\bar{f}_x = \frac{-W}{\mu_{NLD}} \left(\frac{R}{C} \right)^2 \quad (A-27)$$

$$\bar{f}_y = 0 \quad (A-28)$$

and all forces and derivatives are calculated for the given steady state position, defined by (ϵ_0, ϕ_0) .

The stiffness and damping coefficients are made non-dimensional as follows:

$$\bar{K}_{xx} = \frac{C}{W} \cdot K_{xx} \quad (A-29)$$

$$\bar{C}_{xx} = \frac{C\omega}{W} \cdot C_{xx} \quad (A-30)$$

and similarly for the other coefficients.

These are plotted against the Sommerfeld Number,

$$S = \frac{\mu NLD}{W} \left(\frac{R}{C}\right)^2 \quad (A-31)$$

in Figs. 3-16 and 19-32, for the two bearing types that were studied in this program.

APPENDIX 2

ANALYTICAL DEVELOPMENT OF EQUIVALENT STIFFNESS AND DAMPING FORCES

by

H. Cheng

Analytical Development of Equivalent Stiffness and Damping Factors.

The bearing forces, inertia forces and the external exciting force acting on the experimental rotor are shown in Fig. 81. The meaning of the symbols shown in Fig. 81 are listed as follows:

O'	-	center of the guide bearing
C	-	center of mass of the rotor
A	-	center of the test bearing
B	-	point of application of the exciting force
l_c	-	distance $O'C$ in.
l_a	-	distance $O'A$ in.
l_b	-	distance $O'B$ in.
M	-	mass of rotor lb.sec ² /in.
x'_O, x'_A, x'_C	-	x coordinates of O', A, C respectively, in.
y'_O, y'_A, y'_C	-	y coordinates of O', A, C respectively, in.
F_y, F_x	-	bearing forces at A
M_b	-	mass of the exciting mass (cap screw)
R	-	distance of m_b from B
ω	-	exciting frequency
Ω	-	angular speed of the shaft
T_x	-	x component of the inertia torque
T_y	-	y component of the inertia torque
k_x	-	radius of gyration about an axis passing through c and parallel to $O'x$
k_y	-	radius of gyration about an axis passing through c and parallel to $O'y$
k_z	-	radius of gyration about $O'Z$
\dot{x}	-	$\frac{dx}{dt}$

Taking moment of all forces about O' , we have

$$(B1) \quad M \ddot{y}_c - F_y \ell_a + T_x = \ell_b m_b R \omega^2 \sin \omega t$$

$$(B2) \quad M \ddot{x}_c - F_x \ell_a - T_y = \ell_b m_b R \omega^2 \cos \omega t$$

where the bearing forces, F_x and F_y , and the inertia torques, T_x and T_y are represented by the following expressions,

$$(B3) \quad F_x = -(K_{xx} \dot{x}_a + C_{xx} \ddot{x}_a + K_{xy} \dot{y}_a + C_{xy} \ddot{y}_a)$$

$$(B4) \quad F_y = -(K_{yx} \dot{x}_a + C_{yx} \ddot{x}_a + K_{yy} \dot{y}_a + C_{yy} \ddot{y}_a)$$

$$(B5) \quad T_x = M k_x^2 \left(\frac{\ddot{x}_a - \ddot{x}'_o}{\ell_a} \right) + M (k_y^2 - k_z^2) \Omega \left(\frac{\dot{x}_a - \dot{x}'_o}{\ell_a} \right)$$

$$(B6) \quad T_y = -M k_y^2 \left(\frac{\ddot{x}_a - \ddot{x}'_o}{\ell_a} \right) - M (k_z^2 - k_x^2) \Omega \left(\frac{\dot{y}_a - \dot{y}'_o}{\ell_a} \right)$$

Assuming the shaft is a rigid body, the following geometrical relations prevails,

$$(B7) \quad x_c = x'_o + \left(\frac{\ell_c}{\ell_a} \right) (x_a - x'_o)$$

$$(B8) \quad y_c = y'_o + \left(\frac{\ell_c}{\ell_a} \right) (y_a - y'_o)$$

Substituting (B3) through (B8) into (B1) and (B2) and dividing then by ℓ_a , we have,

$$(B9) \quad M_e \ddot{x}_a + \rho \ddot{x}'_o + (\bar{K}_{xx} \bar{x}_a + \bar{C}_{xx} \dot{x}_a + \bar{K}_{xy} \bar{y}_a + \bar{C}_{xy} \dot{y}_a) + \beta (\ddot{y}_a - \ddot{y}'_o) = \cos \omega t$$

$$(B10) \quad M_e \ddot{y}_a + \rho \ddot{y}'_o + (\bar{K}_{yx} \bar{x}_a + \bar{C}_{yx} \dot{x}_a + \bar{K}_{yy} \bar{y}_a + \bar{C}_{yy} \dot{y}_a) - \beta (\ddot{x}_a - \ddot{x}'_o) = \sin \omega t$$

where

$$M_e = \frac{M_c}{m_b R L_b} \left[L_c^2 + \left(\frac{k_x}{\ell_a} \right)^2 \right]$$

$$k_x = k_y$$

$$\rho = \frac{M_c}{m_b R L_b} \left[L_c (1 - L_c) - \left(\frac{k_x}{\ell_a} \right)^2 \right]$$

(B11)

$$\beta = \frac{M_c}{m_b R \omega L_b} \frac{(\ell_z^2 - k_y^2)}{\ell_a^2} \Omega$$

$$\bar{K}_{xx} = \frac{K_{xx} C}{m_b R \omega^2 L_b}$$

$$\bar{C}_{xx} = \frac{C_{xx} C}{m_b R \omega L_b} \quad \text{etc.}$$

$$\bar{x}_a = x_a / C \quad \text{etc.}$$

$$\bar{y}_a = y_a / C \quad \text{etc.}$$

C = radial clearance of the bearing
and \dot{x} now stands for $\frac{dx}{d(\omega t)}$.

For small oscillations of the rotor, the following substitutions can be made,

$$\begin{aligned} \bar{x}_a &= A e^{i\omega t} \\ \bar{y}_a &= B e^{i\omega t} \\ \bar{x}'_0 &= E e^{i\omega t} \\ \bar{y}'_0 &= F e^{i\omega t} \end{aligned} \quad \text{(B12)}$$

where A, B, E and F are complex amplitudes of oscillation at A and O'.
Substituting (B12) into (B9) and (B10), we have

$$(\bar{K}_{xx} - M_e + i \bar{C}_{xx}) A + [\bar{K}_{xy} + i (\bar{C}_{xy} + \beta)] B = 1 + \rho E + i \beta F \quad \text{(B13)}$$

$$[\bar{K}_{yx} + i (\bar{C}_{yx} - \beta)] A + (\bar{K}_{yy} - M_e + i \bar{C}_{yy}) B = \rho F - i (1 + \beta E) \quad \text{(B14)}$$

If the motion at O' is given, then E and F become known and Equations (B13) and (B14) can be solved for A and B to give

$$(B15) \quad A = \frac{us - vq}{ps - rq}$$

$$(B16) \quad B = \frac{pv - ur}{ps - rq}$$

where

$$(B17) \quad \begin{aligned} p &= \bar{K}_{xx} - M_e + i \bar{C}_{xx} \\ q &= \bar{K}_{xy} + i (\bar{C}_{xy} + \beta) \\ r &= \bar{K}_{yx} + i (\bar{C}_{yx} - \beta) \\ s &= \bar{K}_{yy} - M_e + i \bar{C}_{yy} \\ u &= 1 + \rho E + i\beta F \\ v &= \rho F - i(1 + \beta E) \end{aligned}$$

The dynamic system represented by Eq. (B13) and (B14) can now be reduced to a much simpler equivalent system containing only effective direct stiffness K_x' , K_y' and effective direct damping factors C_x' , C_y' without the cross coupling stiffness and damping factors.

The equations governing the motion of the equivalent system are

$$(B18) \quad M_e \ddot{x}_a + K_x' x_a + C_x' \dot{x}_a = \cos \omega t$$

$$(B19) \quad M_e \ddot{y}_a + K_y' y_a + C_y' \dot{y}_a = \sin \omega t$$

Comparing (B18) and (B19) with (B15)(B16) we obtain the expression for the effective stiffness and damping factors as follows:

$$(B20) \quad K_x' = M_e + \mathcal{R} \left\{ \frac{ps - rq}{us - vq} \right\}$$

$$(B21) \quad K_y' = M_e + \mathcal{R} \left\{ \frac{-i(ps - rq)}{vp - ur} \right\}$$

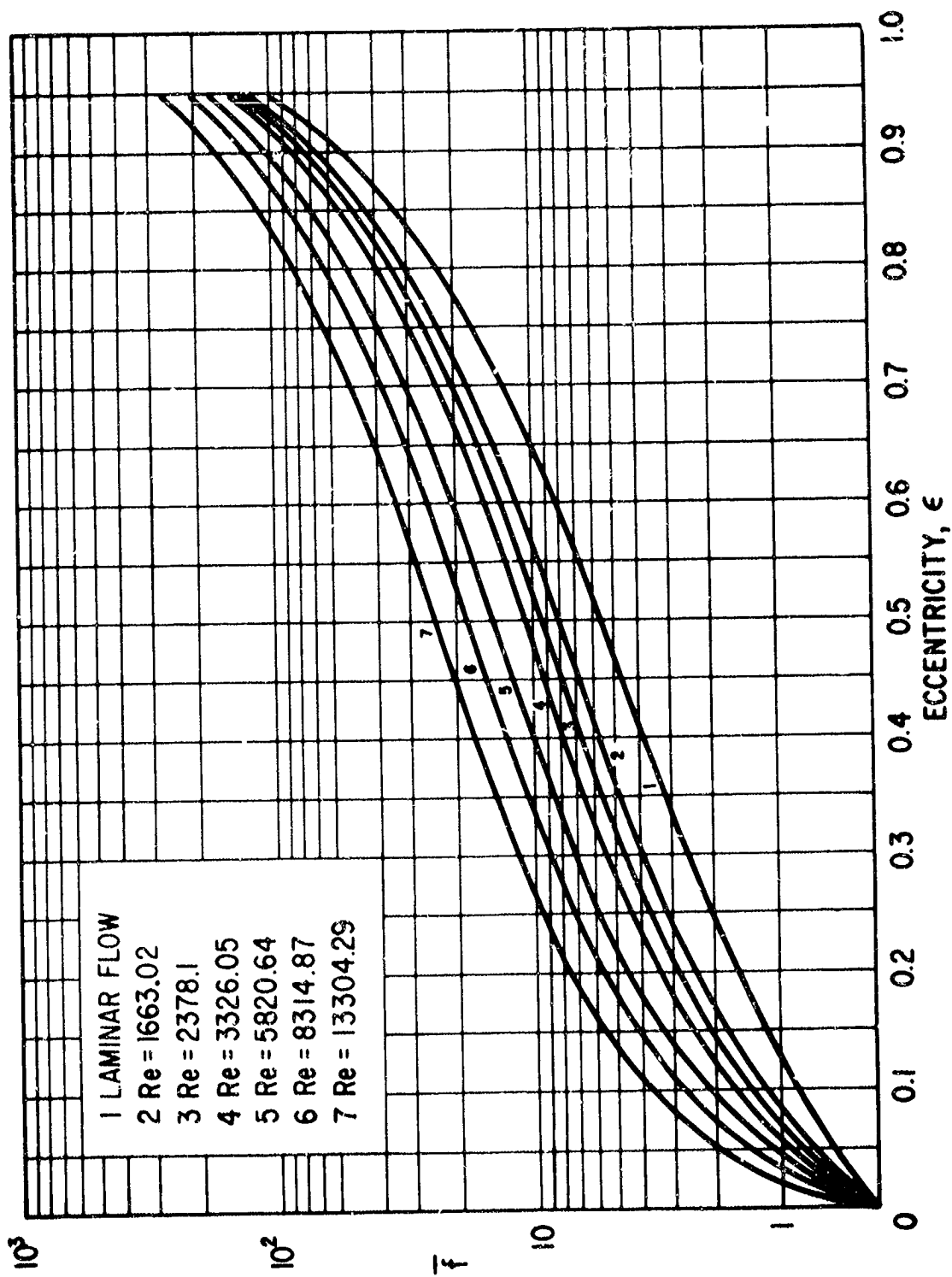
$$(B22) \quad C_x' = \mathcal{I} \left\{ \frac{ps - rq}{us - vq} \right\}$$

$$(B23) \quad C_y' = \mathcal{I} \left\{ \frac{-i(ps - rq)}{vp - ur} \right\}$$

The correlation between the experimental and theoretical characteristics of the test bearing can be achieved by comparing the theoretical and experimental effective stiffness and damping factors. The experimental effective stiffness and damping factors are calculated from motions measured at A and O' using Equations (B18) and (B19) while the theoretical K_x' , K_y' , C_x' and C_y' are determined by Equations (B20) through (B23).

REFERENCES

1. Wilcock, D.F., "Turbulence in High Speed Journal Bearings," Trans. A.S.M.E., Vol. 72, 1950.
2. Smith, M.I. and Fuller, D.D. "Journal Bearing Operation of Super-Laminar Speeds," ASME Paper 55 Lub-26, 1955.
3. Orcutt, F.K., "Investigation of a Partial Arc Pad Bearing in the Super-Laminar Flow Regime," ASME Paper 64-LubS-8 to be presented at Lubrication Symposium, Cleveland, April, 1964.
4. Ng, C.W. and Pan, C.H.T., "A Linearized Turbulent Lubrication Theory," MTI 63TR53, Dec. 19, 1963.
5. Arwas, E.B., Orcutt, F.K. and Vohr J.H., "Lubrication Analysis in Turbulent Regime, 2nd Quarterly Report on N.A.S.A. Contract NAS w-771," MTI Report 64TR3.
6. Lund, J.W., "Spring and Damping Coefficients for the Tilting Pad Journal Bearing," ASLE Paper 64AM-2B3 to be presented at the Annual Meeting, Chicago, May 1964.
7. Hagg, A.C. and Sankey, G.O., "Some Dynamic Properties of Oil Film Journal Bearings with Reference to Unbalance Vibration of Rotors," J. Appl. Mech. 302-306, June, 1956.
8. Lund, J.W., Discussion to ASME Paper No. 63-LubS-6, Warner, P. C. and Thoman, R.J. "The Effect of the 150 Degree Partial Bearing on Rotor-Unbalance Vibration".
9. Warner, P.C. and Thoman, R.J., "The Effect of the 150 Degree Partial Bearing on Rotor Unbalance Vibration," A.S.M.E. Paper 63-LubS-6.
10. Lund, J.W., "Attenuation of Bearing Transmitted Noise," Vol. 1 of Report on Bu Ships Contract Nobs - 86914, issued by Westinghouse Corporation, March, 1964.



FULL CIRCULAR BEARING

Fig. 1 Dimensionless Force vs. Eccentricity Ratio ($L/D = 1$)

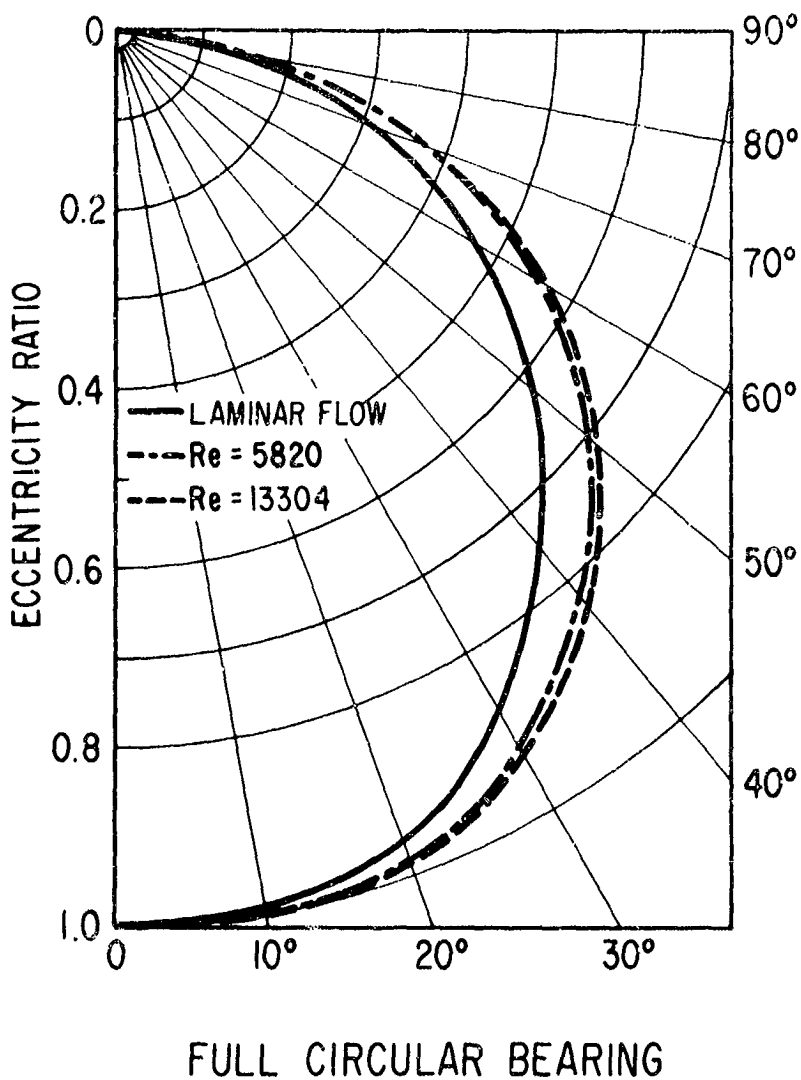


Fig. 2 Eccentricity Ratios - Attitude Angle Locus ($L/D = 1$)

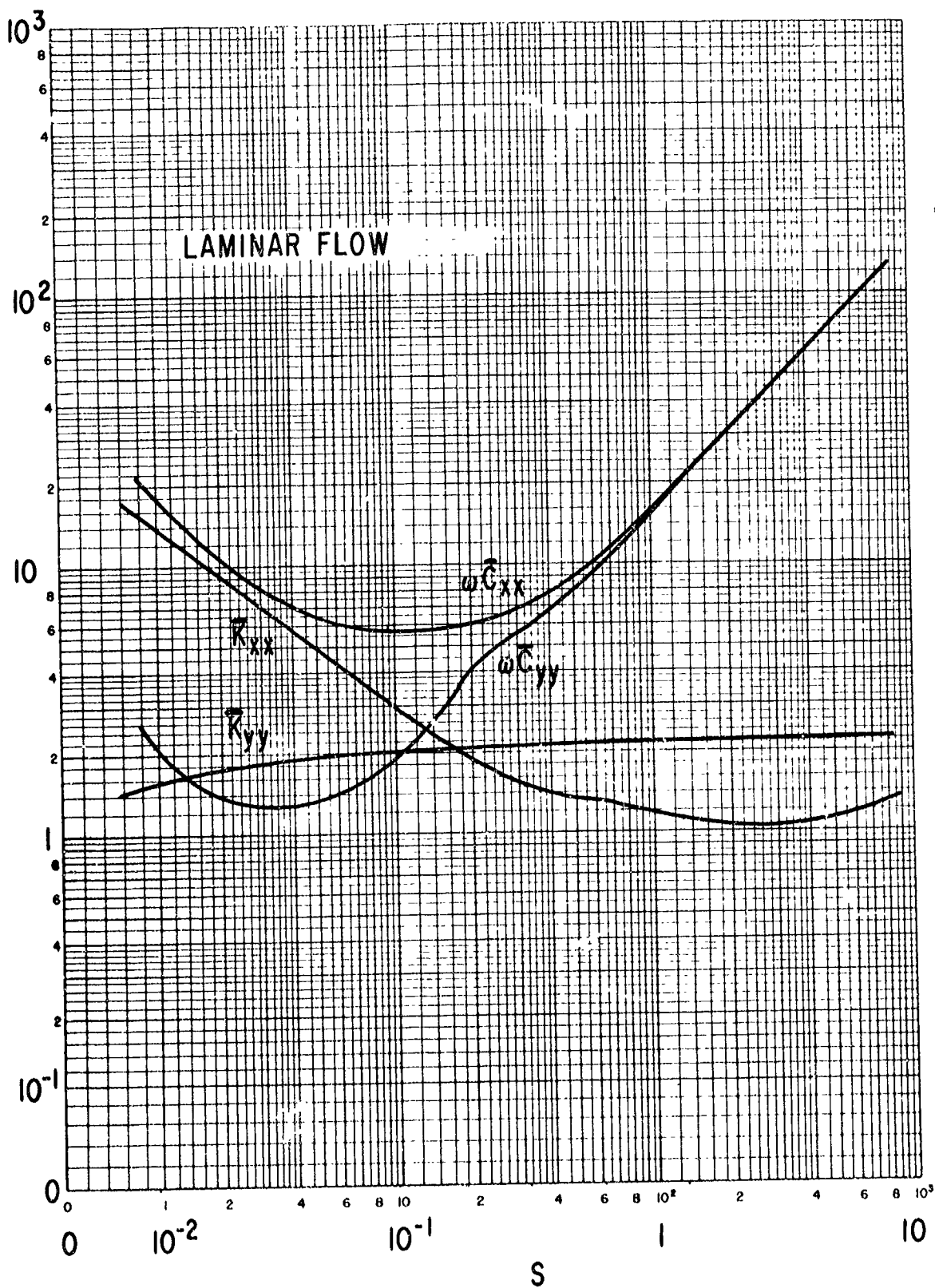


Fig. 3 Dimensionless Stiffness and Damping Coefficients for Full Circular Bearing ($L/D = 1$)

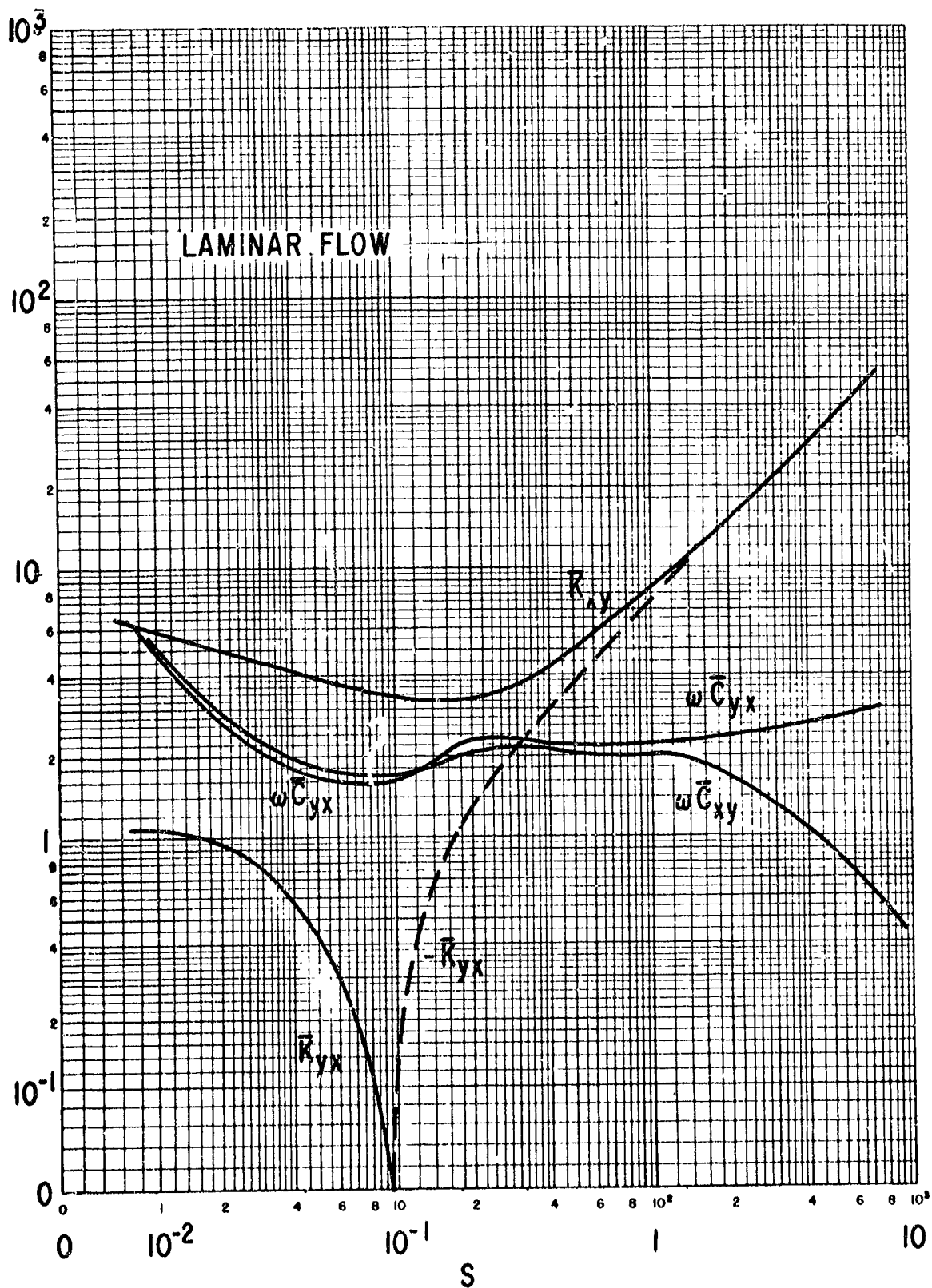


Fig. 4 Dimensionless Stiffness and Damping Coefficients
for Full Circular Bearings ($l/D = 1$)

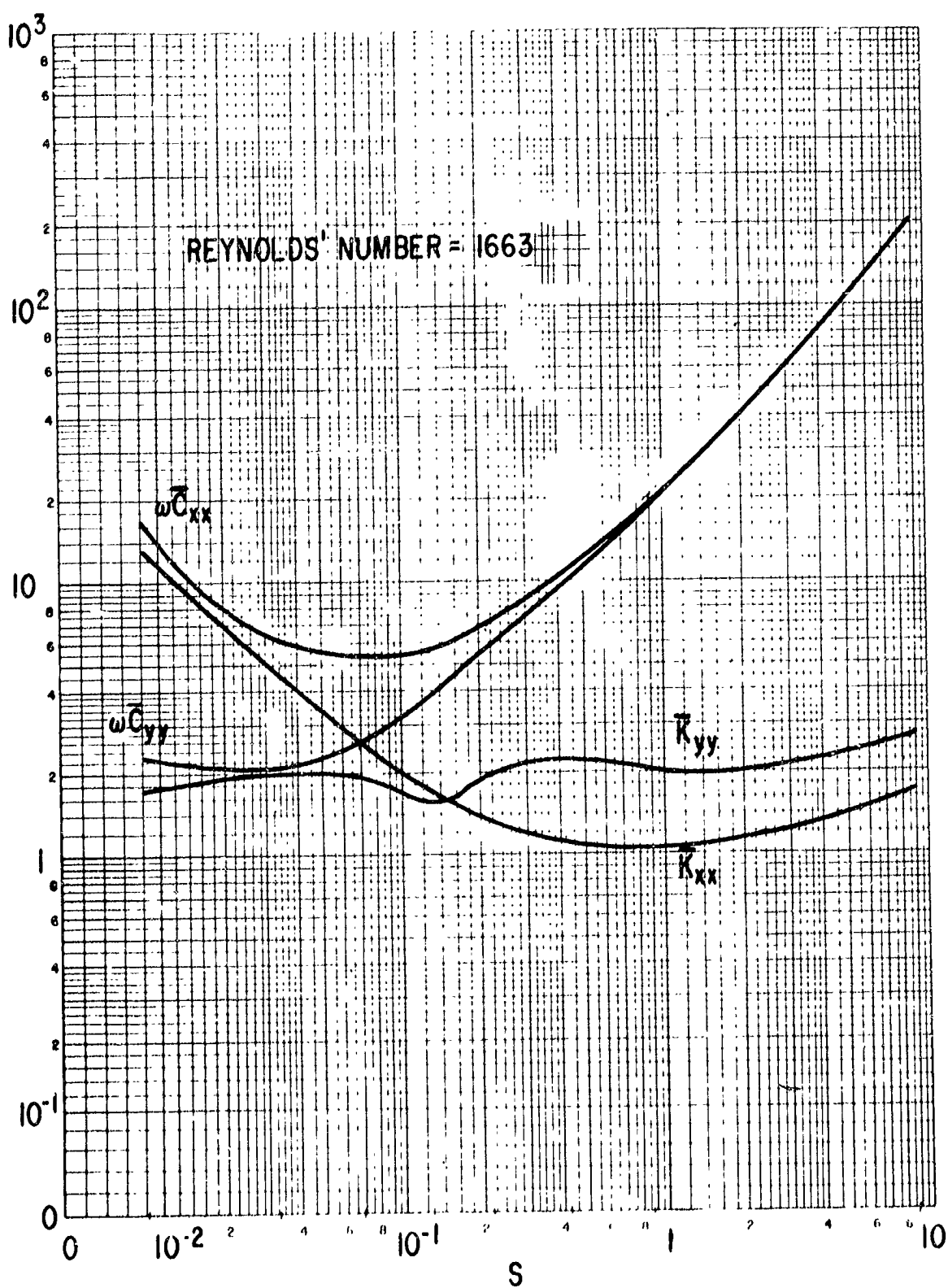


Fig. 5 Dimensionless Stiffness and Damping Coefficients for Full Circular Bearings ($L/D = 1$)

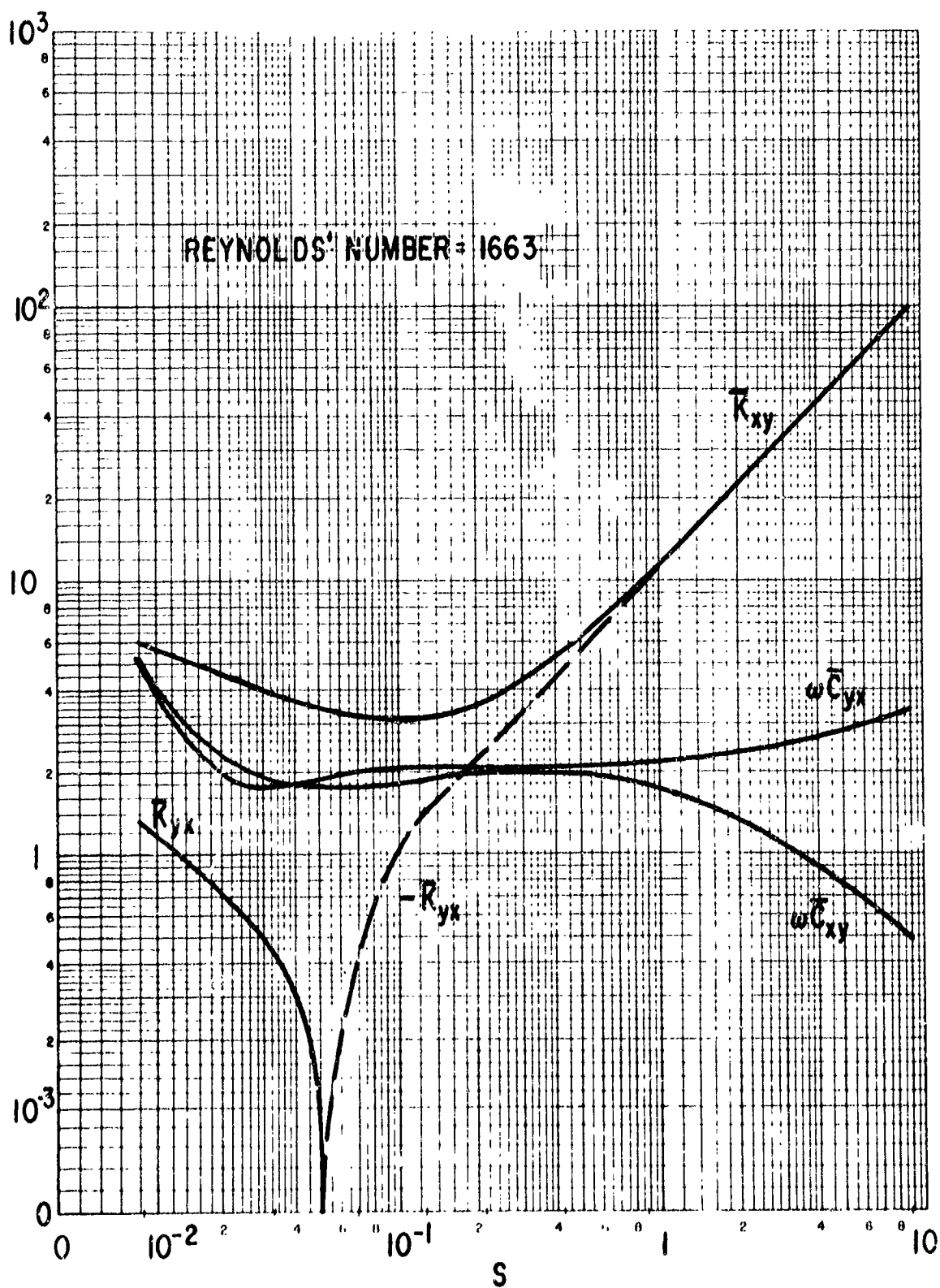


Fig. 6 Dimensionless Stiffness and Damping Coefficients for Full Circular Bearings ($L/D = 1$)

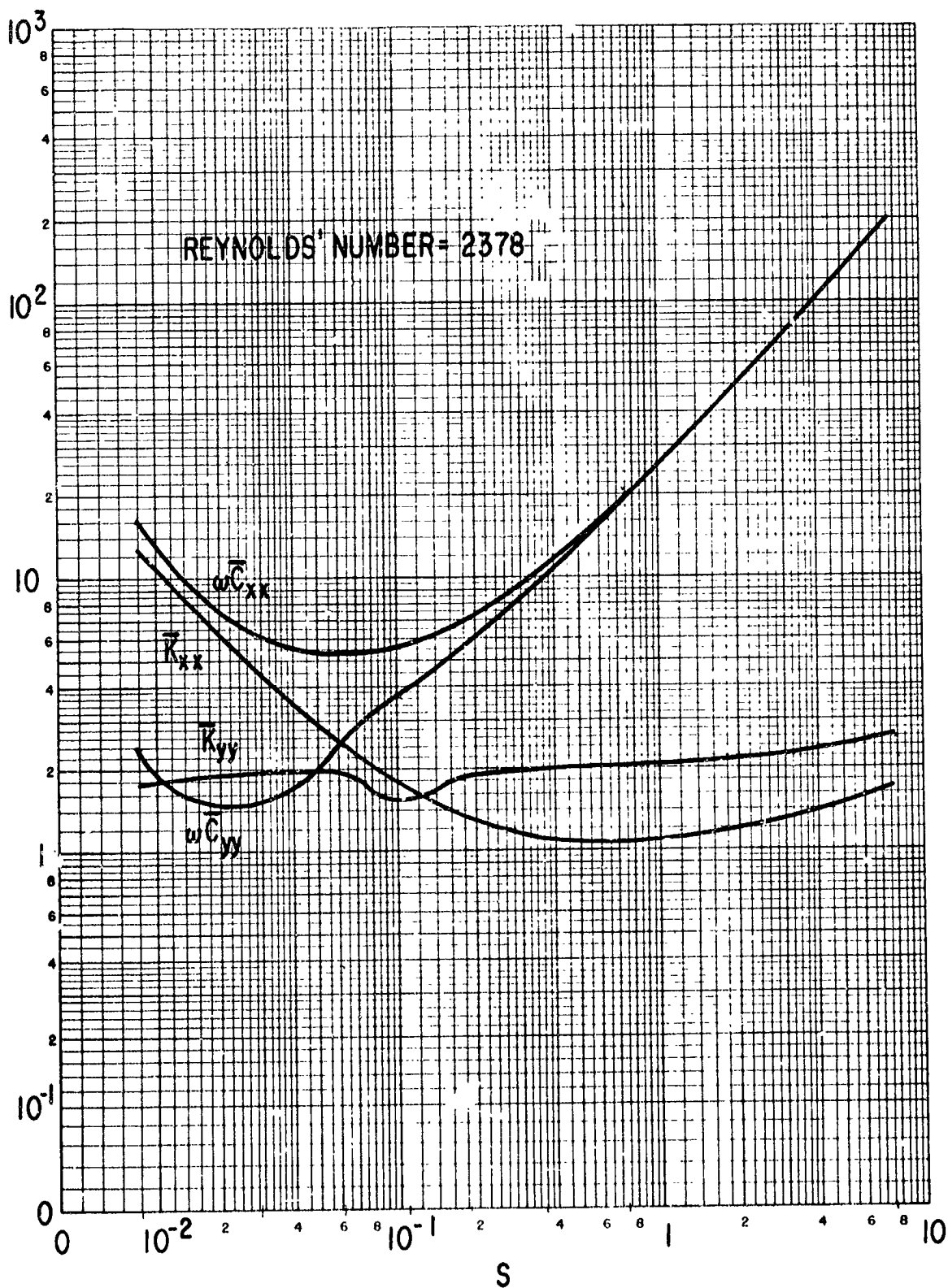


Fig. 7 Dimensionless Stiffness and Damping Coefficients for Full Circular Bearings ($L/D = 1$)

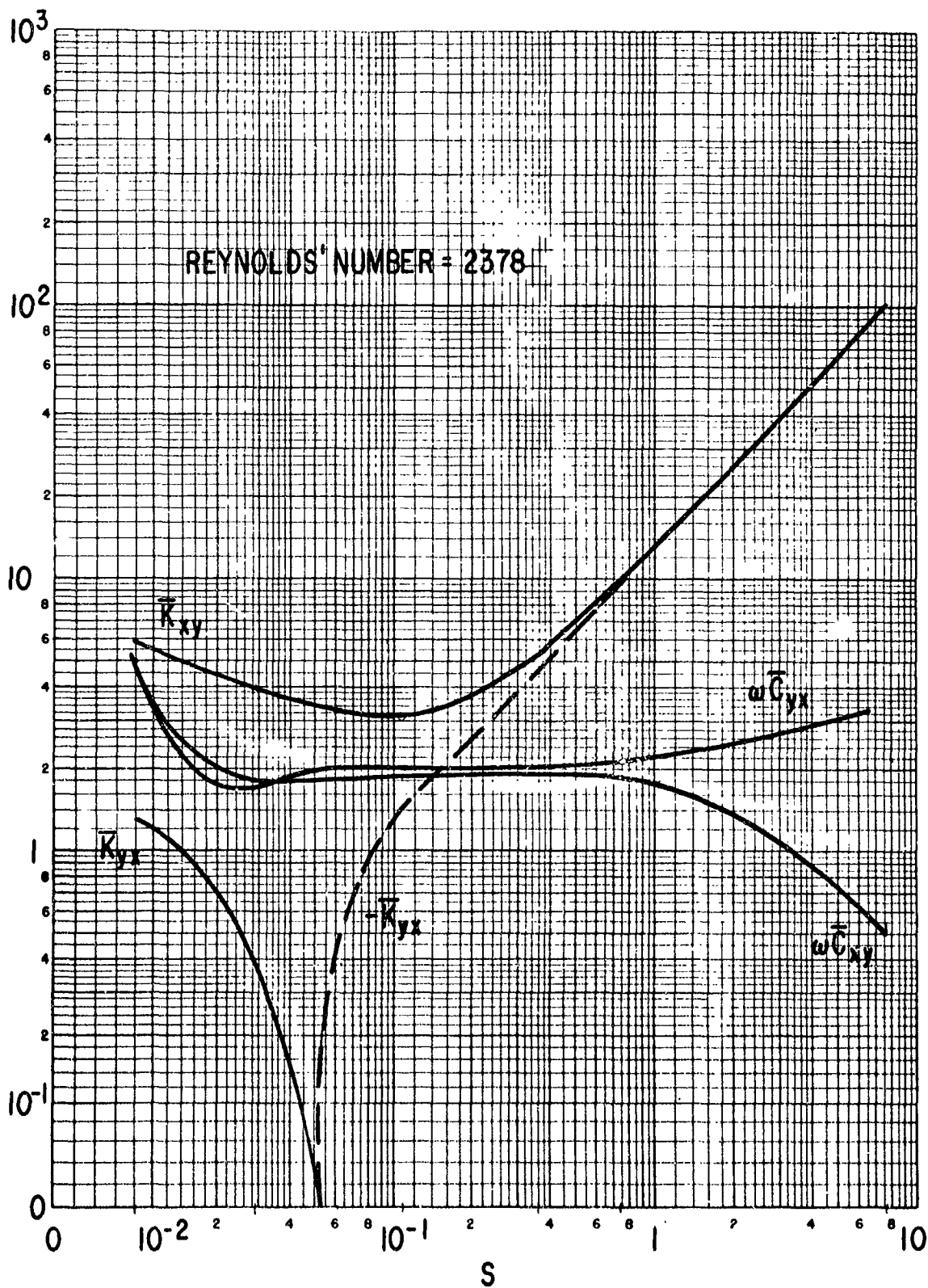


Fig. 8 Dimensionless Stiffness and Damping Coefficients
for Full Circular Bearings ($l/D = 1$)

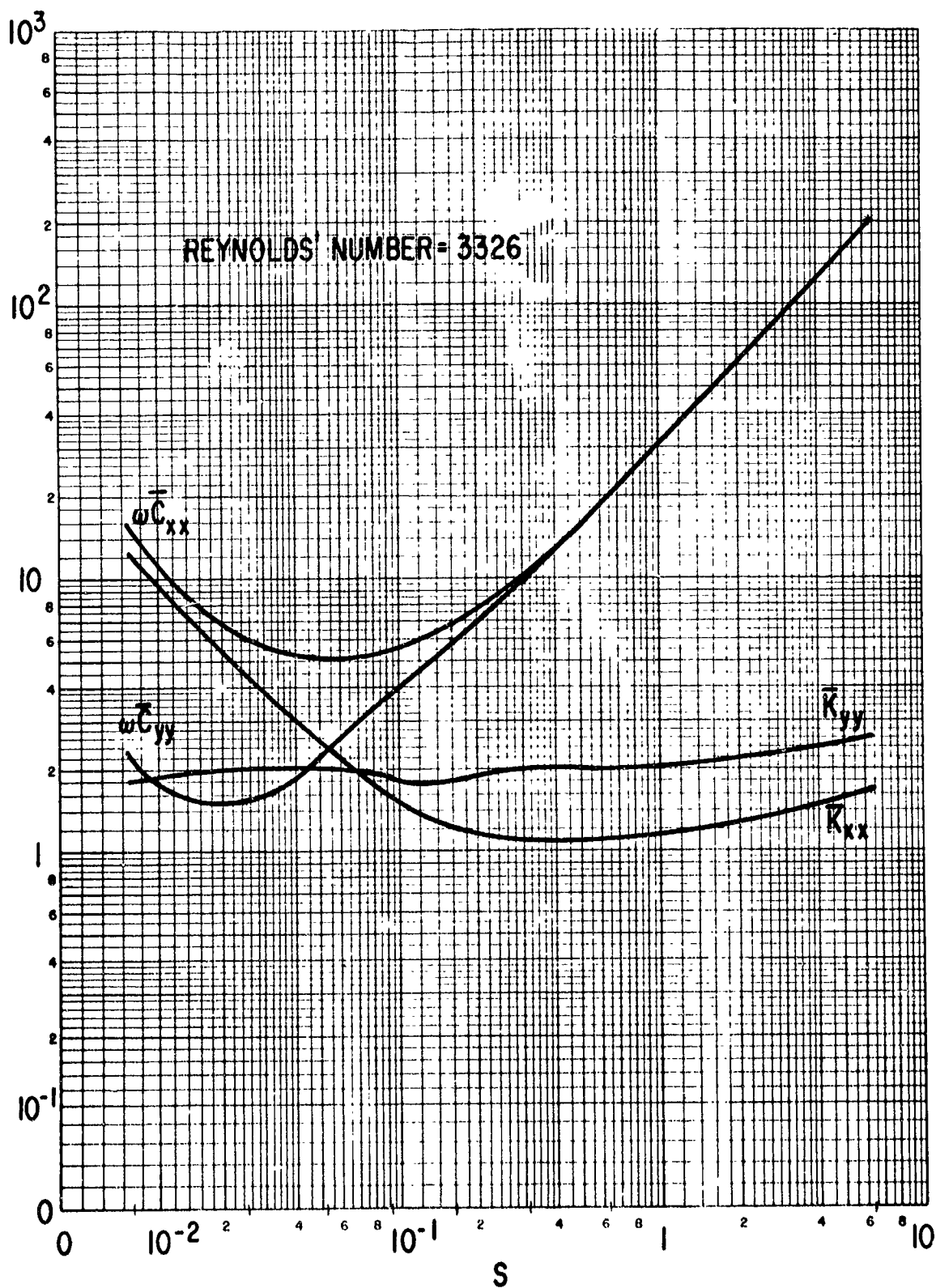


Fig. 9 Dimensionless Stiffness and Damping Coefficients for Full Circular Bearings ($L/D = 1$)

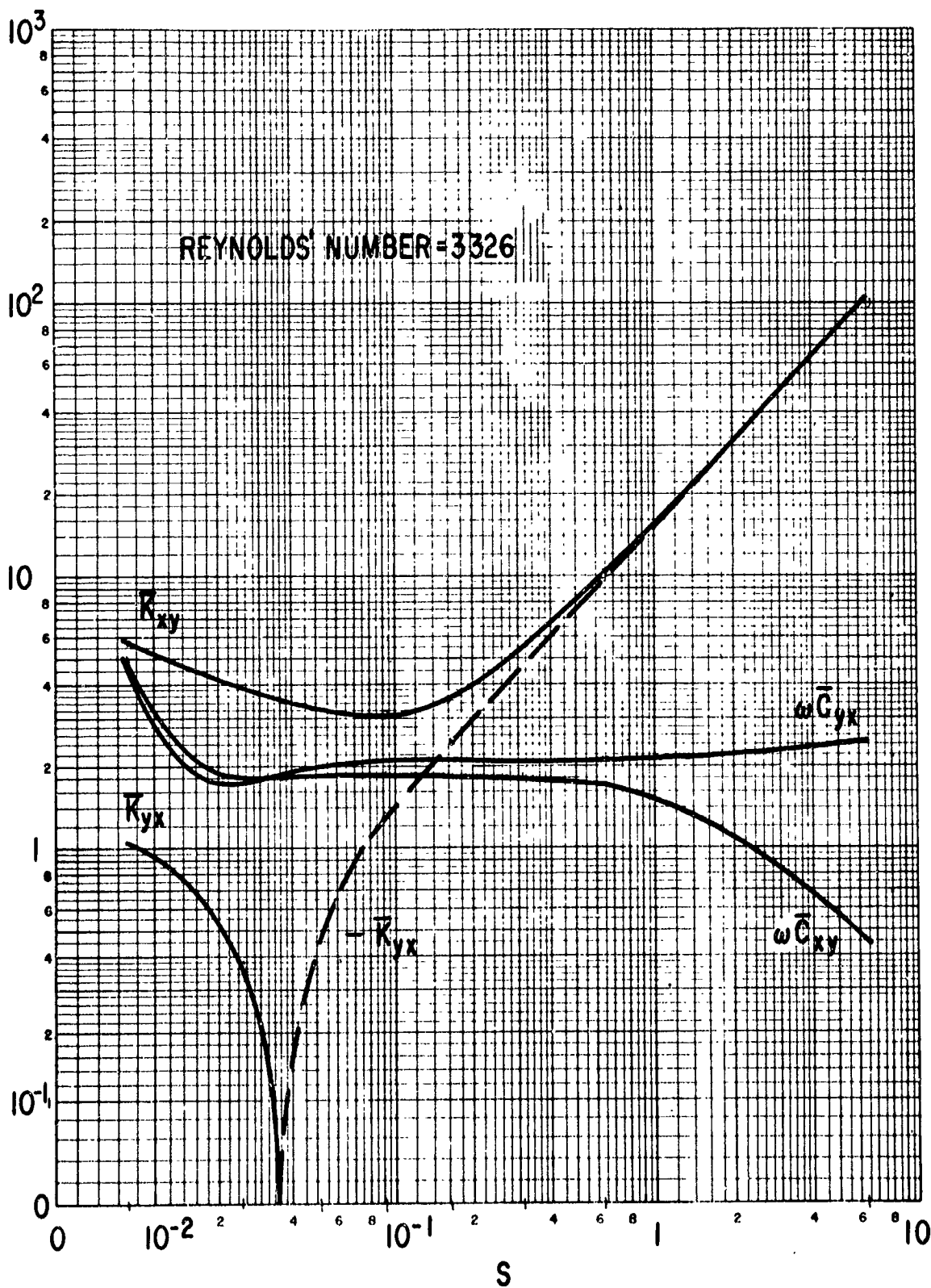


Fig. 10 Dimensionless Stiffness and Damping Coefficients for Full Circular Bearings ($L/D = 1$)

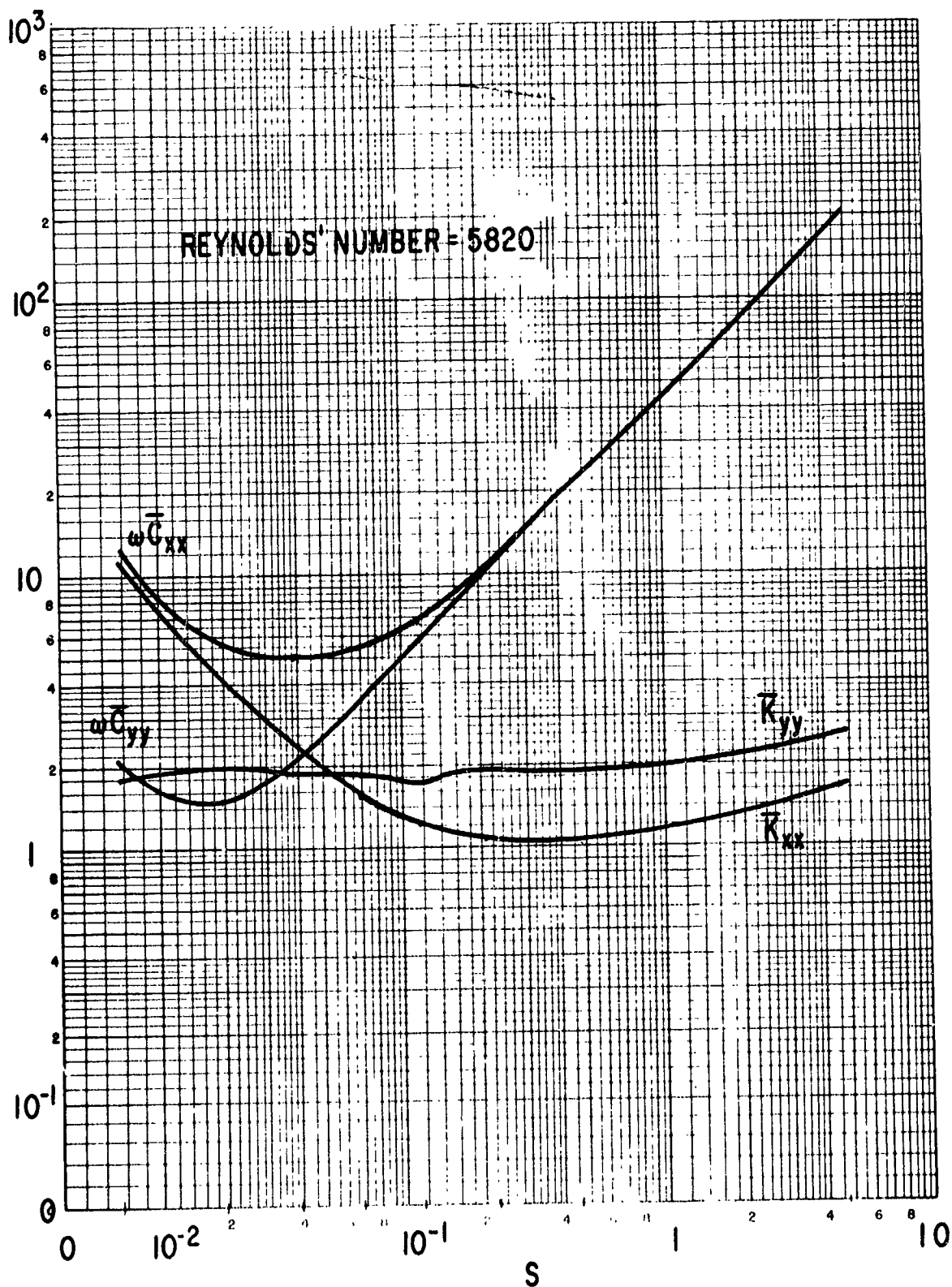


Fig. 11 Dimensionless Stiffness and Damping Coefficients for Full Circular Bearings ($L/D = 1$)

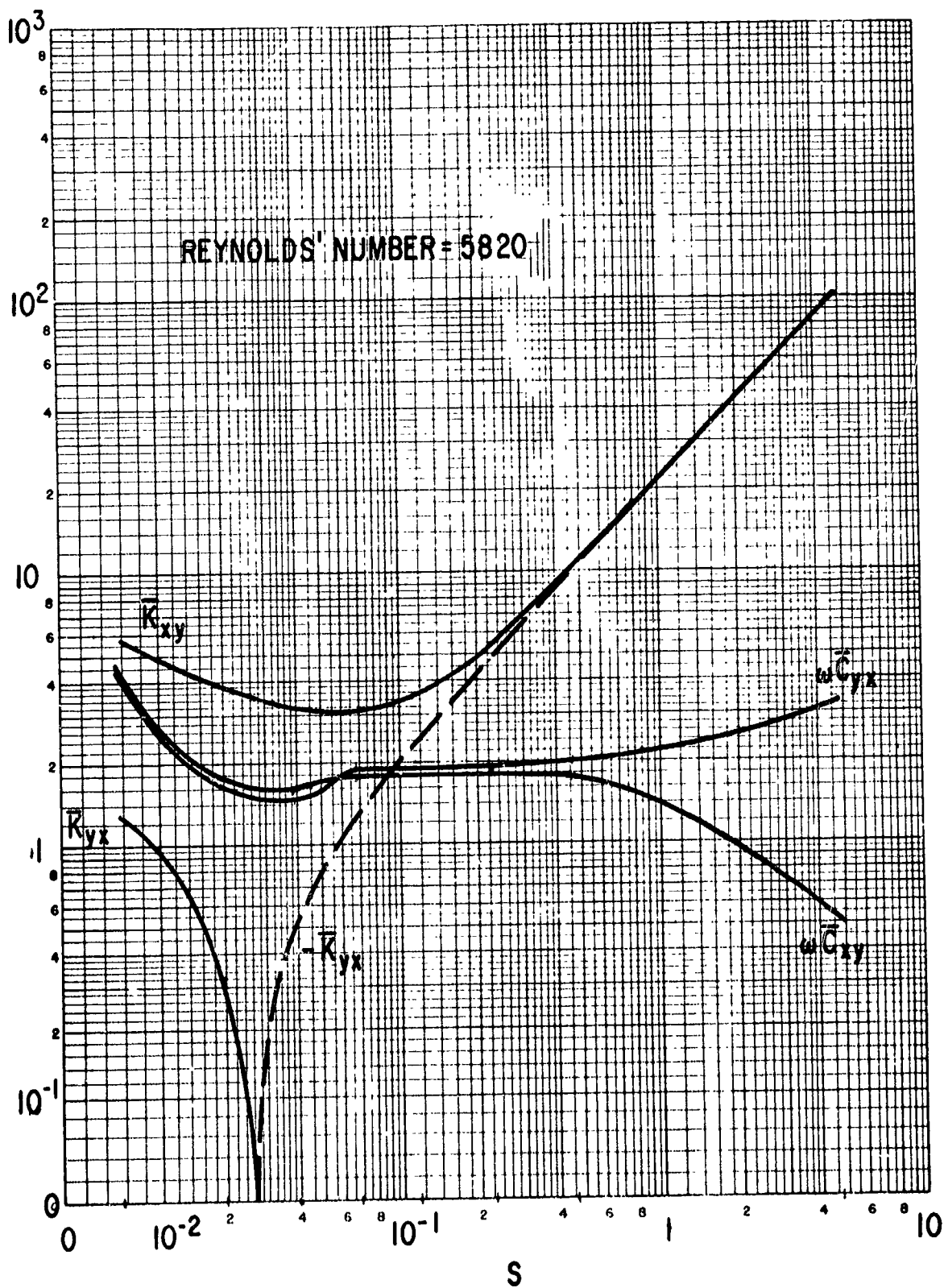


Fig 12 Dimensionless Stiffness and Damping Coefficients for Full Circular Bearings ($l/D = 1$)

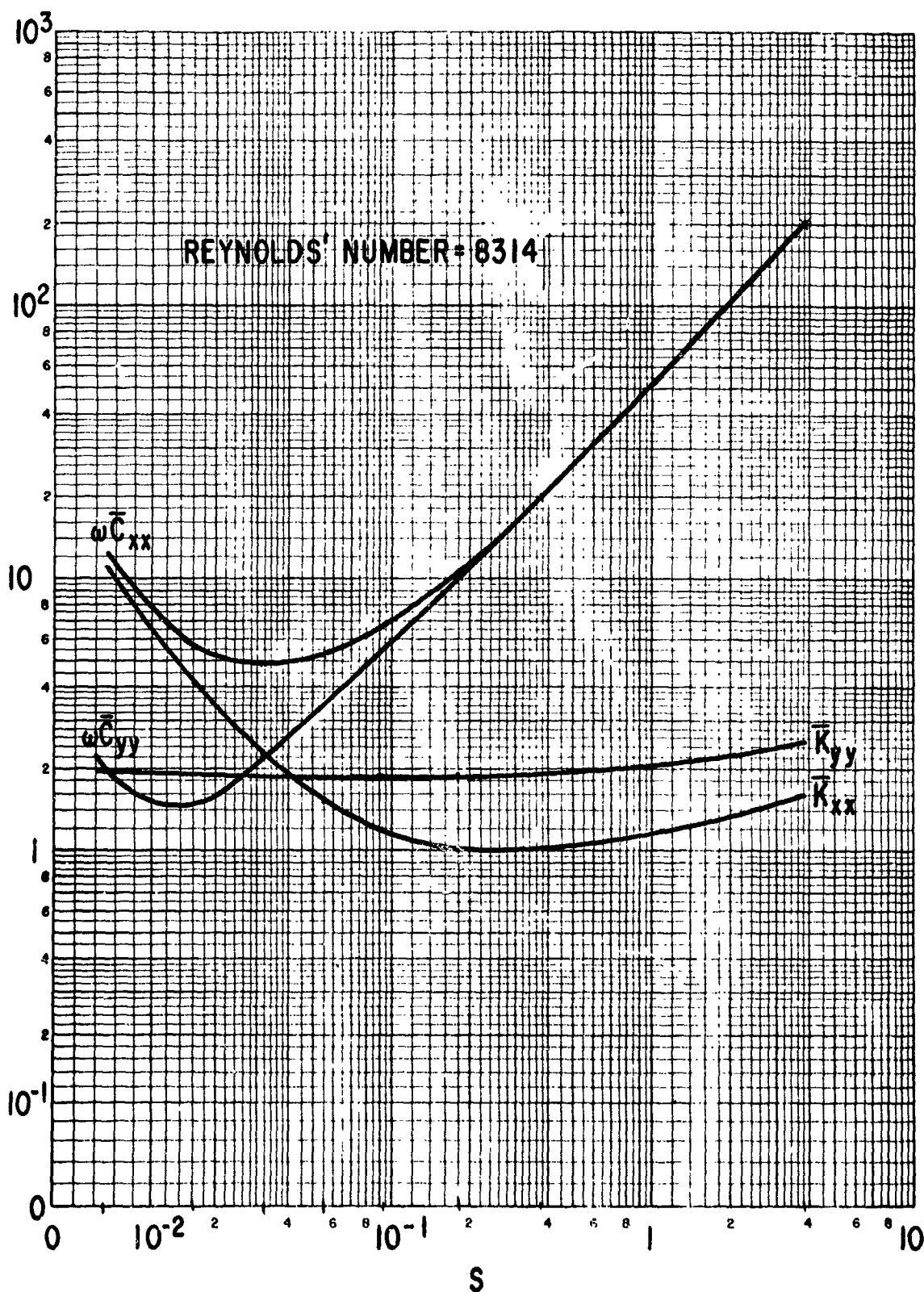


Fig. 13 Dimensionless Stiffness and Damping Coefficients for Full Circular Bearings ($L/D = 1$)

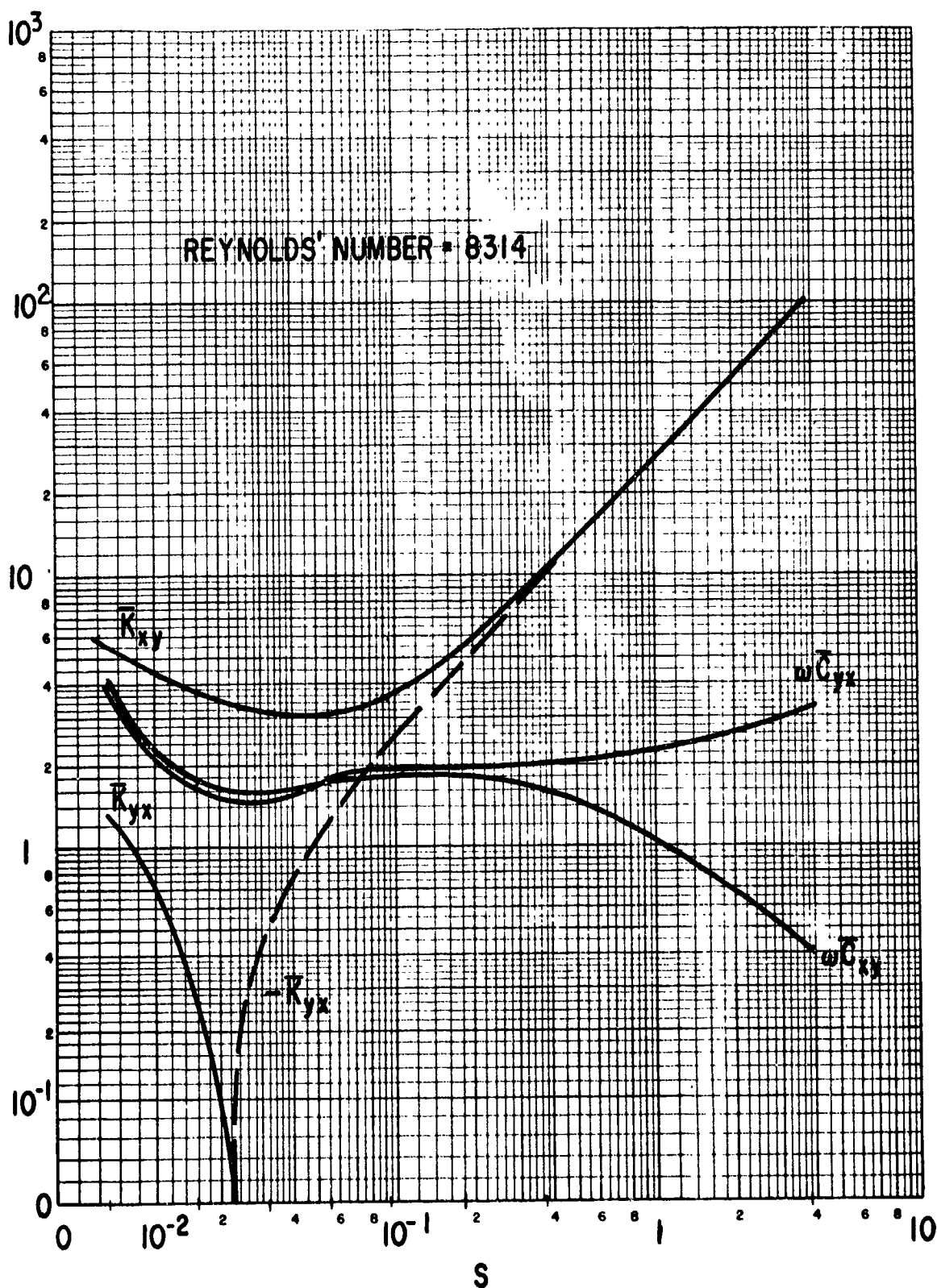


Fig. 14 Dimensionless Stiffness and Damping Coefficients for Full Circular Bearings ($L/D = 1$)

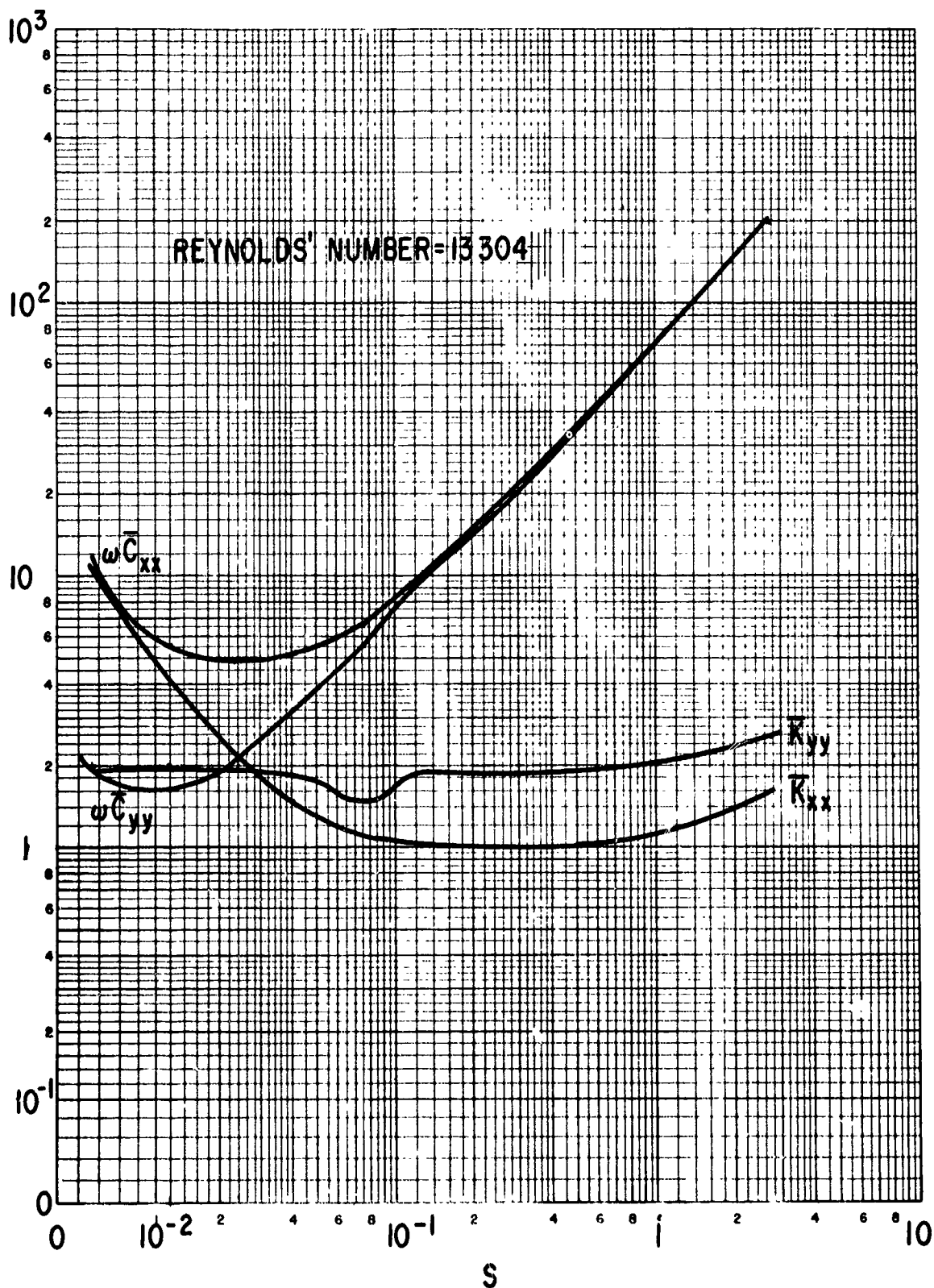


Fig. 15 Dimensionless Stiffness and Damping Coefficients for Full Circular Bearings ($L/D = 1$)

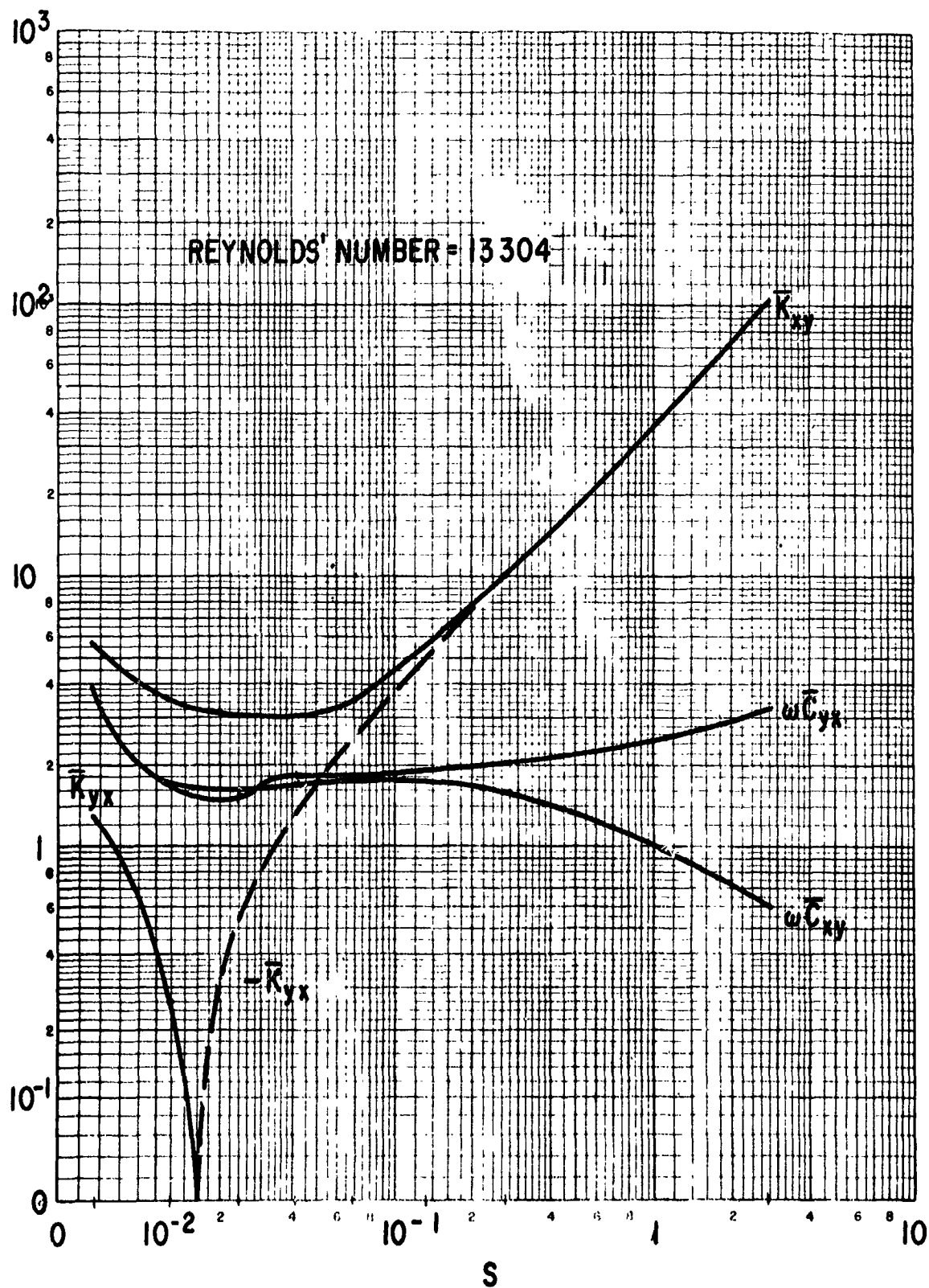
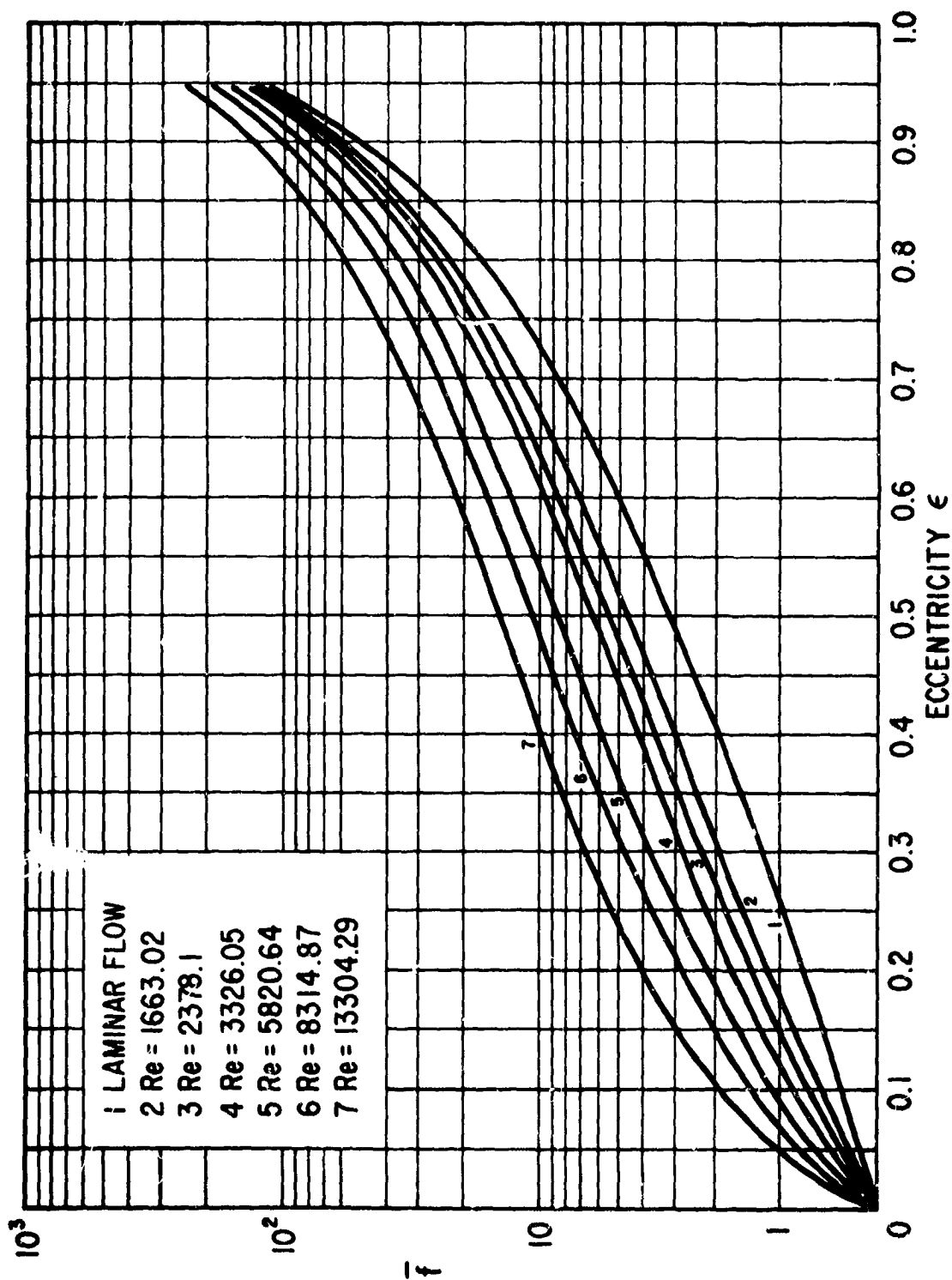
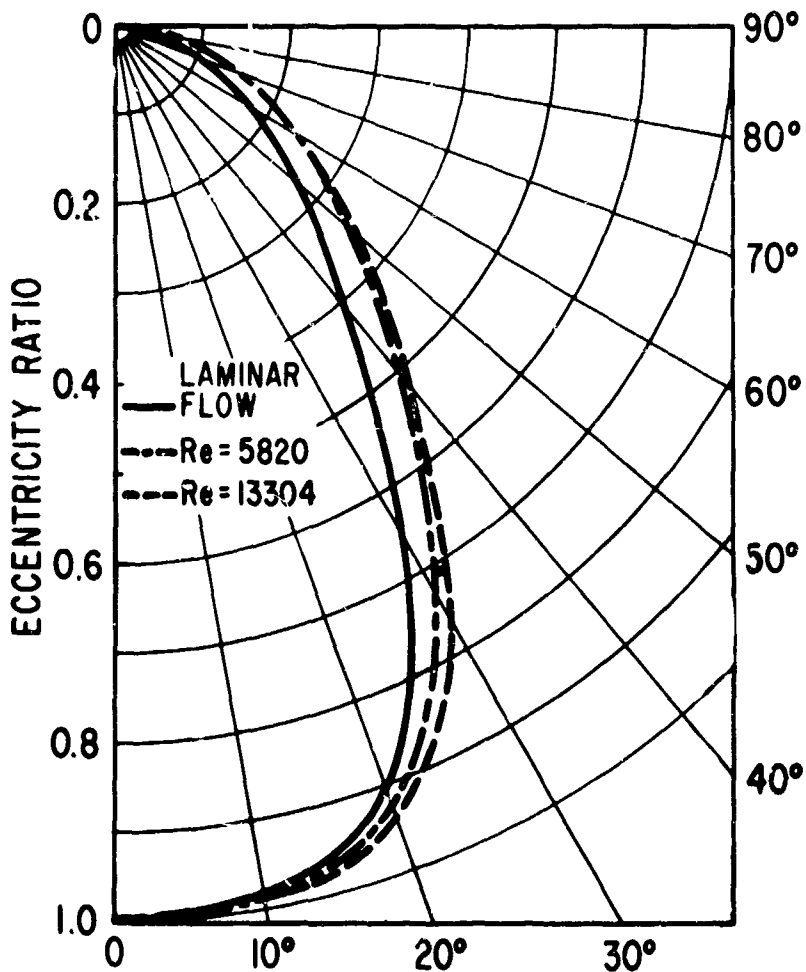


Fig. 16 Dimensionless Stiffness and Damping Coefficients for Full Circular Bearings ($L/D = 1$)



CENTRALLY LOADED, 100° ARC BEARING

Fig. 17 Dimensionless Force vs. Eccentricity Ratio ($L/D = 1$)



CENTRALLY LOADED, 100° ARC BEARING

Fig. 18 Eccentricity Ratios - Attitude Angle Locus

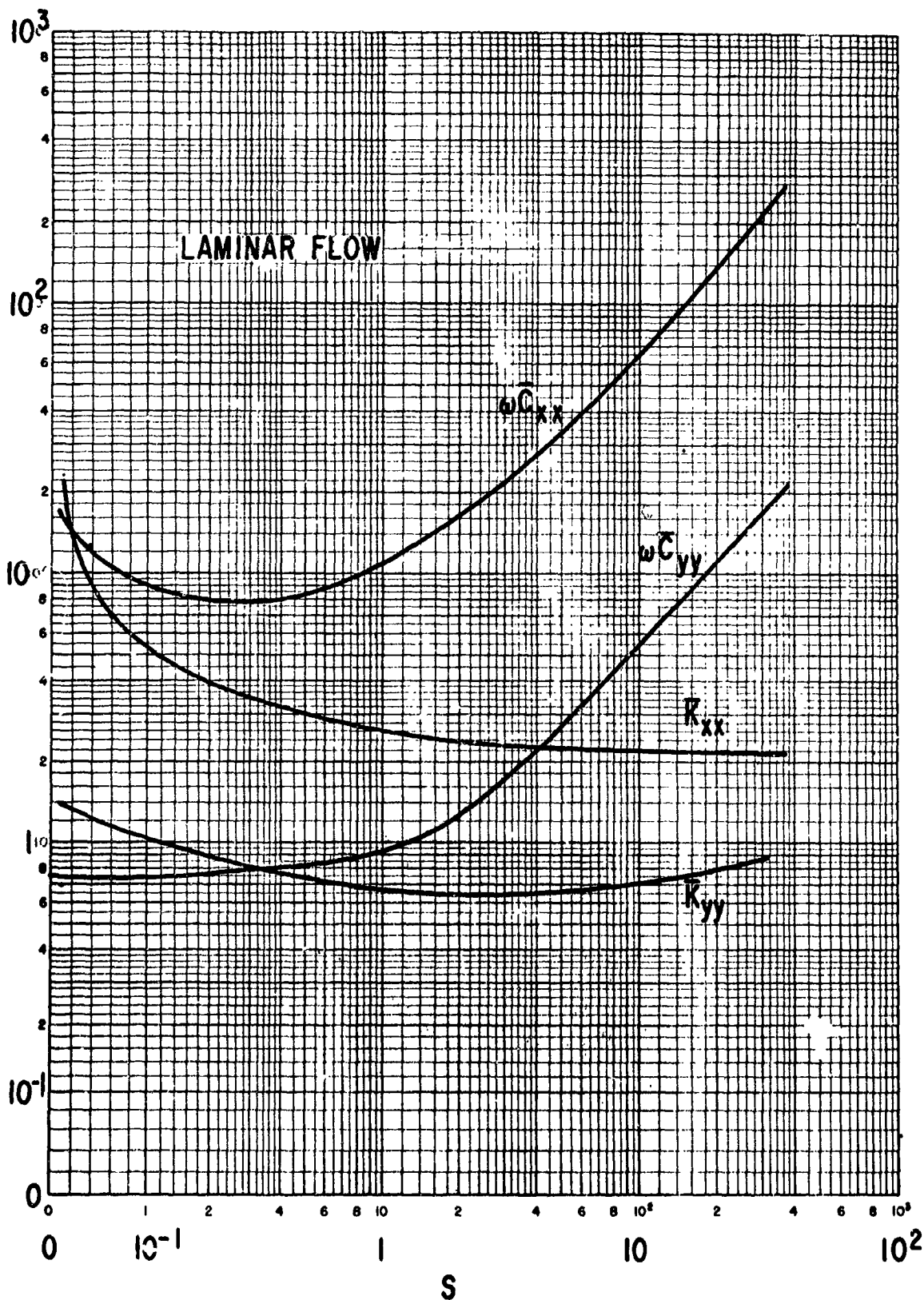


Fig. 19 Dimensionless Stiffness and Damping Coefficients for Centrally Loaded, 100° Arc Bearings ($L/D = 1$)

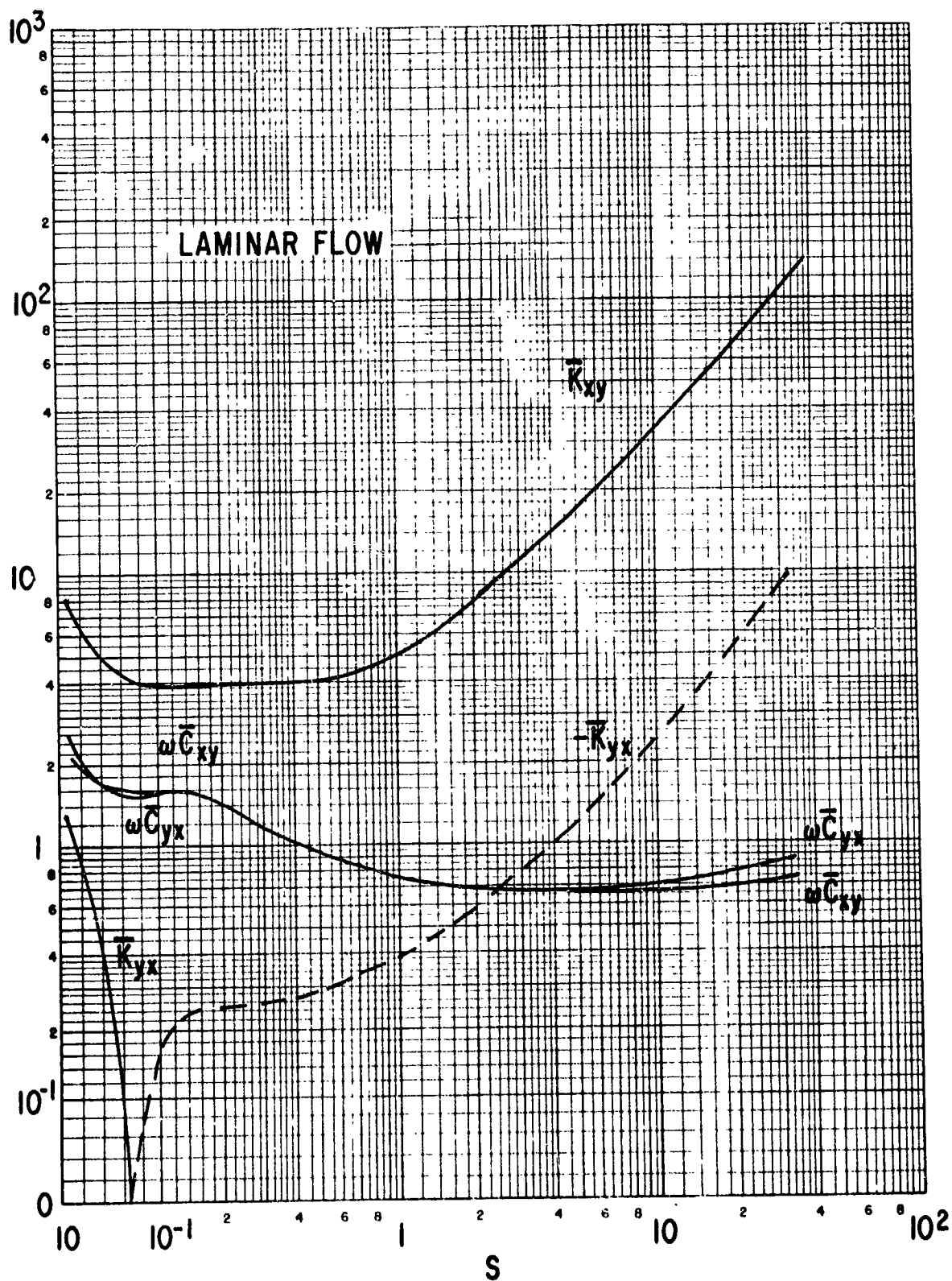


Fig. 20 Dimensionless Stiffness and Damping Coefficients
for Centrally Loaded, 100° Arc Bearings ($L/D = 1$)

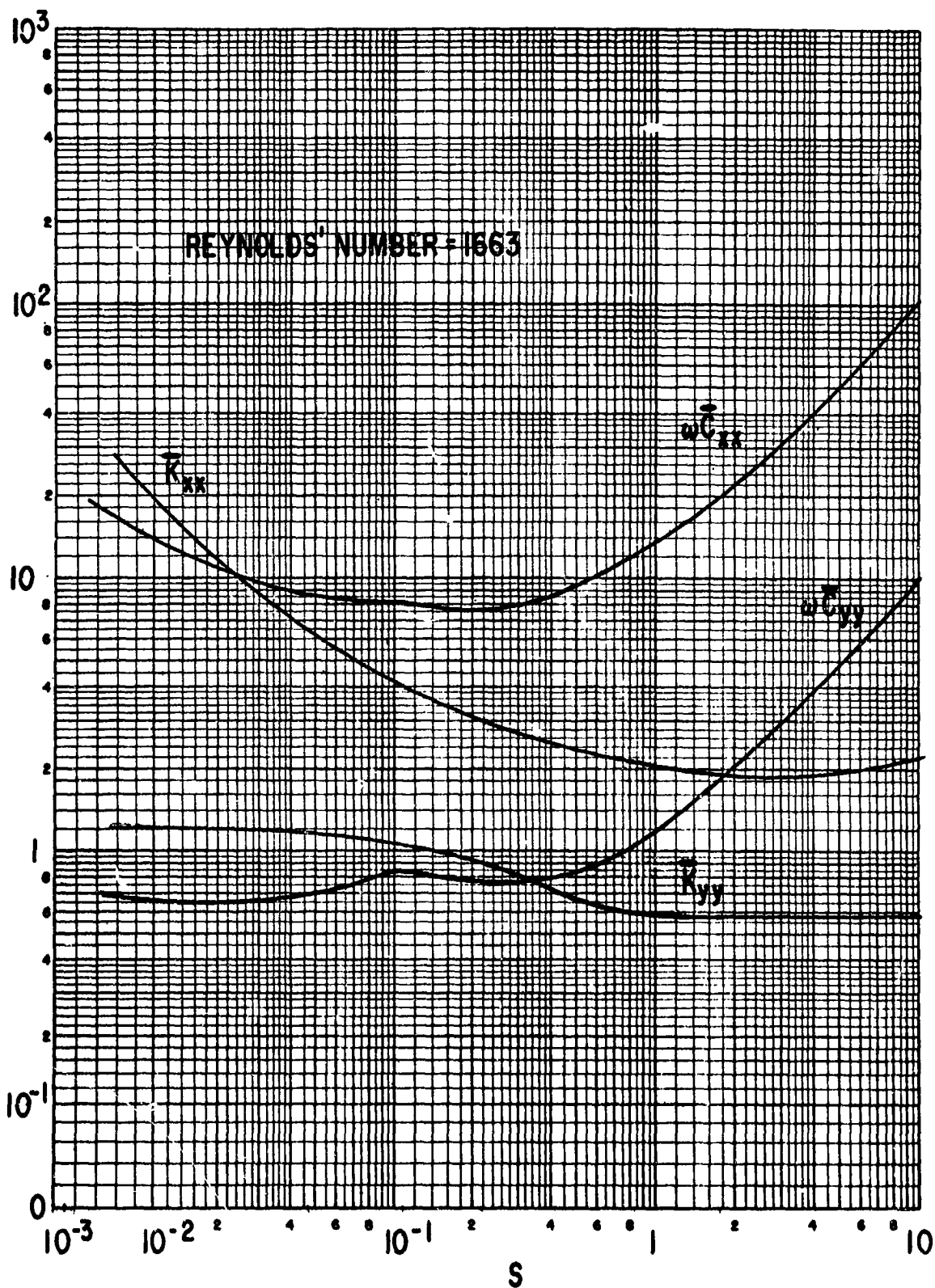


Fig. 21 Dimensionless Stiffness and Damping Coefficients for Centrally Loaded, 100° Arc Bearings ($L/D = 1$)

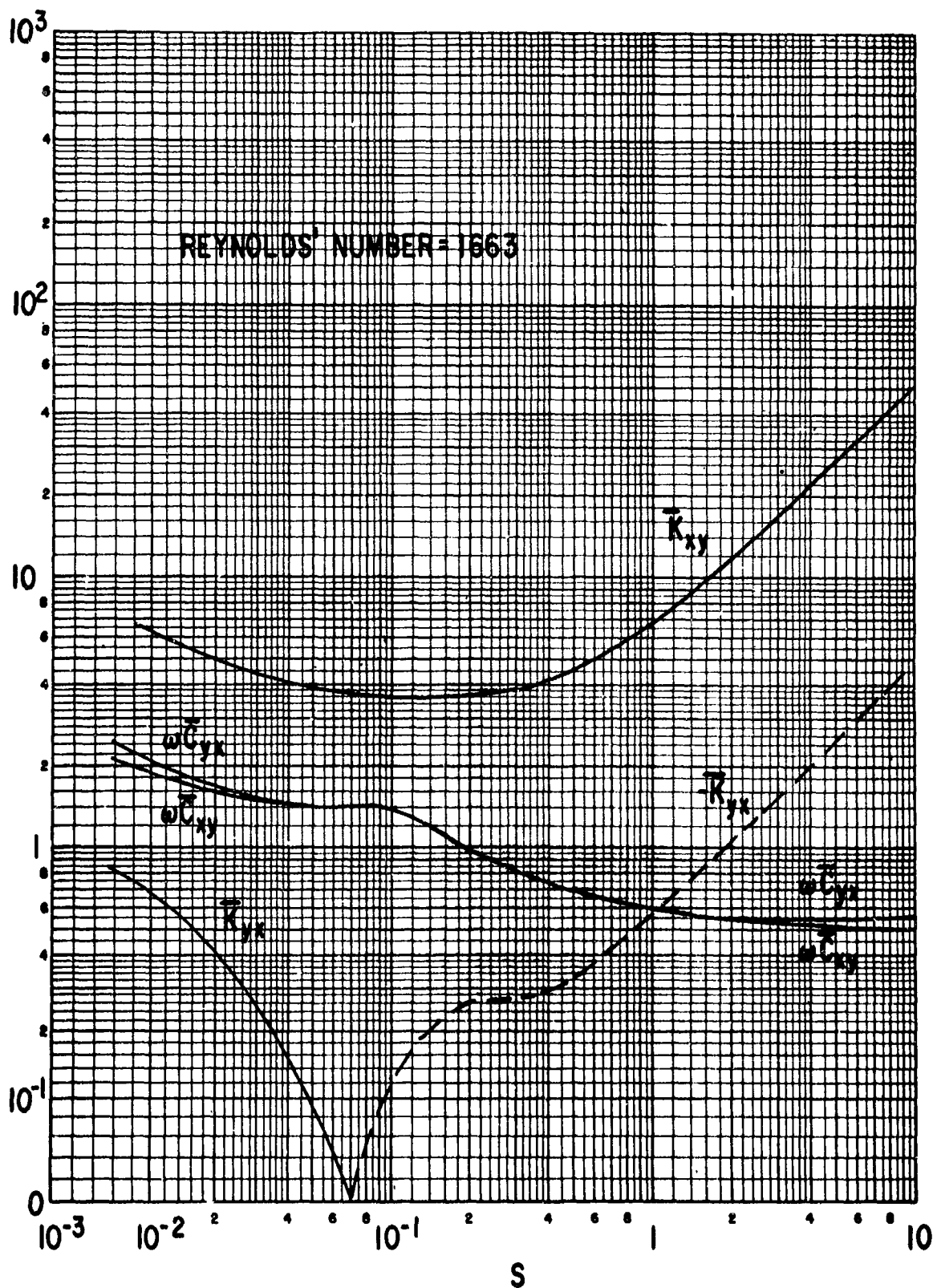


Fig. 22 Dimensionless Stiffness and Damping Coefficients for Centrally Loaded, 100° Arc Bearings ($l/D = 1$)

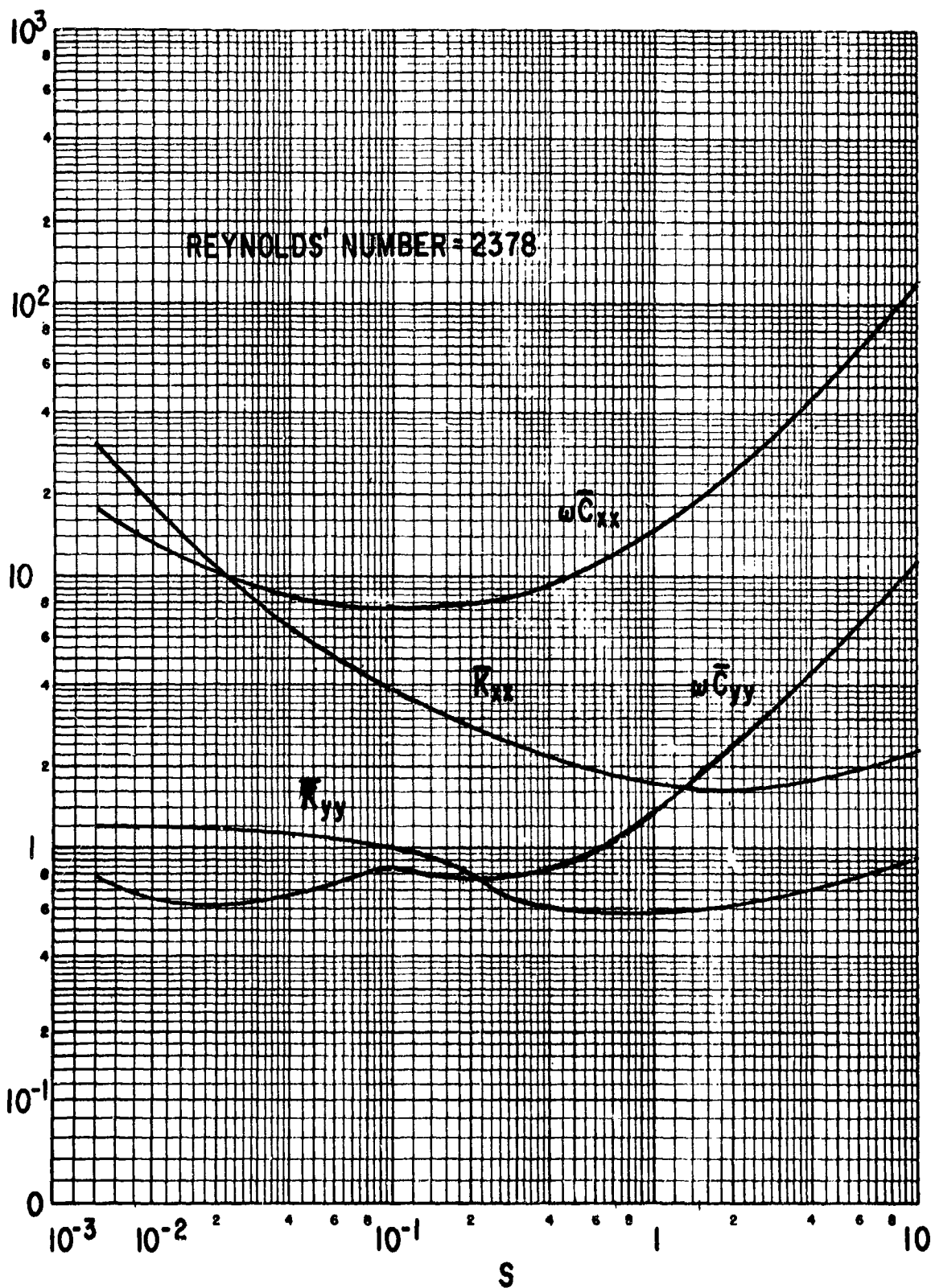


Fig. 23 Dimensionless Stiffness and Damping Coefficients for Centrally Loaded, 100° Arc Bearings ($L/D = 1$)

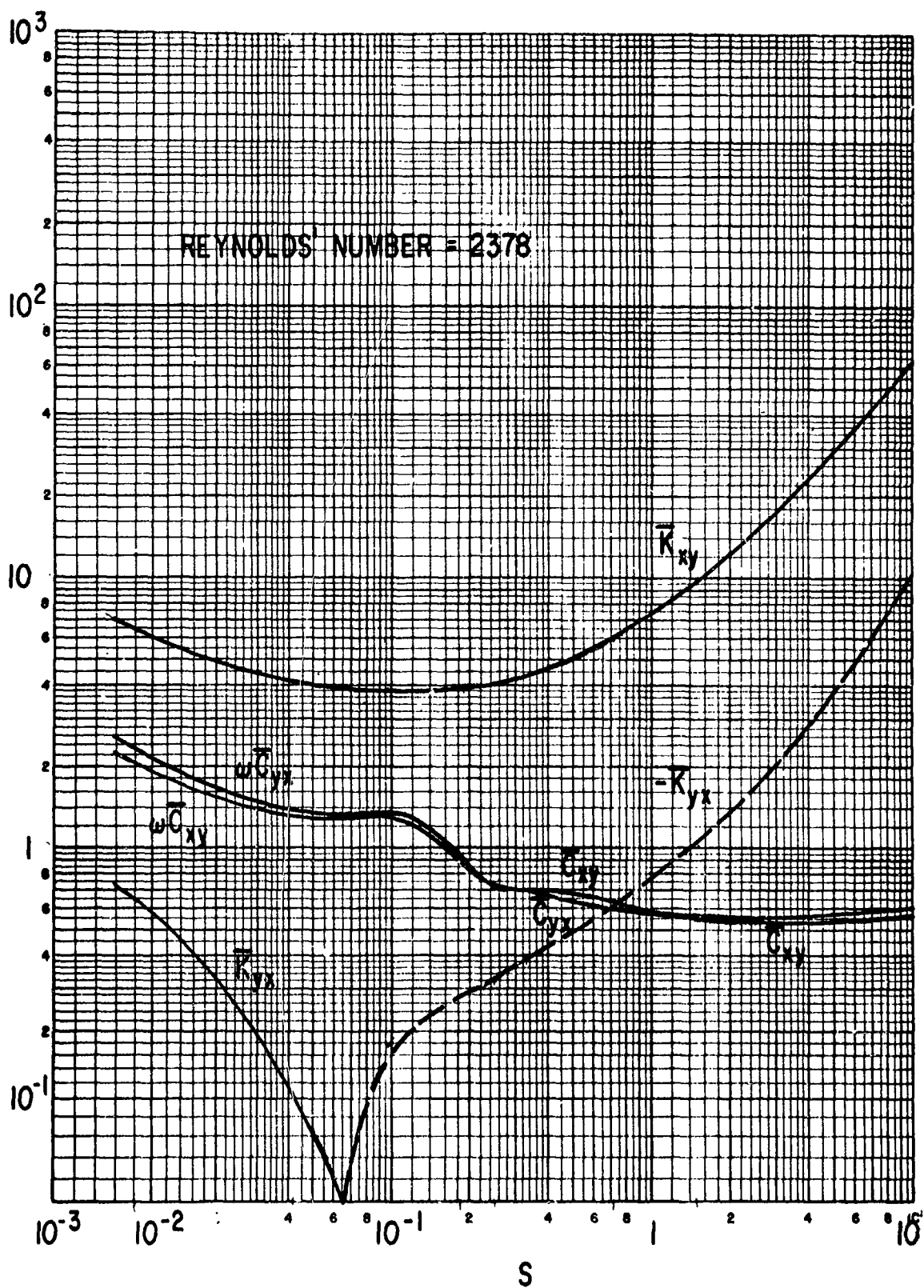


Fig. 24 Dimensionless Stiffness and Damping Coefficients for Centrally Loaded, 100° Arc Bearings ($L/D = 1$)

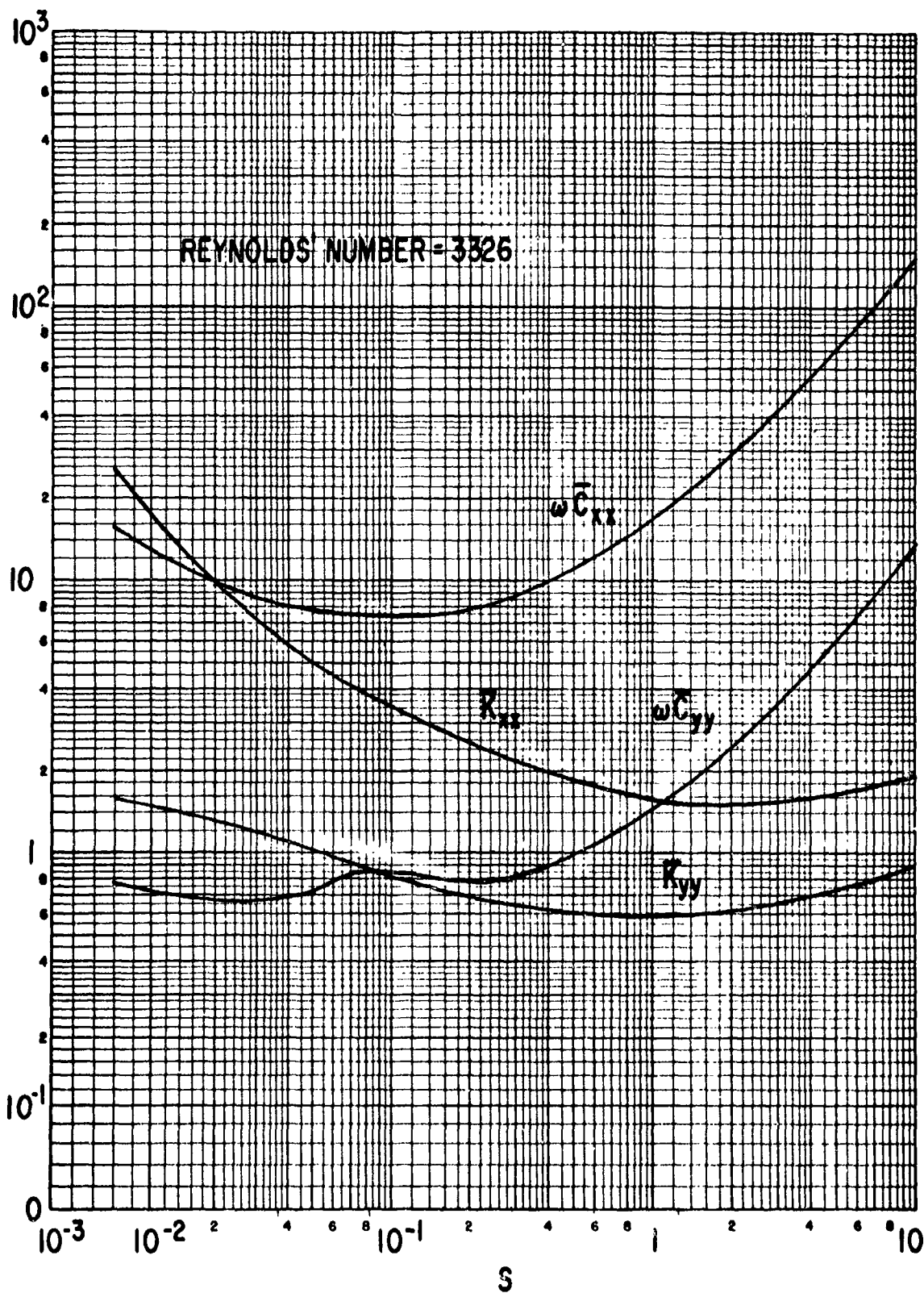


Fig. 25 Dimensionless Stiffness and Damping Coefficients for Centrally Loaded, 100° Arc Bearings ($L/D = 1$)

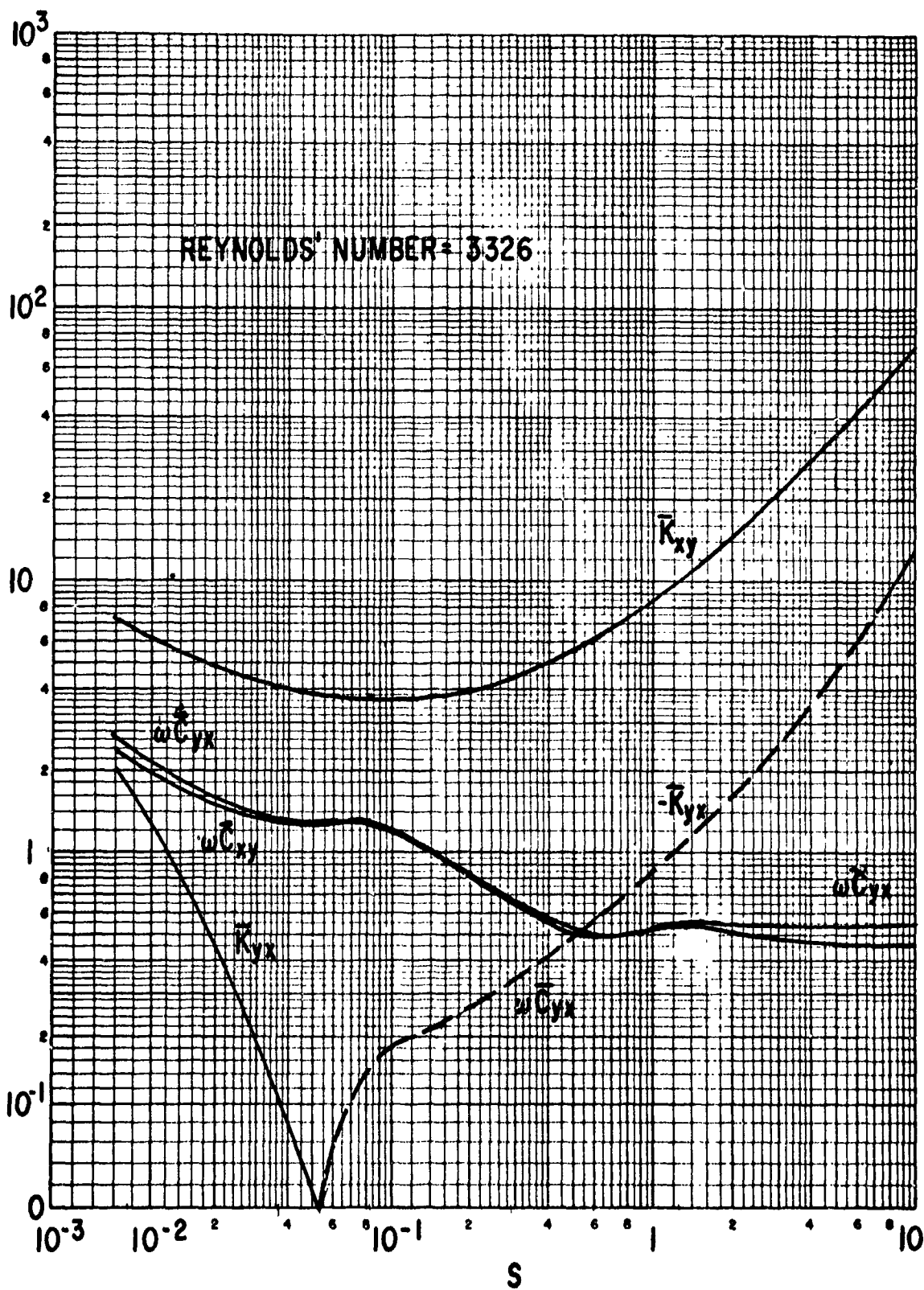


Fig. 26 Dimensionless Stiffness and Damping Coefficients for Centrally Loaded, 100° Arc Bearings ($L/D = 1$)

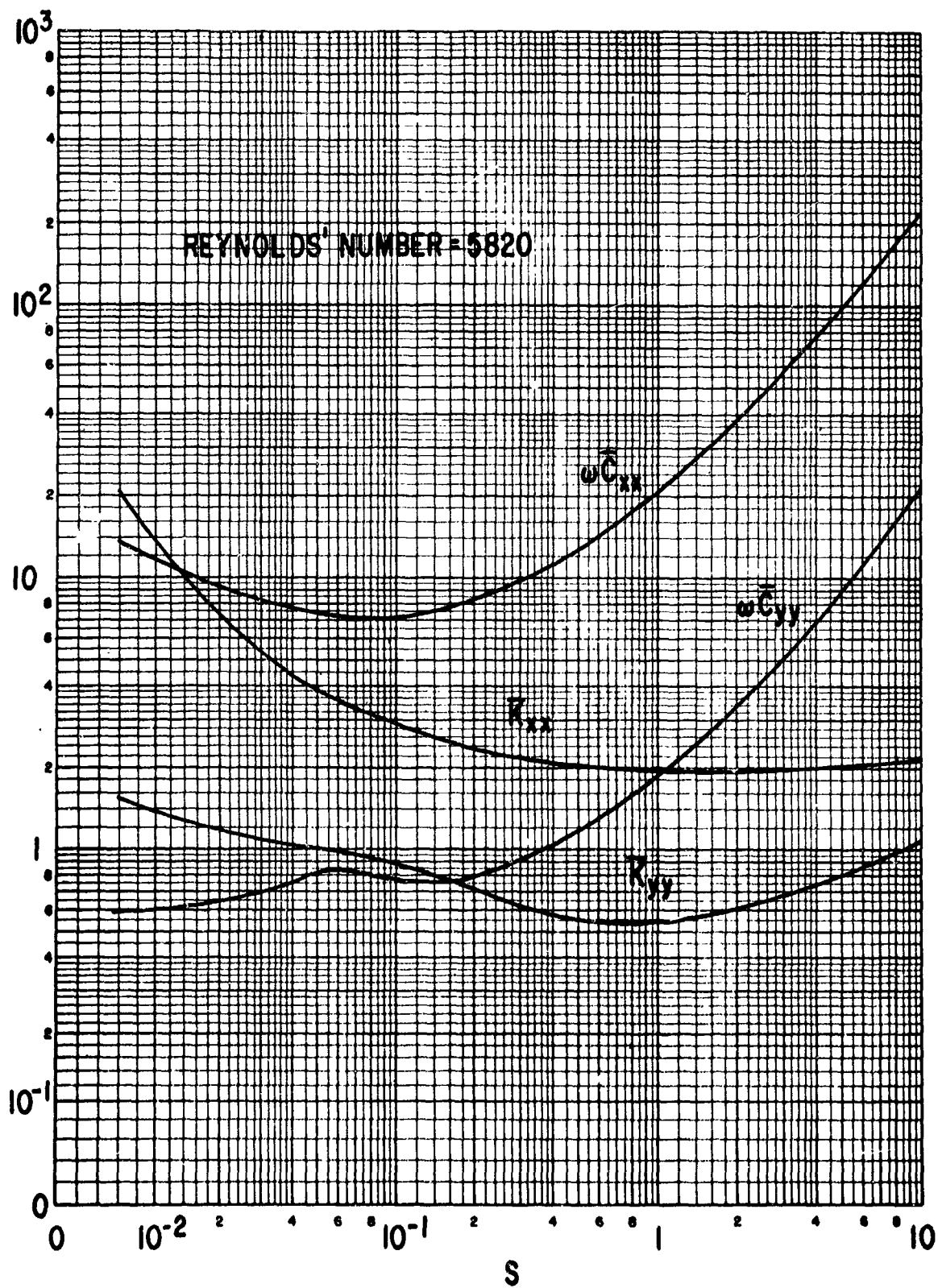


Fig. 27 Dimensionless Stiffness and Damping Coefficients for Centrally Loaded, 100° Arc Bearings ($L/D = 1$)

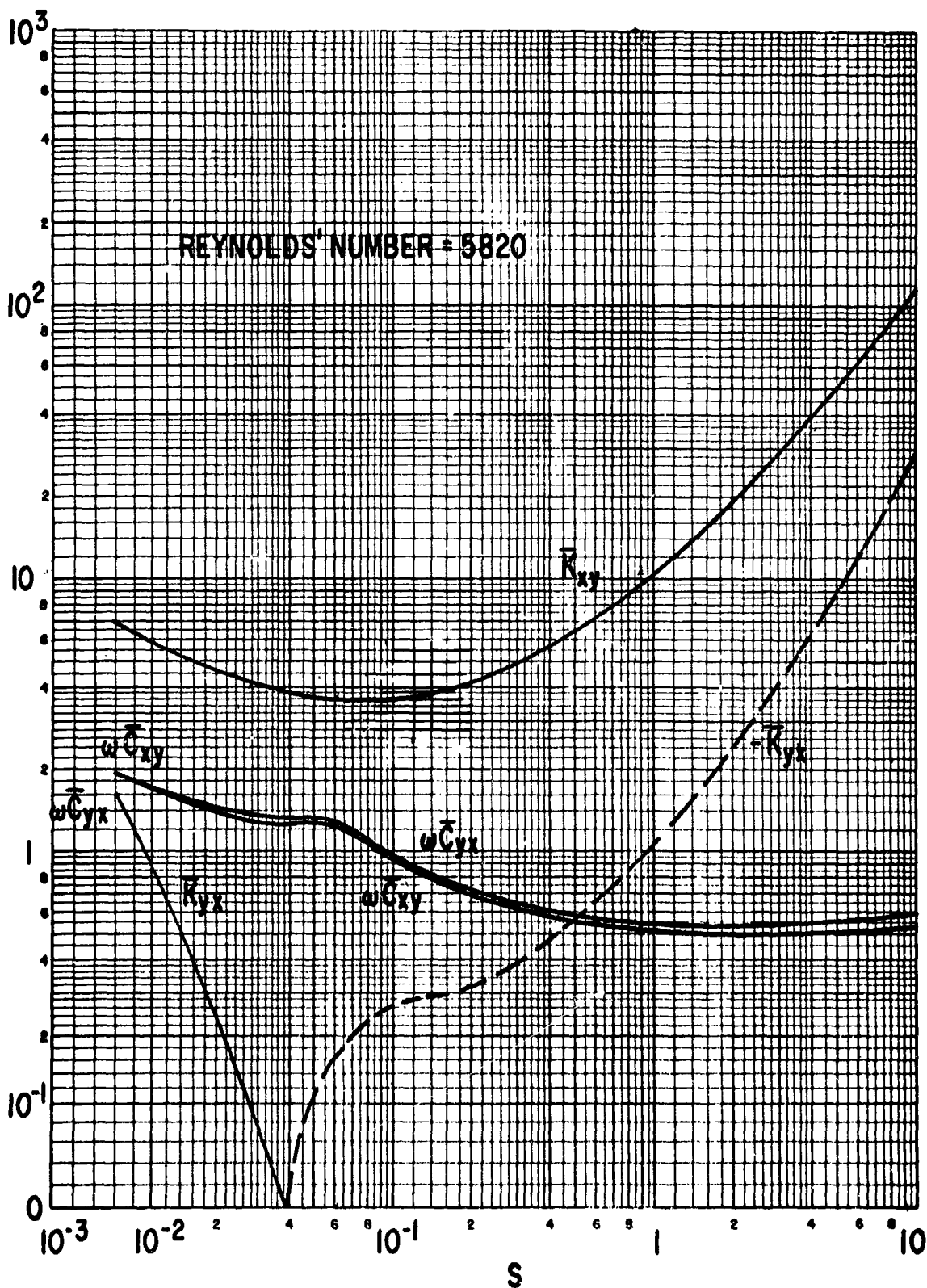


Fig. 28 Dimensionless Stiffness and Damping Coefficients for Centrally Loaded, 100° Arc Bearings ($L/D = 1$)

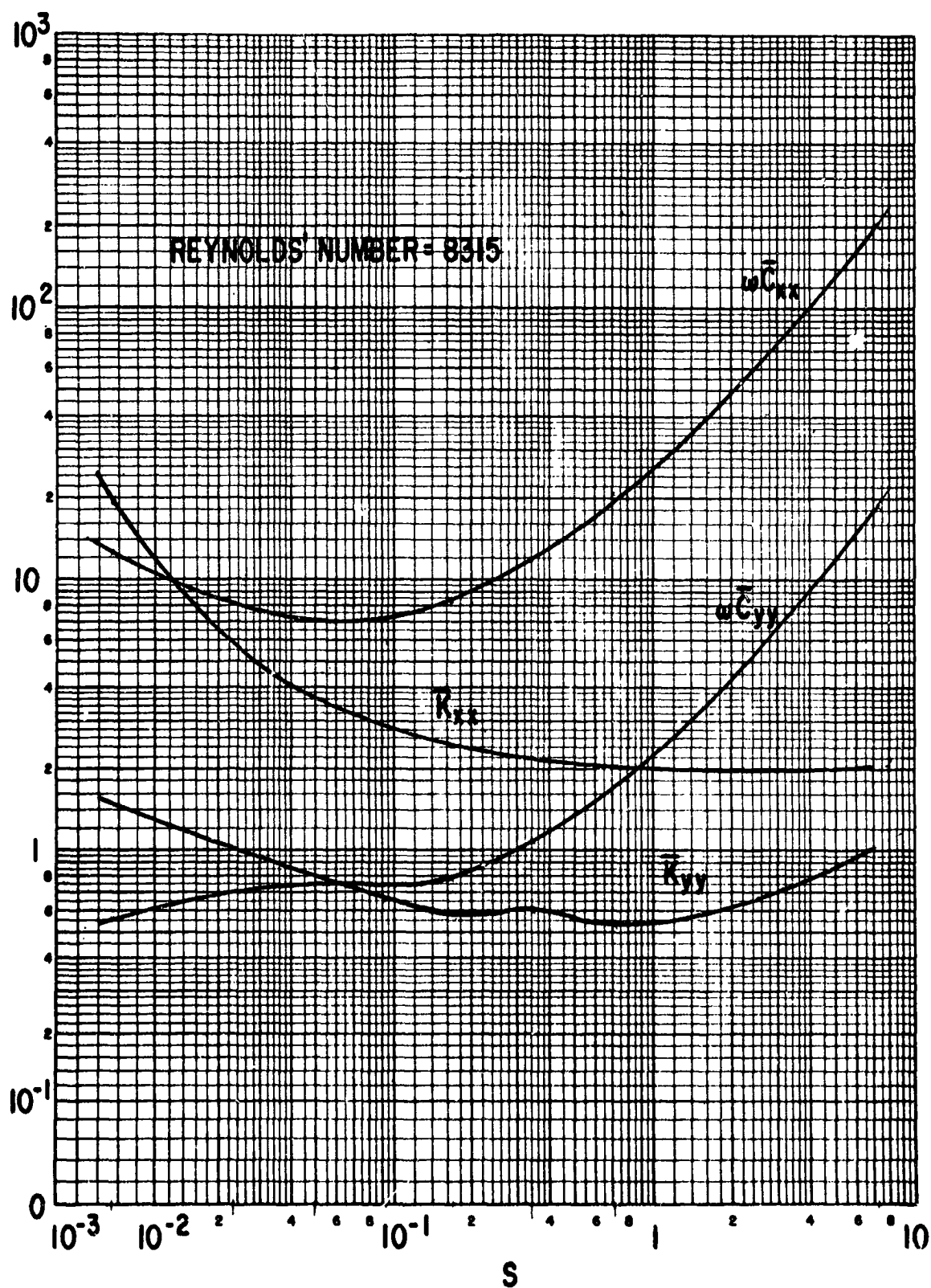


Fig. 29 Dimensionless Stiffness and Damping Coefficients for Centrally Loaded, 100° Arc Bearings ($L/D = 1$)

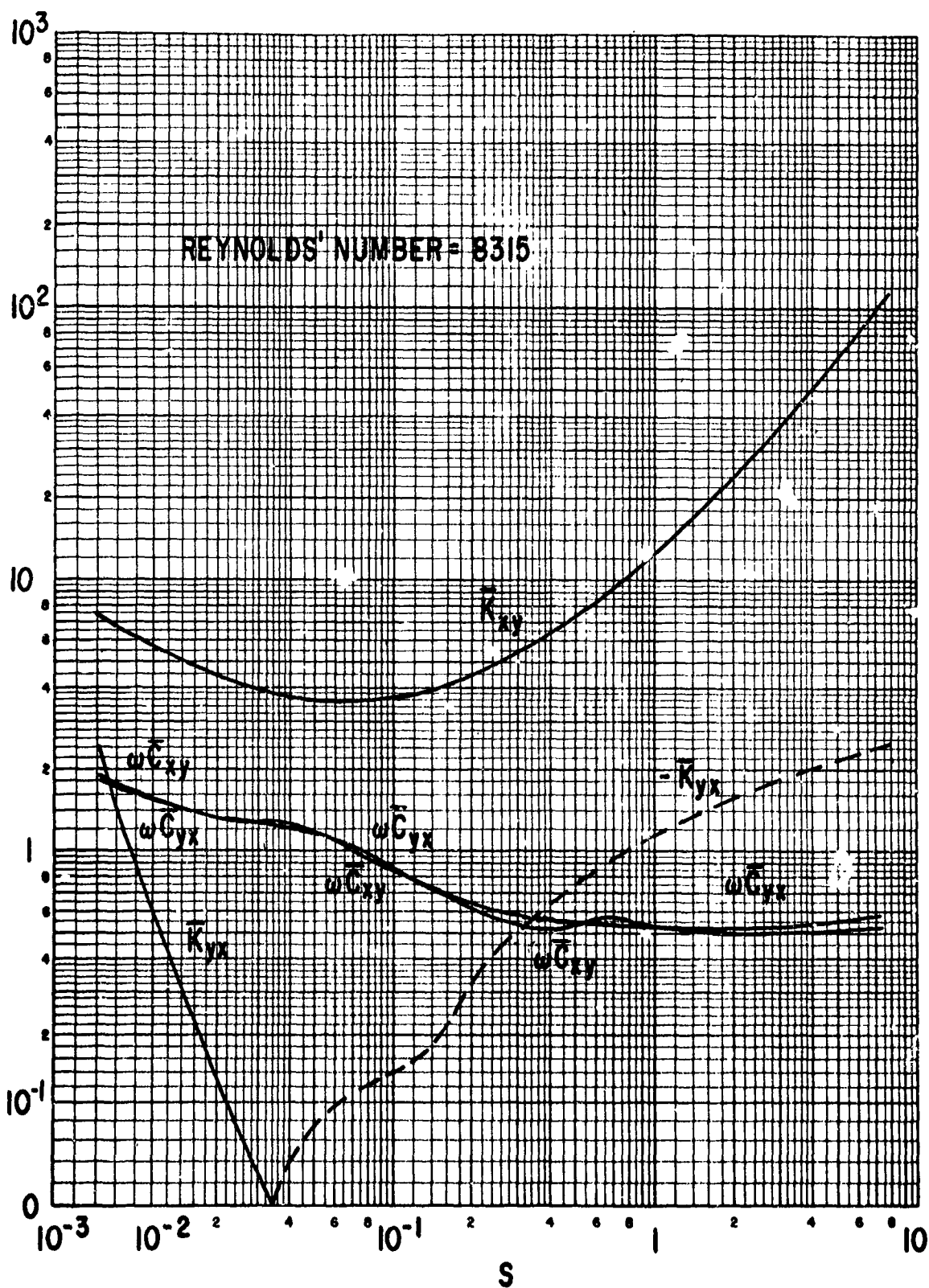


Fig. 30 Dimensionless Stiffness and Damping Coefficients
For Centrally Loaded, 100° Arc Bearings ($\eta/D = 1$)

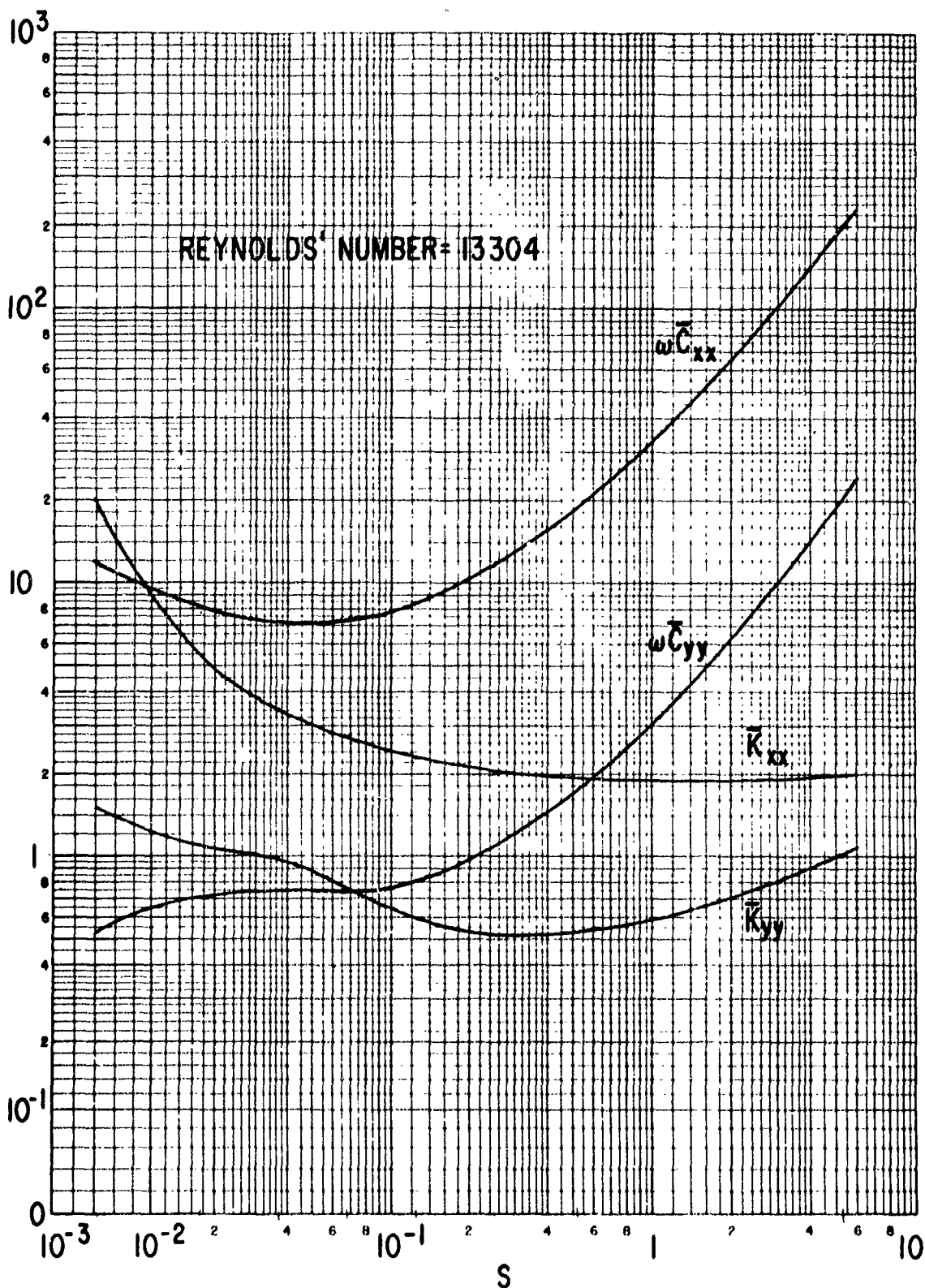


Fig. 31 Dimensionless Stiffness and Damping Coefficients for Centrally Loaded, 100° Arc Bearings ($U/D = 1$)

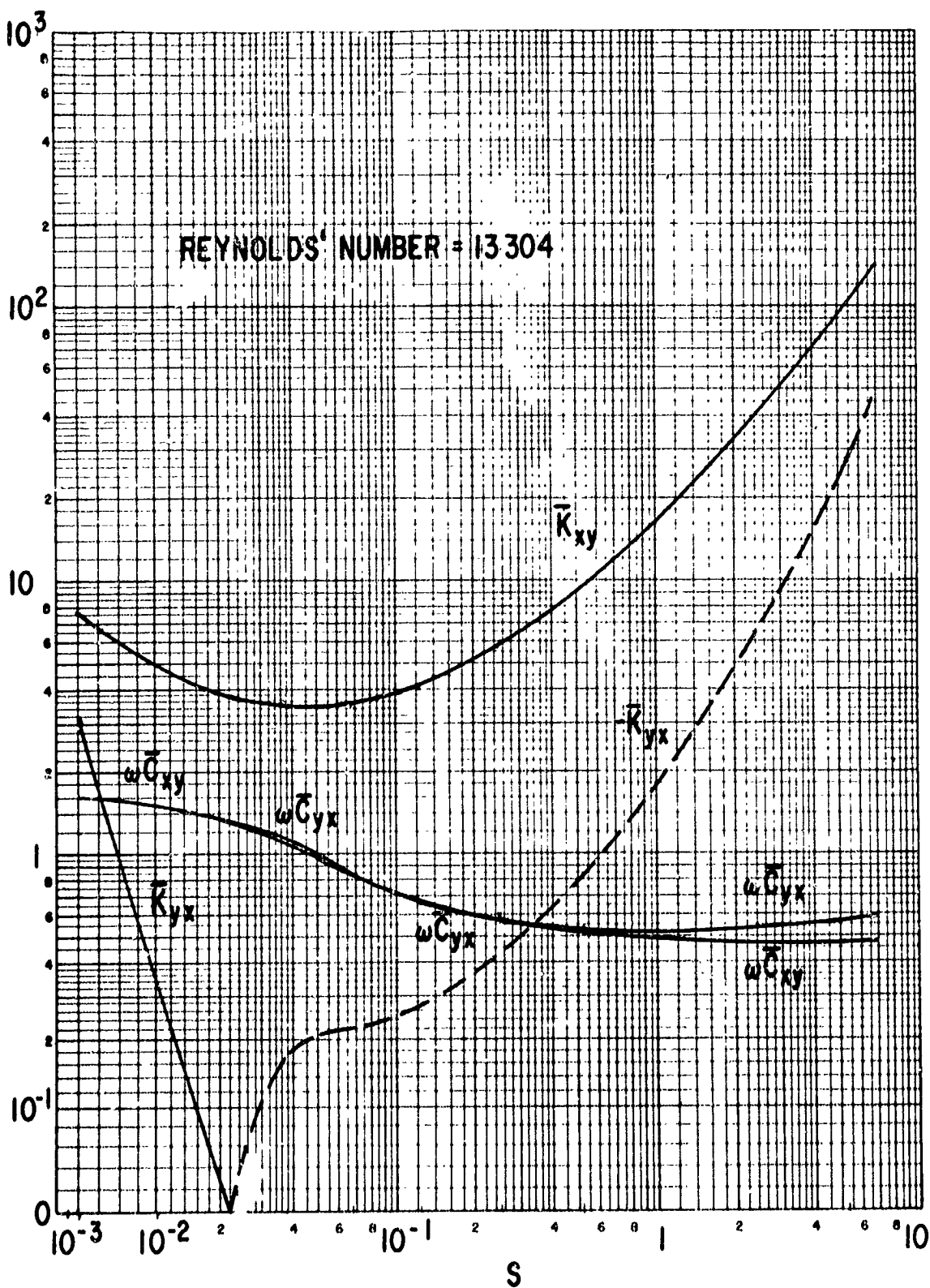


Fig. 32 Dimensionless Stiffness and Damping Coefficients for Centrally Loaded, 100° Arc Bearings ($L/D = 1$)

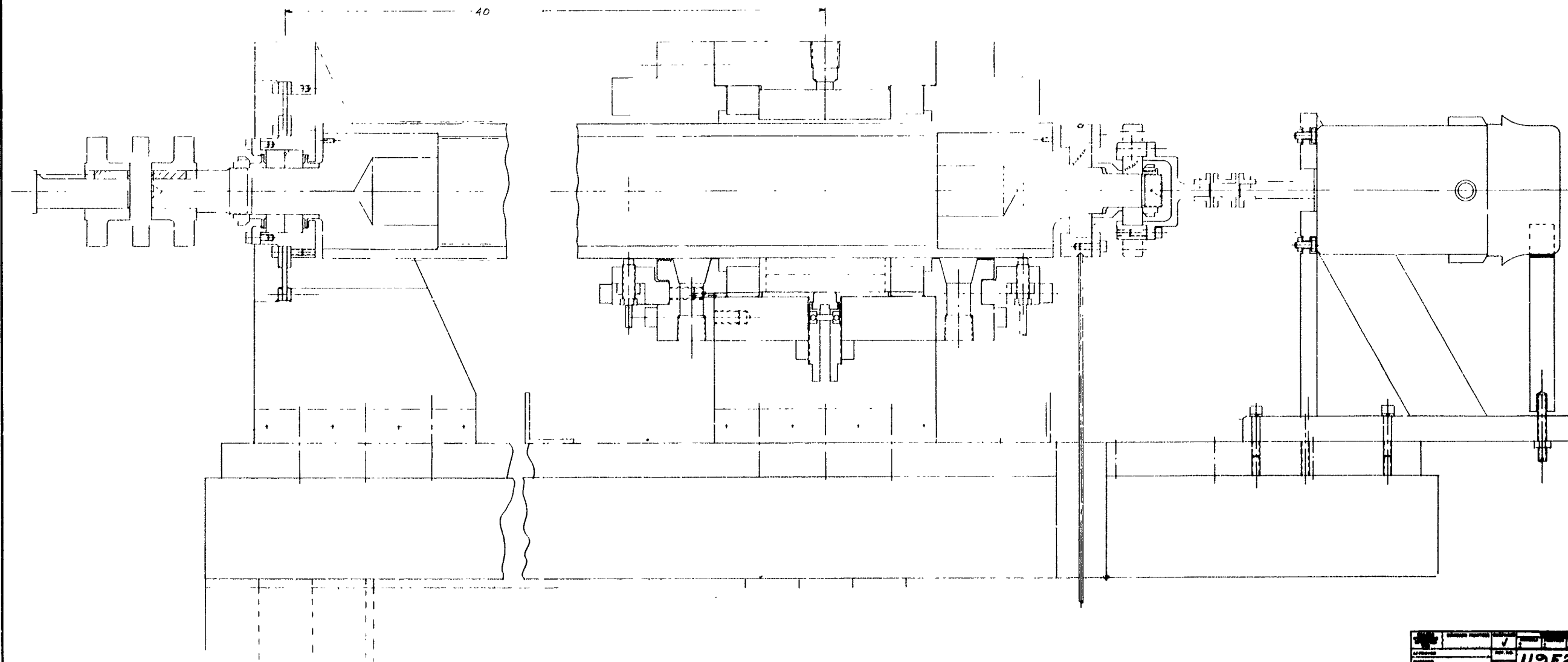


Fig. 33 Arrangement of Dynamic Load Bearing Apparatus Major Components

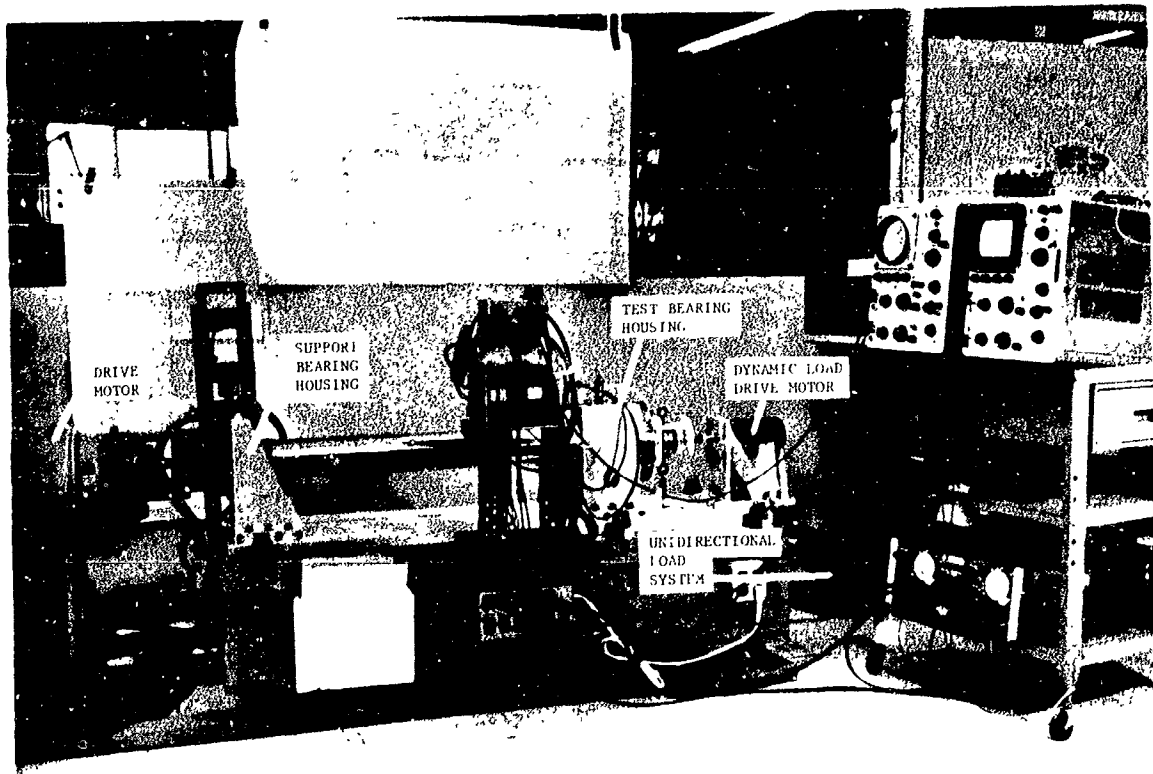


Fig. 34 Dynamic Load Bearing Apparatus

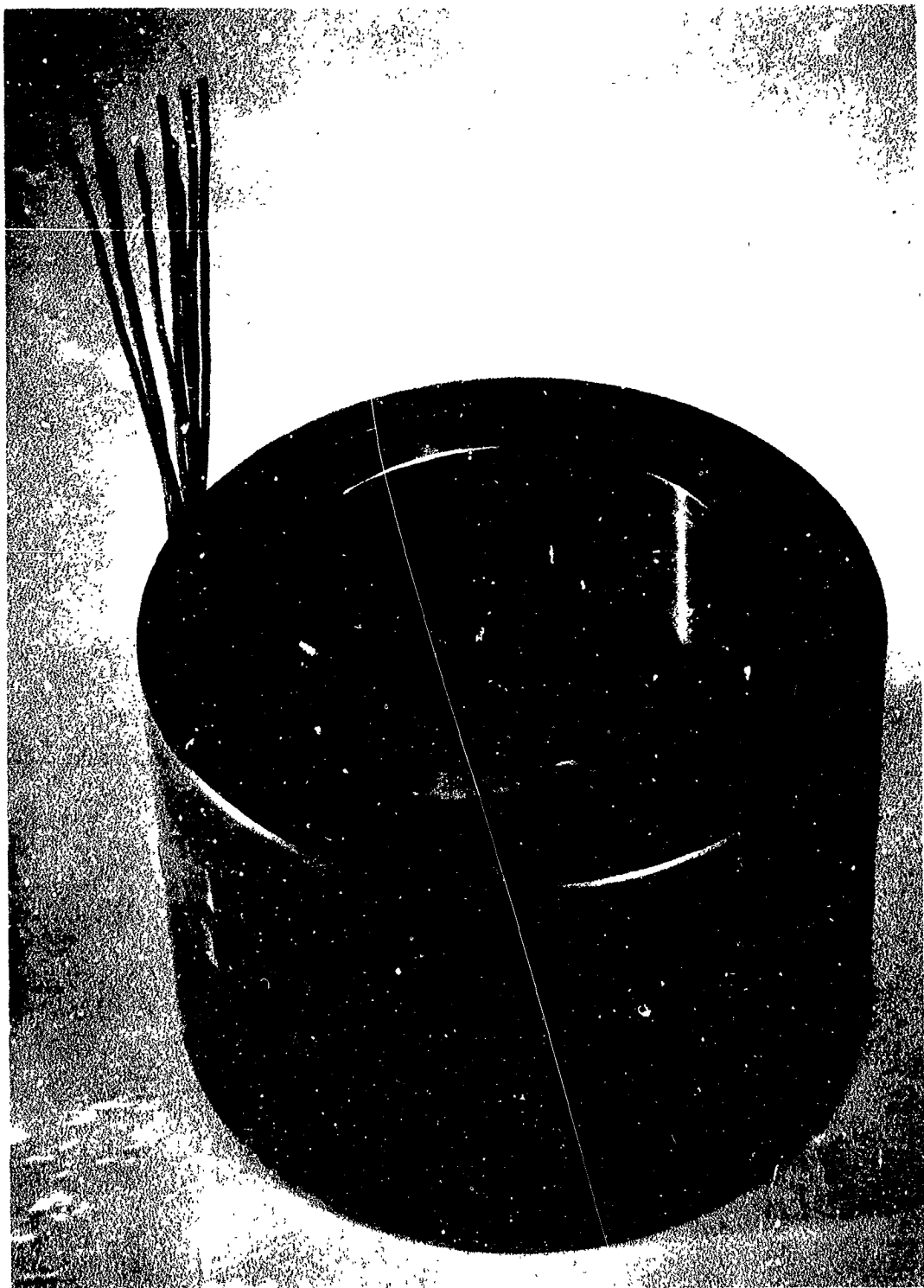


Fig. 35 Modified Partial Arc Bearing with Pressure Taps

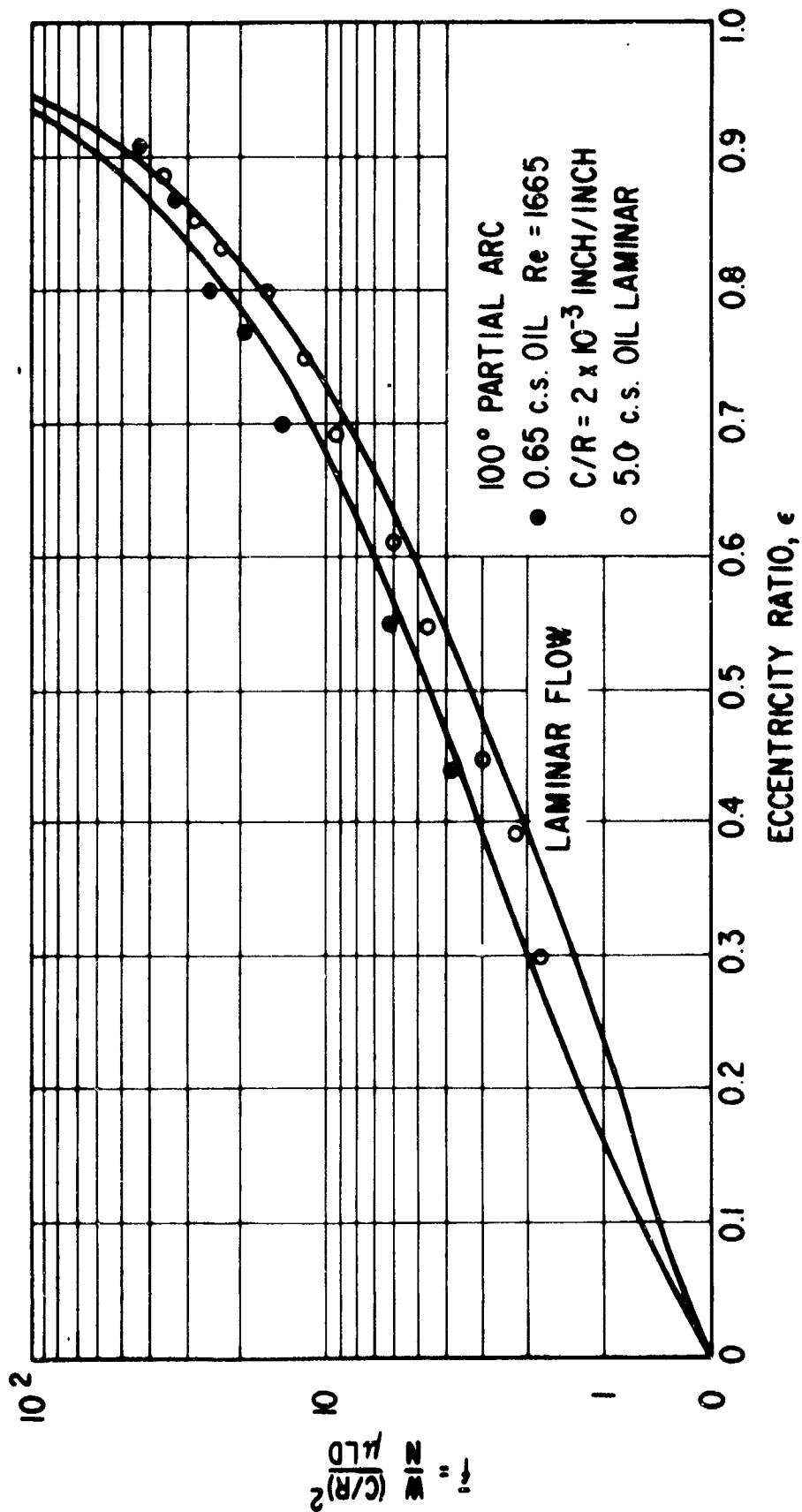


Fig. 36 Steady State Load Capacity - Reynolds Number 1665, $\beta = 100^\circ$

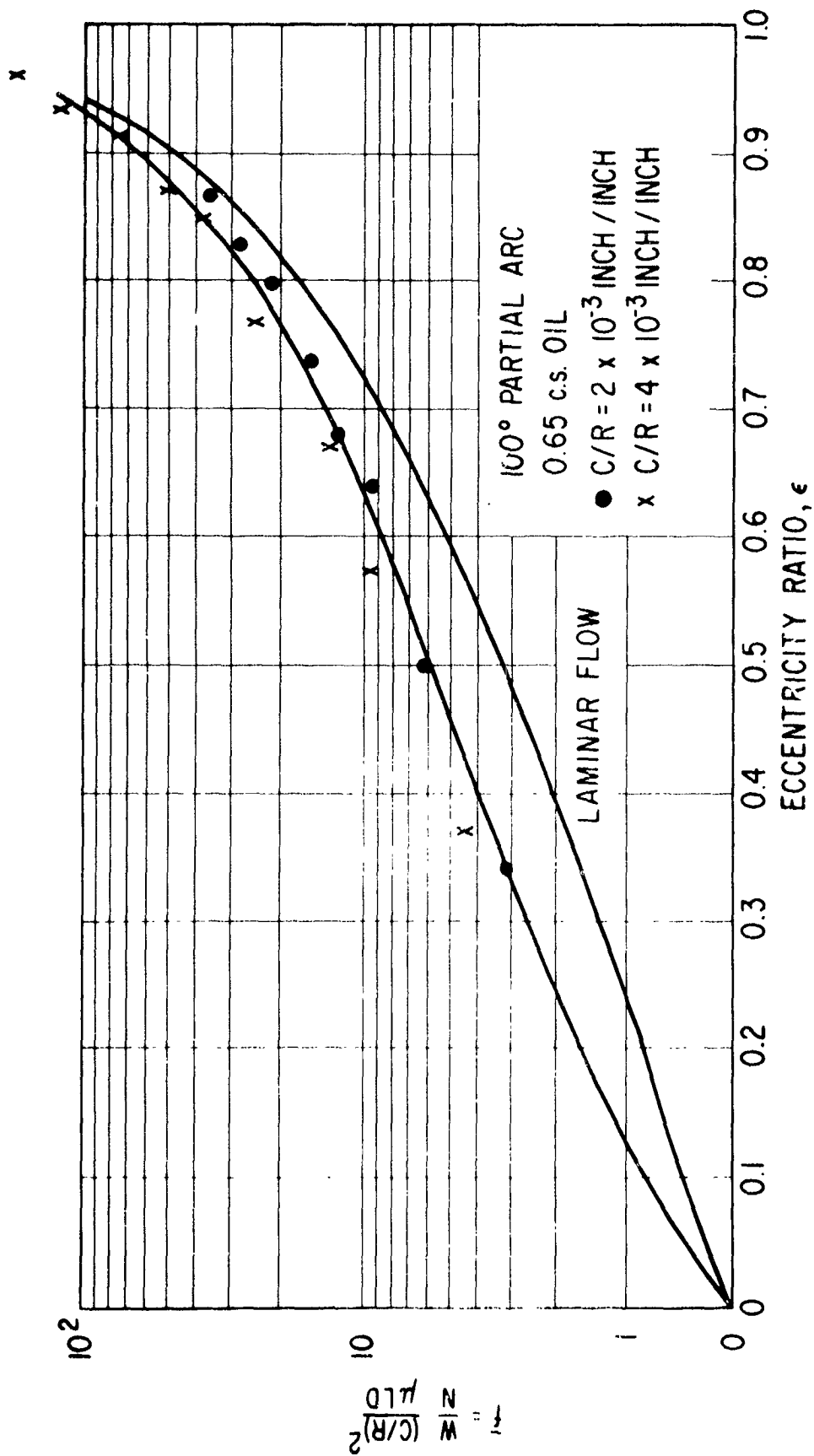


Fig. 37 Steady State Load Capacity - Reynolds Number 3326, $\epsilon = 100^\circ$

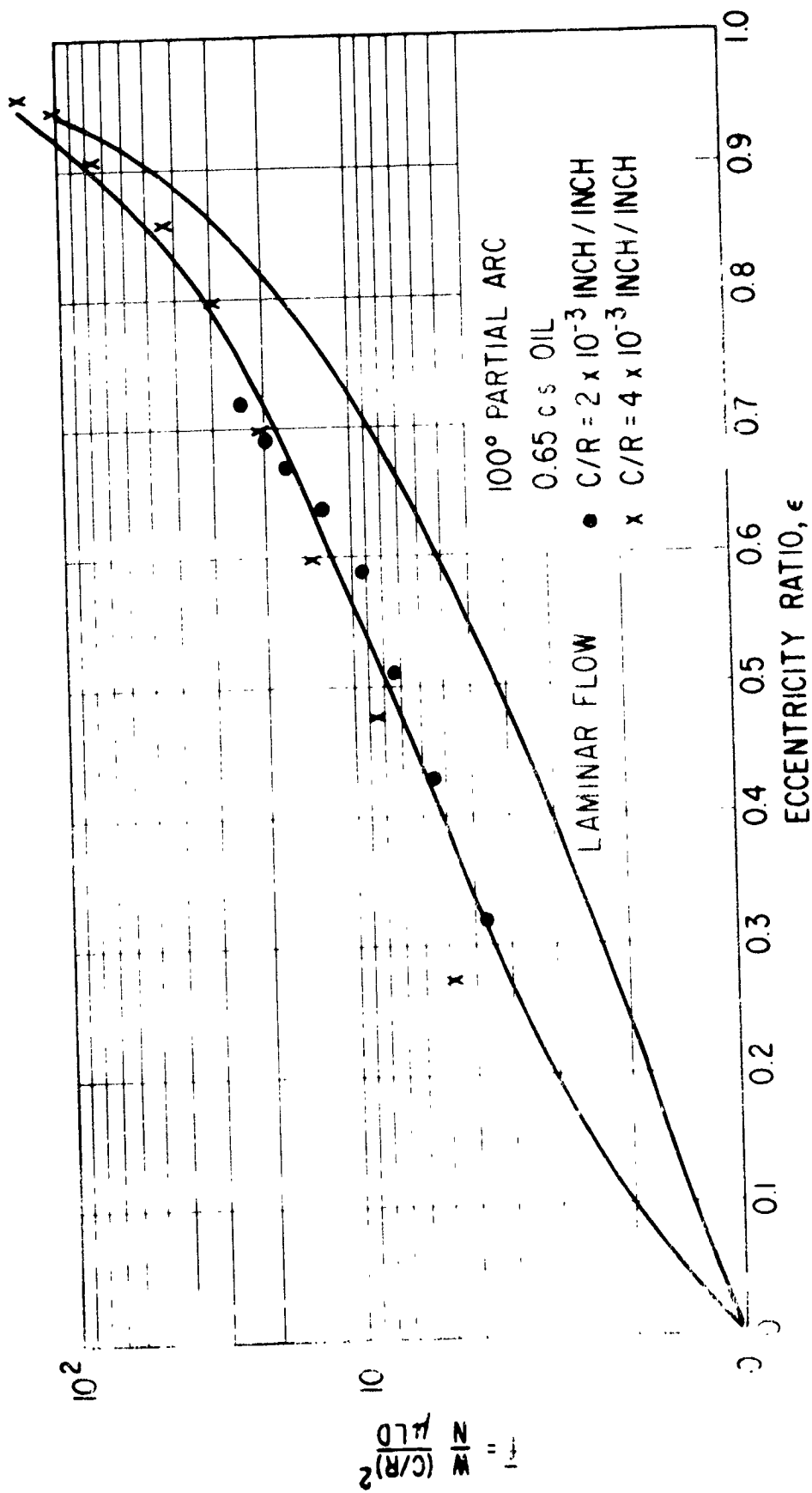


Fig. 3b Steady State Load Capacity - Reynolds Number 5820, $\mu = 100^c$

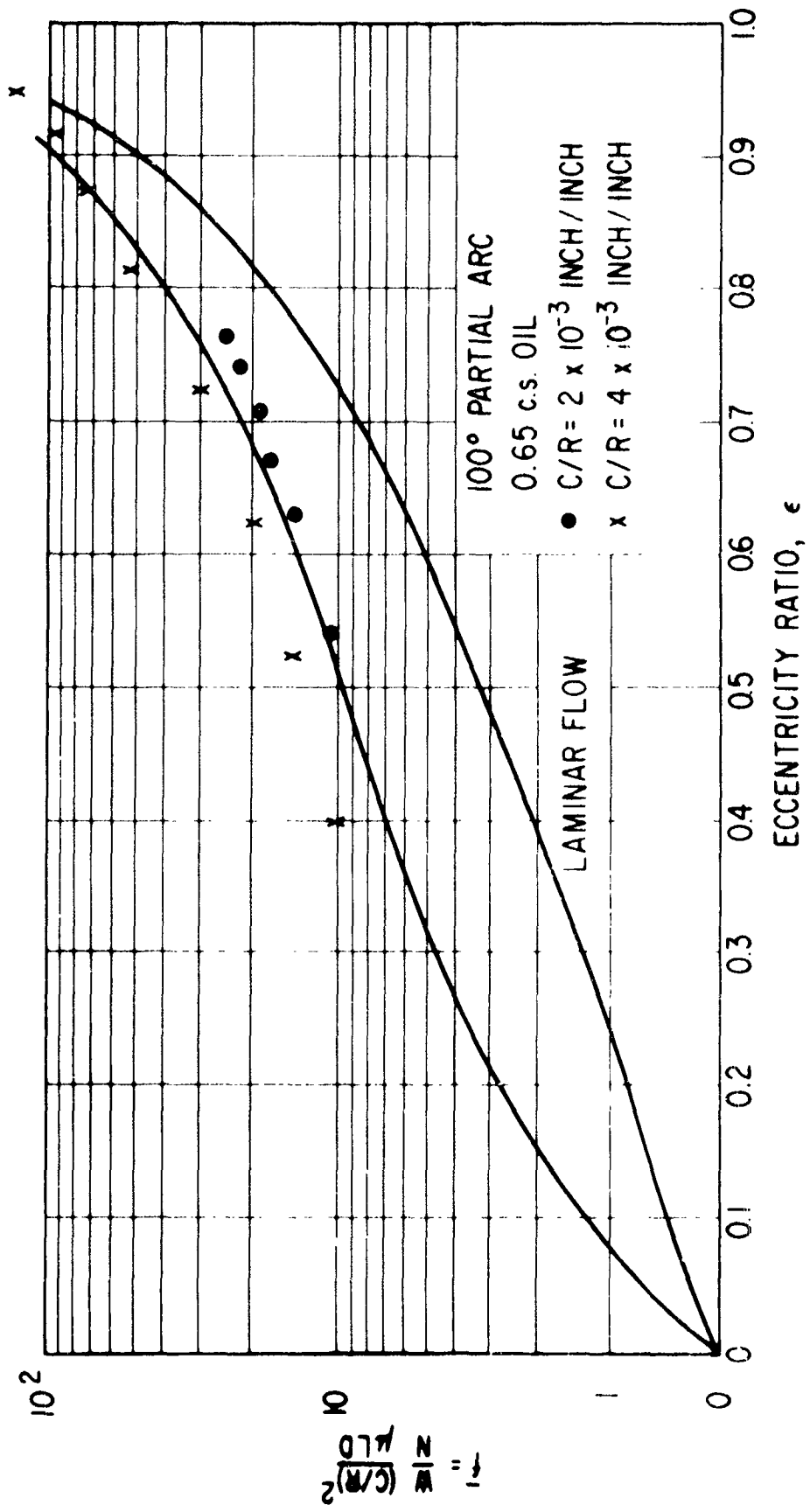


Fig. 59 Steady State Load Capacity - Reynolds Number 8314, $\theta = 100^\circ$

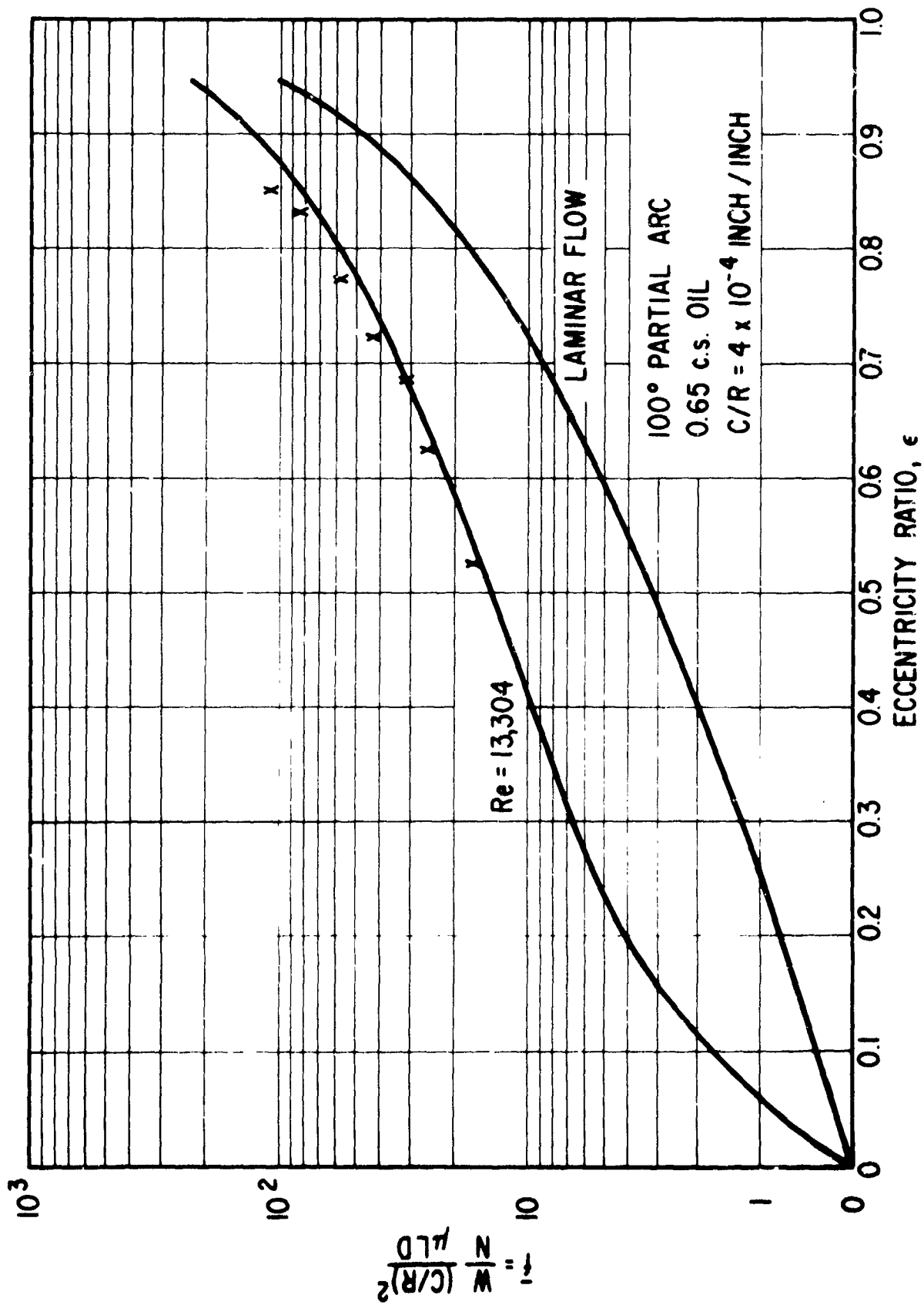


Fig. 40 Steady State Load Capacity - Reynolds Number 13,304, $\theta = 100^\circ$

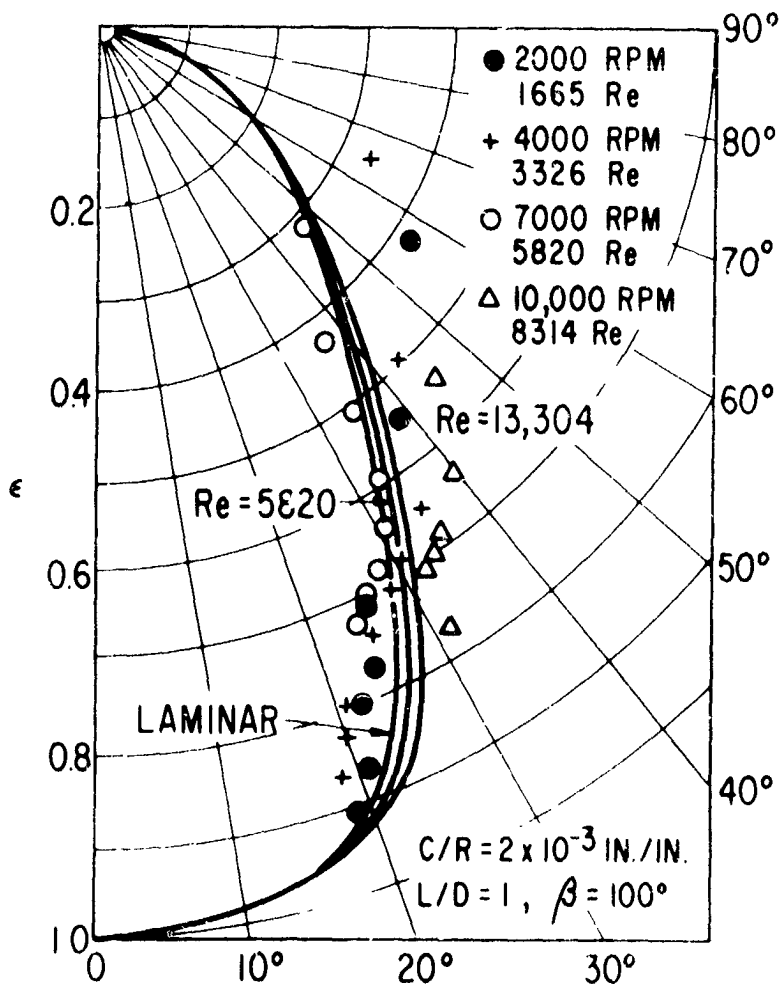


Fig. 41 Eccentricity - Attitude Angle Measurements
 $C/R = 2 \times 10^{-3}$ in/in., $\beta = 100^\circ$

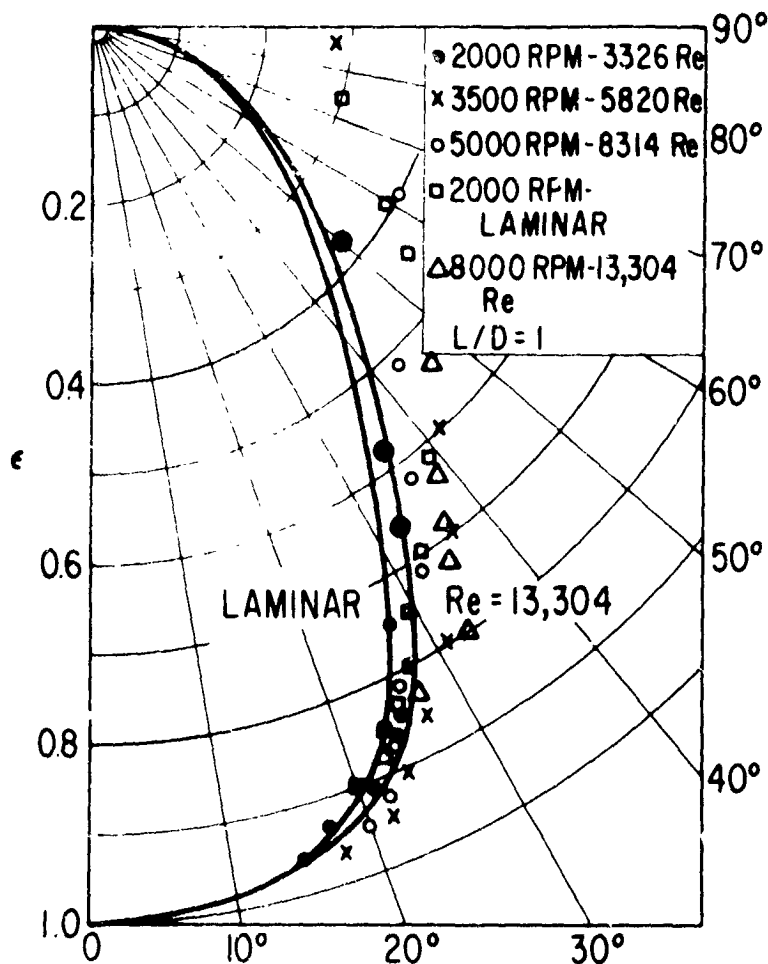


FIG. 42 Eccentric Attitude Angle Measurements
 $C/R = 4 \times 10^{-3}$ in/in., $\mu = 100^\circ$

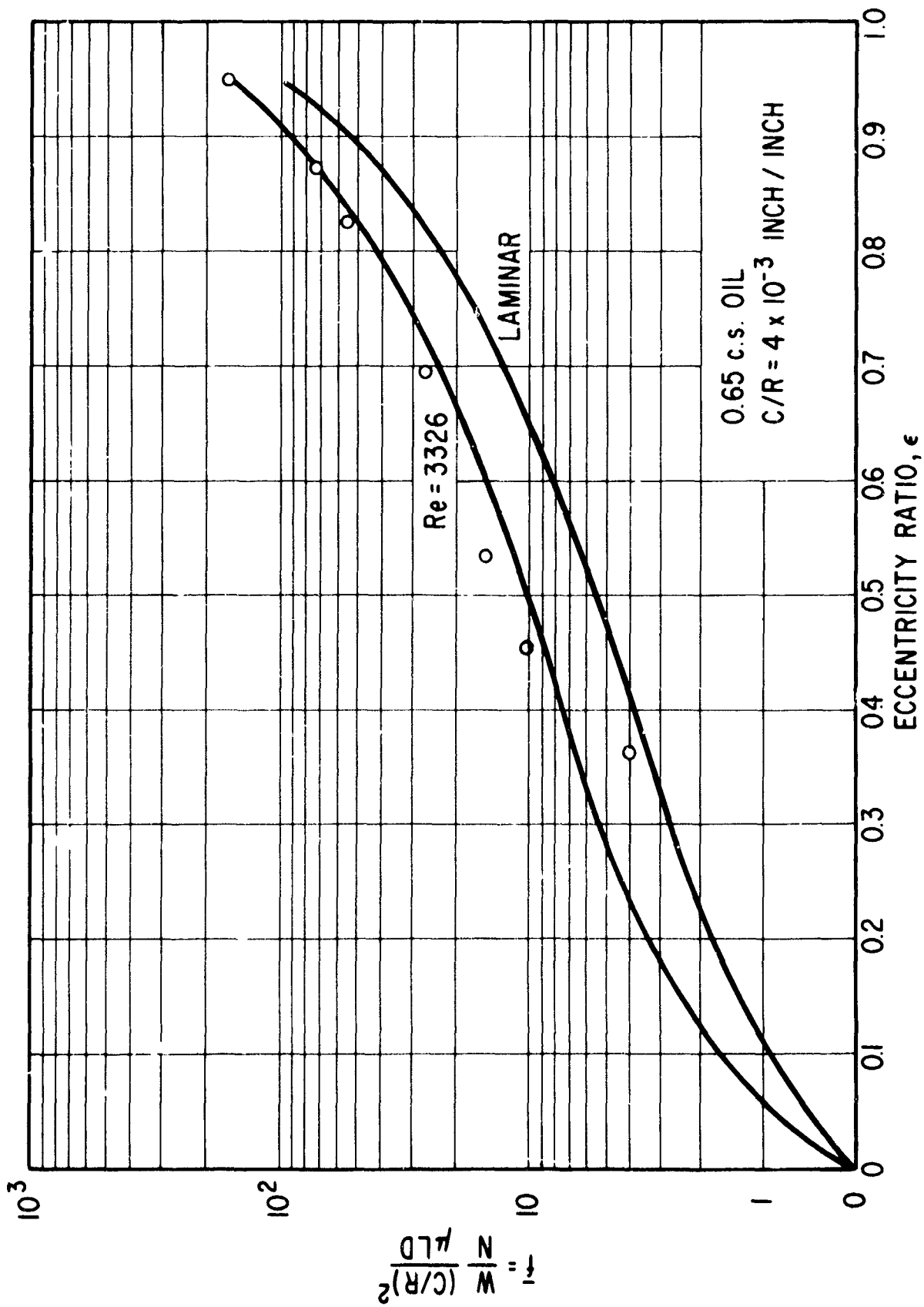


Fig. 43 Steady State Load Capacity - Reynolds Number 3326, $\mu = 350$

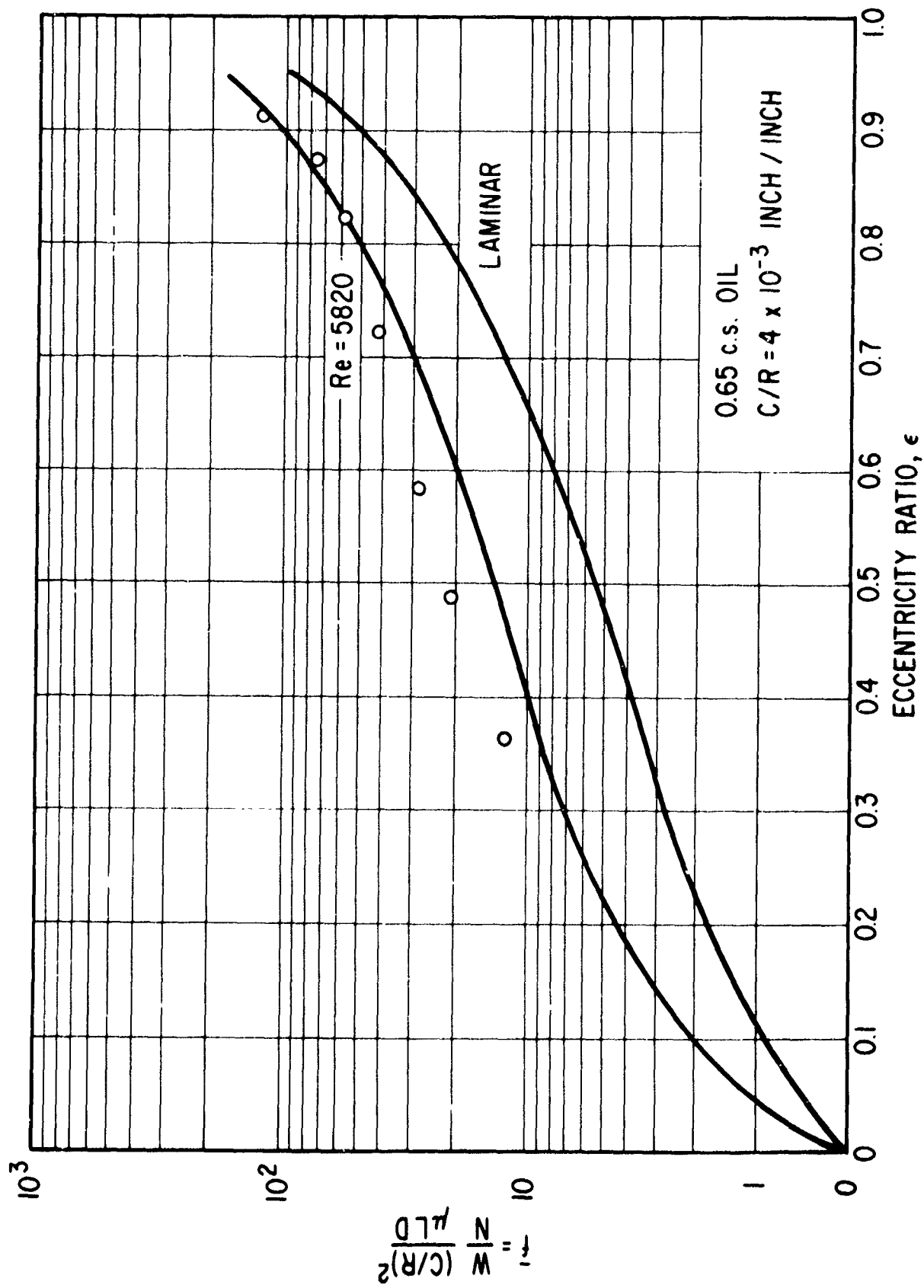


Fig 44 Steady State Load Capacity - Reynolds Number 5820, $\mu = 350^c$

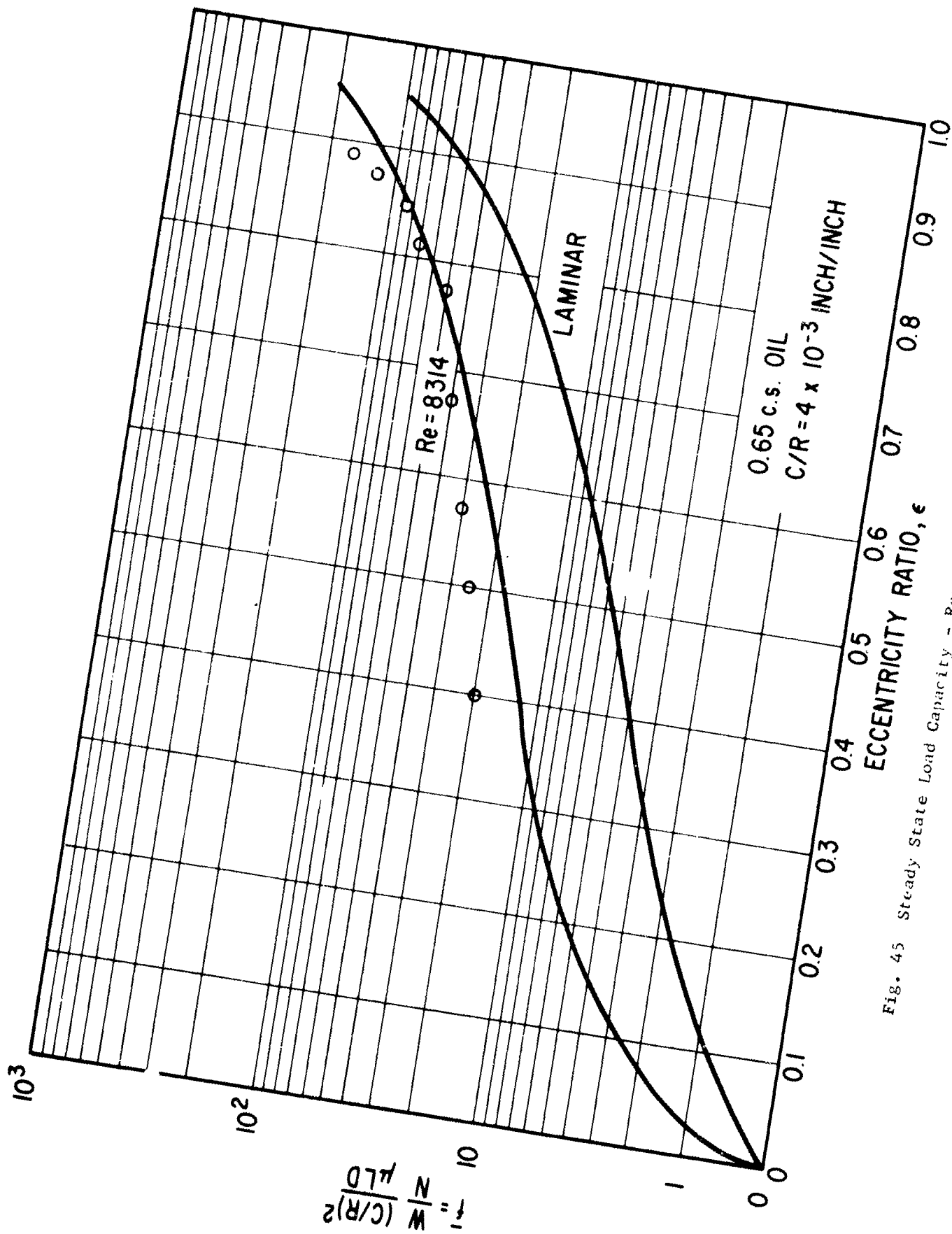


Fig. 45 Steady State Load Capacity - Reynolds Number 8314, $\mu = 3 \times 10^{-3}$

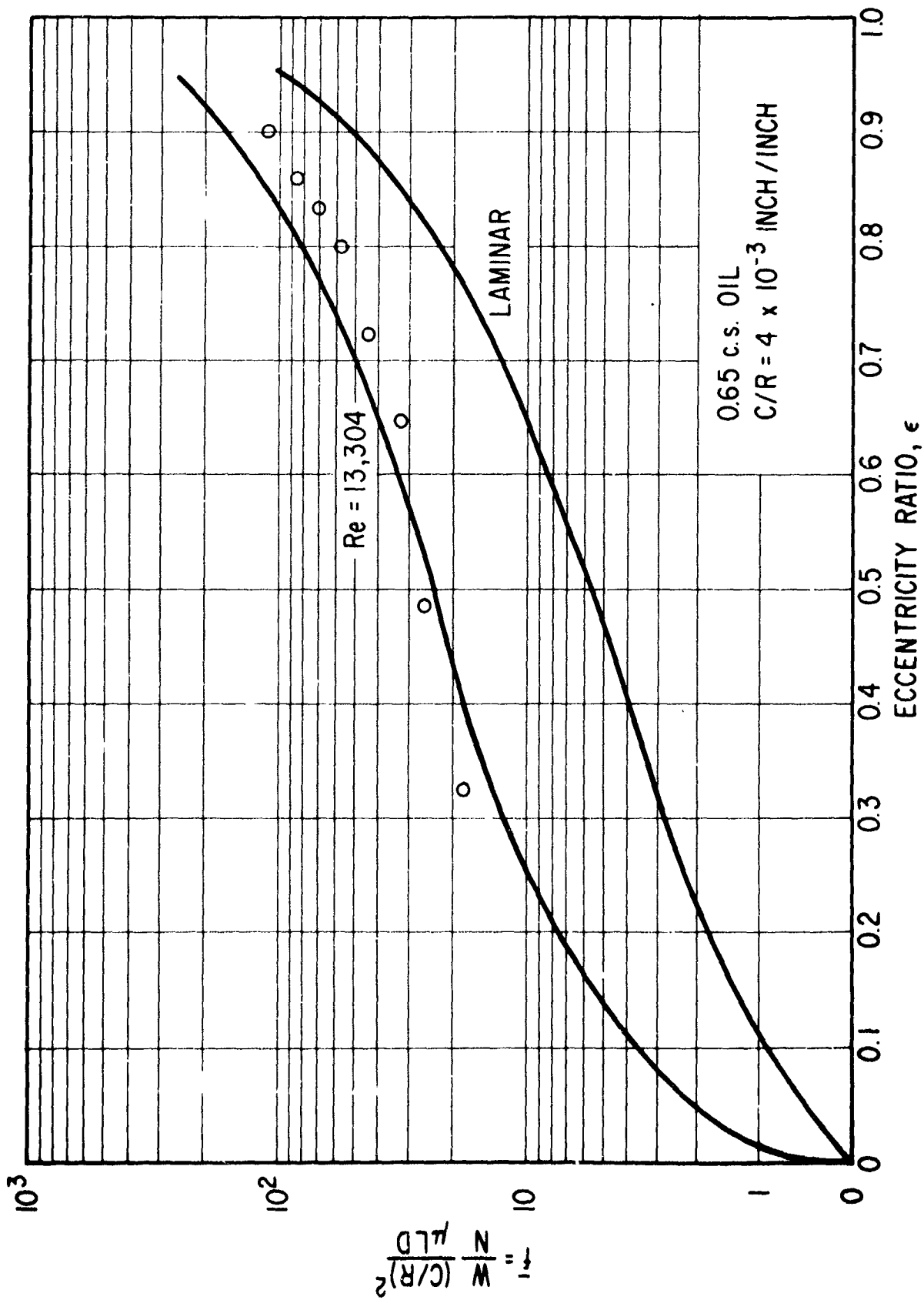


Fig. 46 Steady State Load Capacity - Reynolds Number 13,304, $\mu = 360^0$

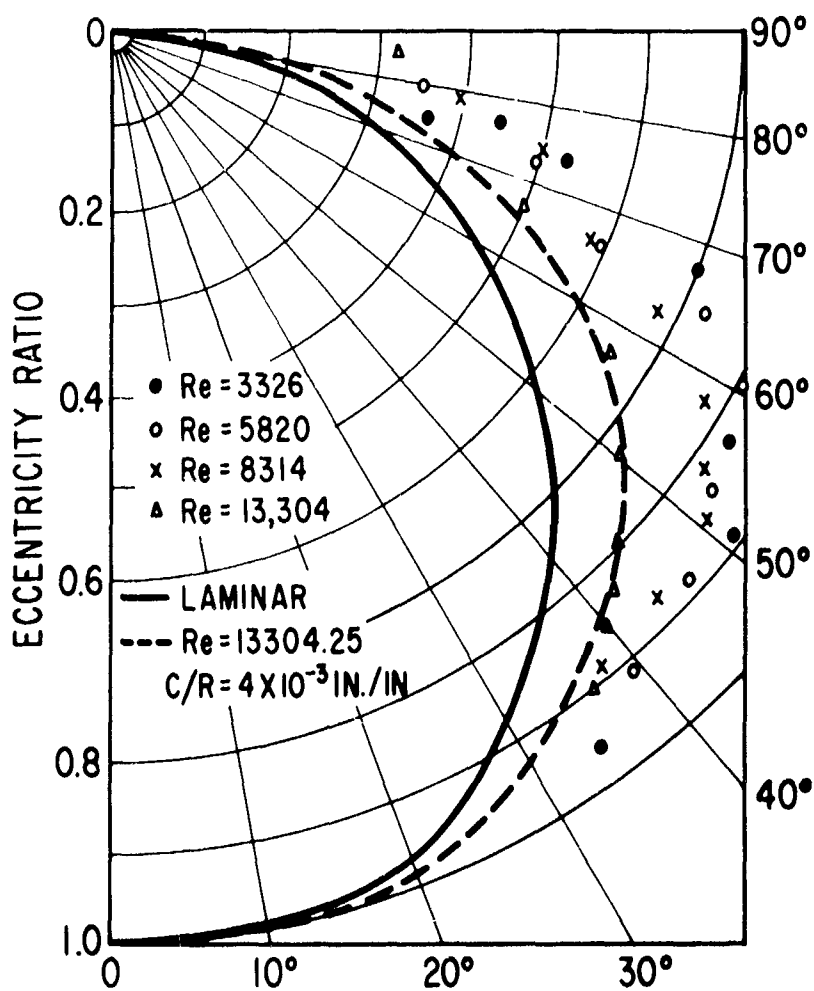


Fig. 47 Eccentricity - Attitude Angle Measurements - $\beta = 360^\circ$

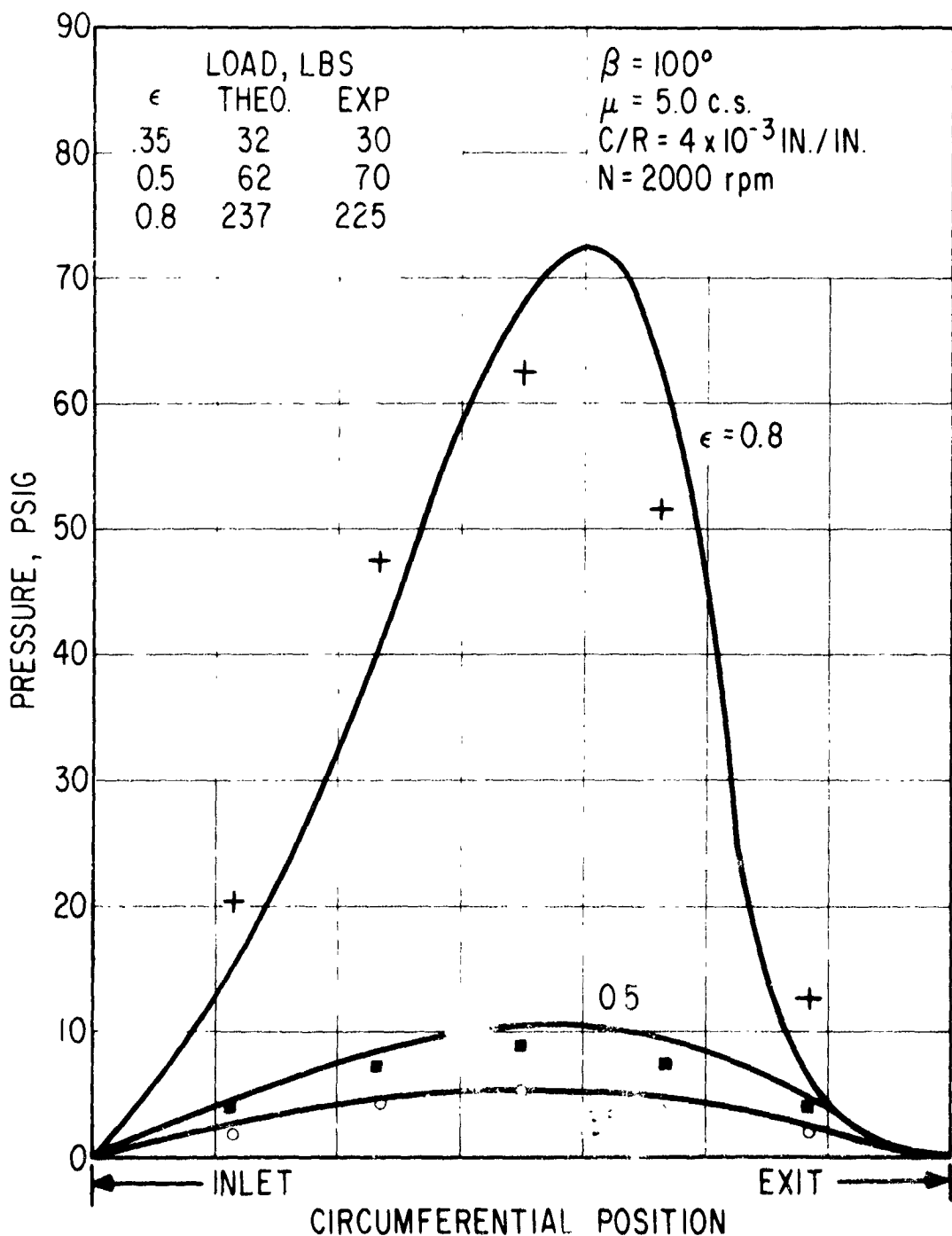


Fig. 48 Laminar Flow Pressure Distribution in Circumferential Direction

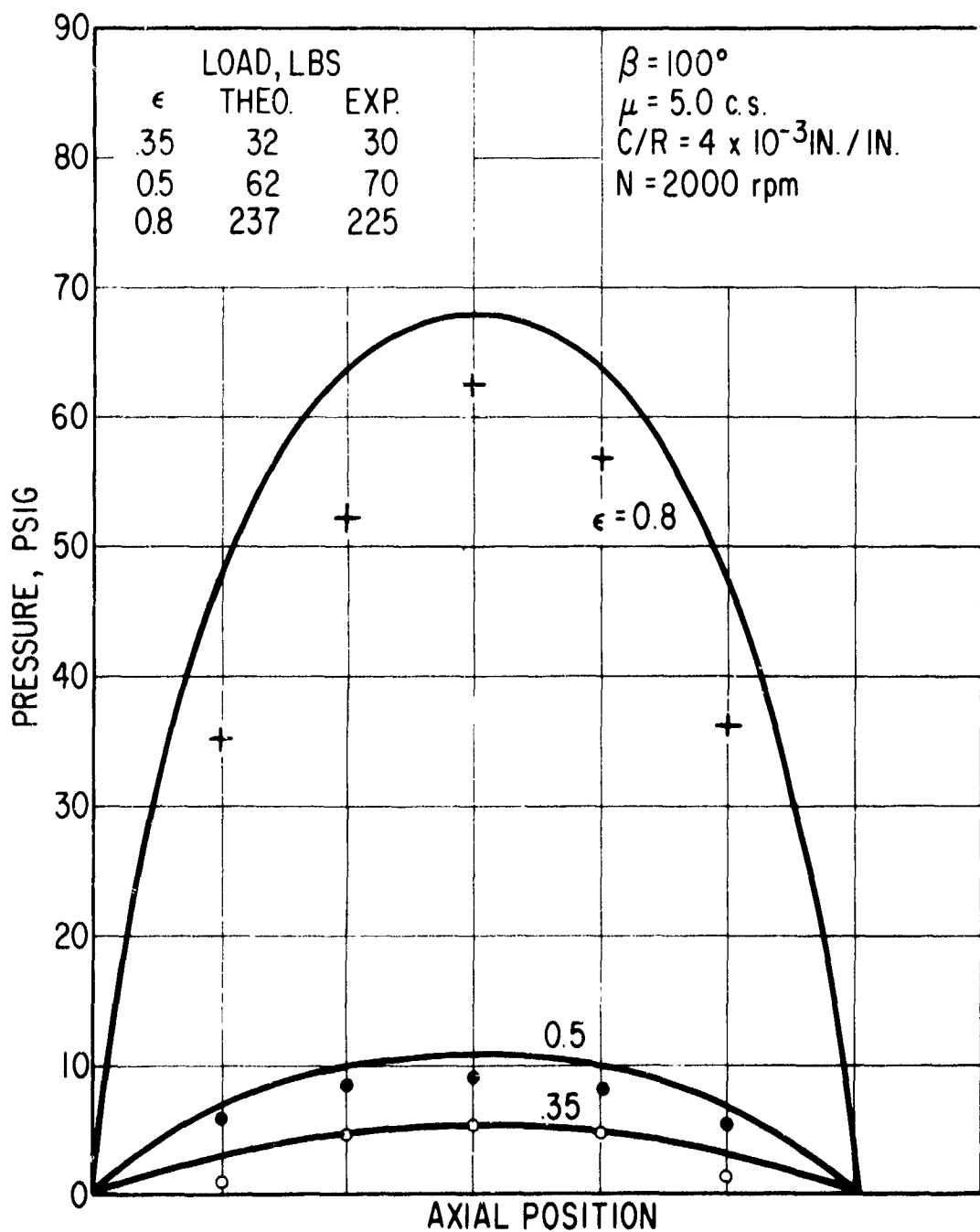


Fig. 49 Laminar Flow Pressure Distribution in Axial Direction

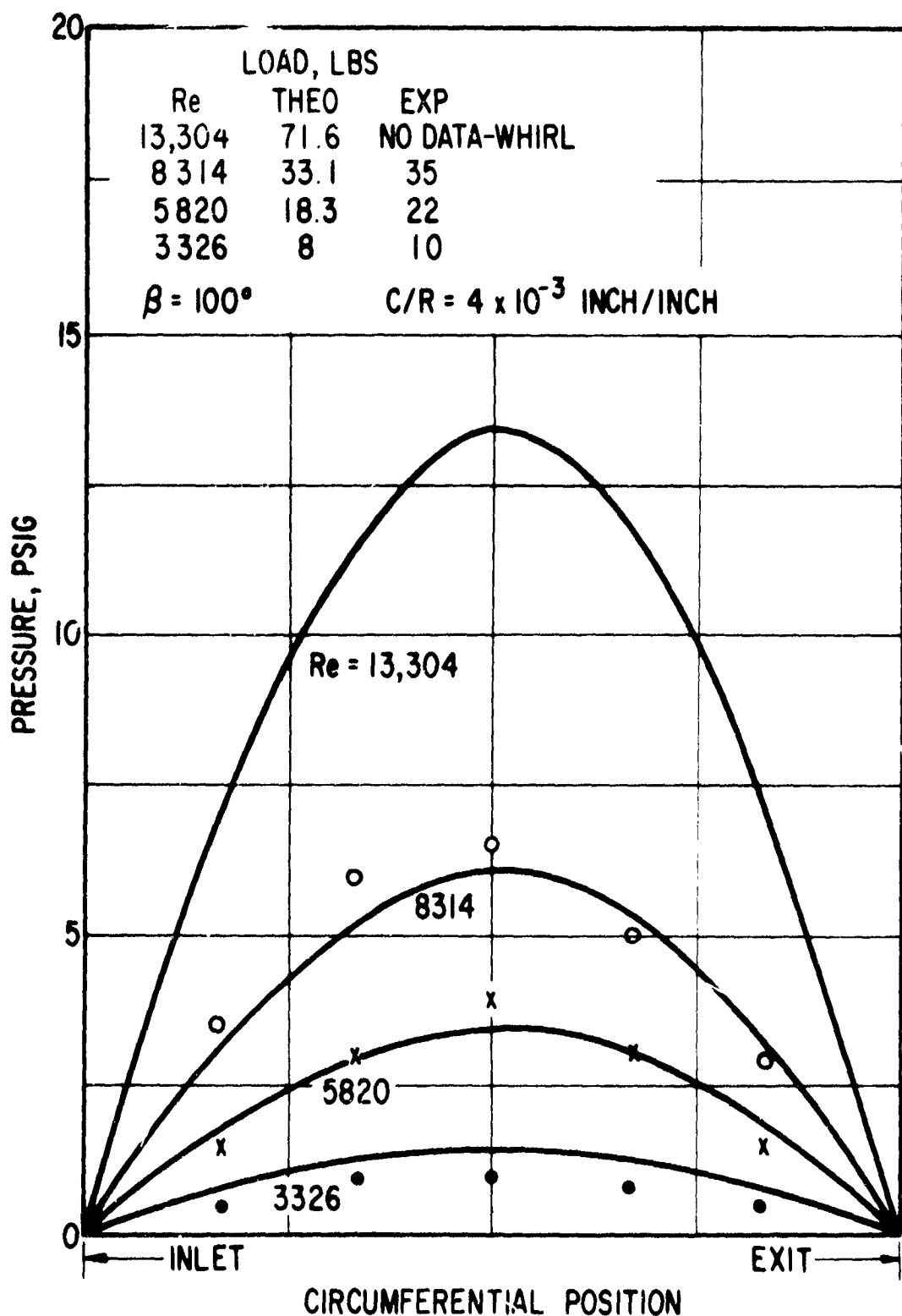


Fig. 50 Measured and Calculated Film Pressure in the Circumferential Direction
 $\epsilon = .35$

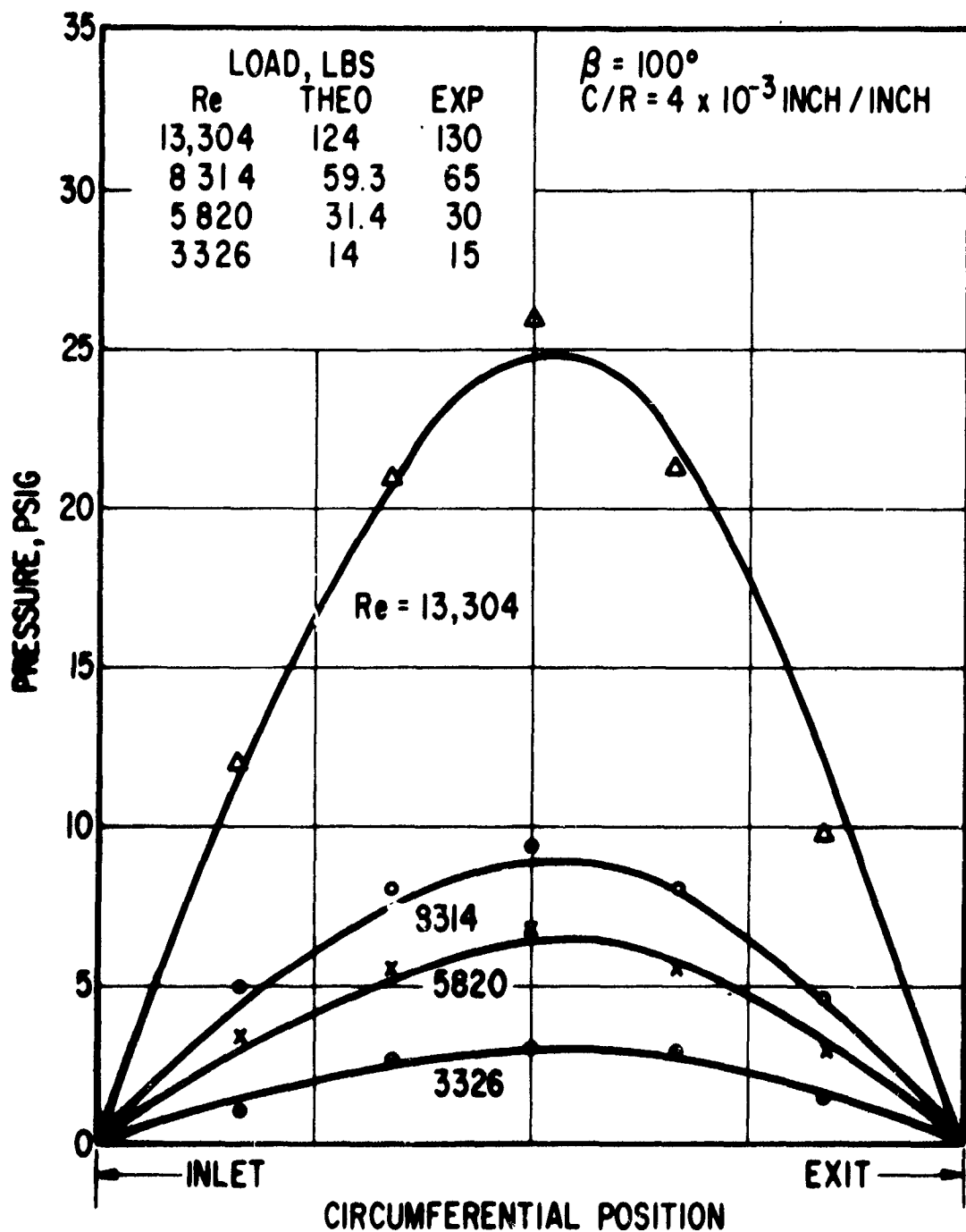


Fig. 51 Measured and Calculated Film Pressure in the Circumferential Direction - $\epsilon = .5$

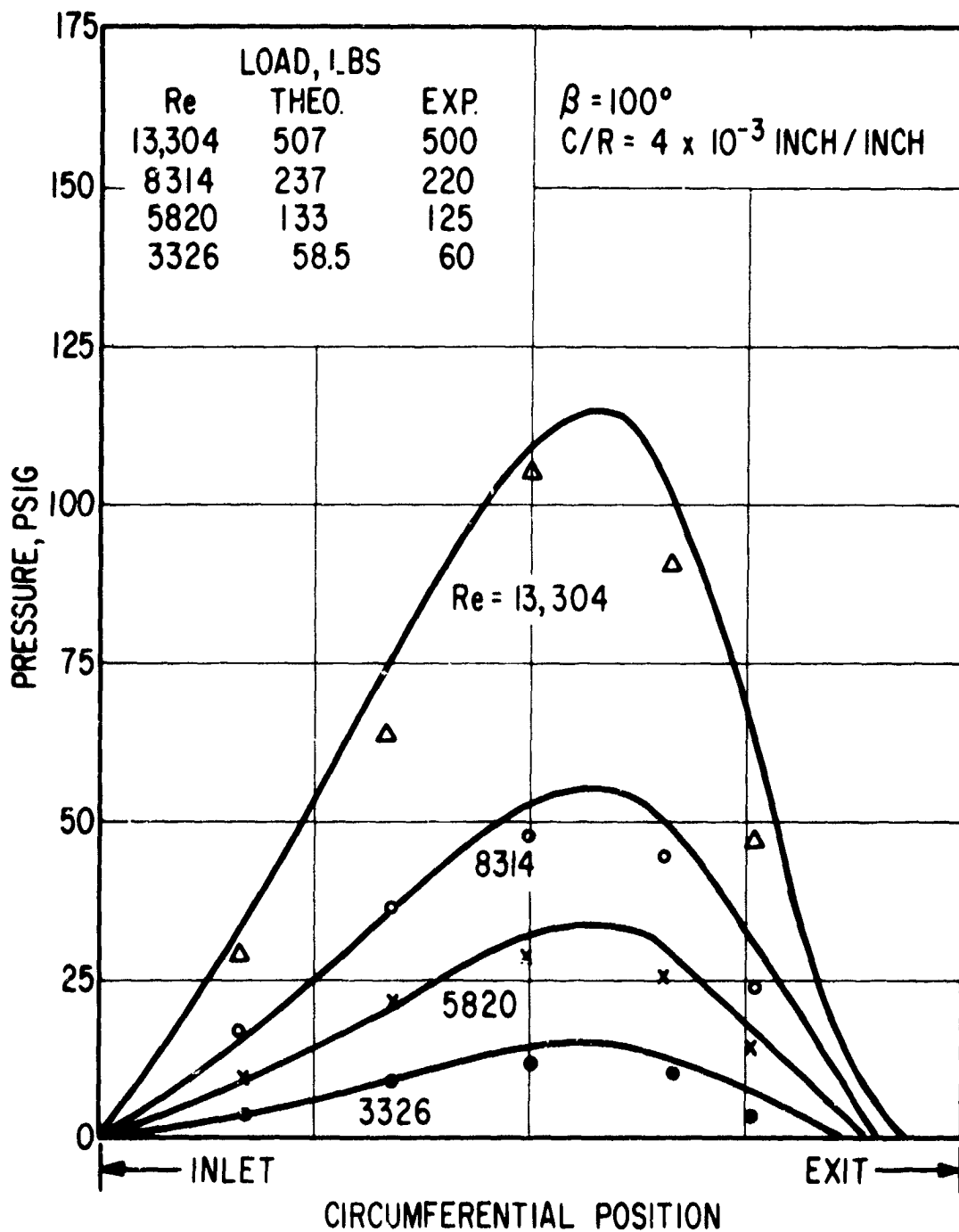


Fig. 52 Measured and Calculated Film Pressure in the Circumferential Direction - $c = .8$

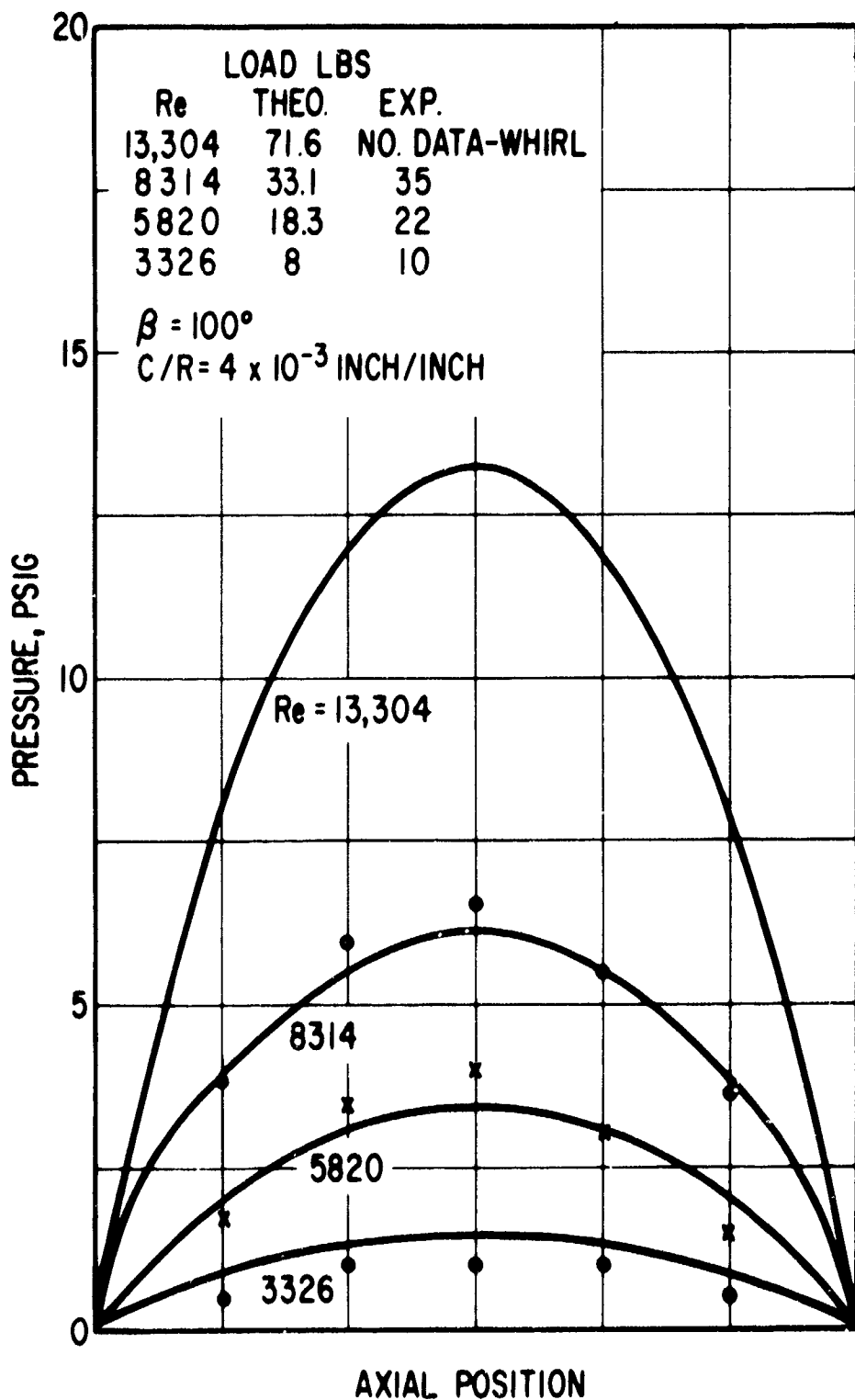


Fig. 53 Measured and Calculated Film Pressure in the Axial Direction - $\epsilon = .35$

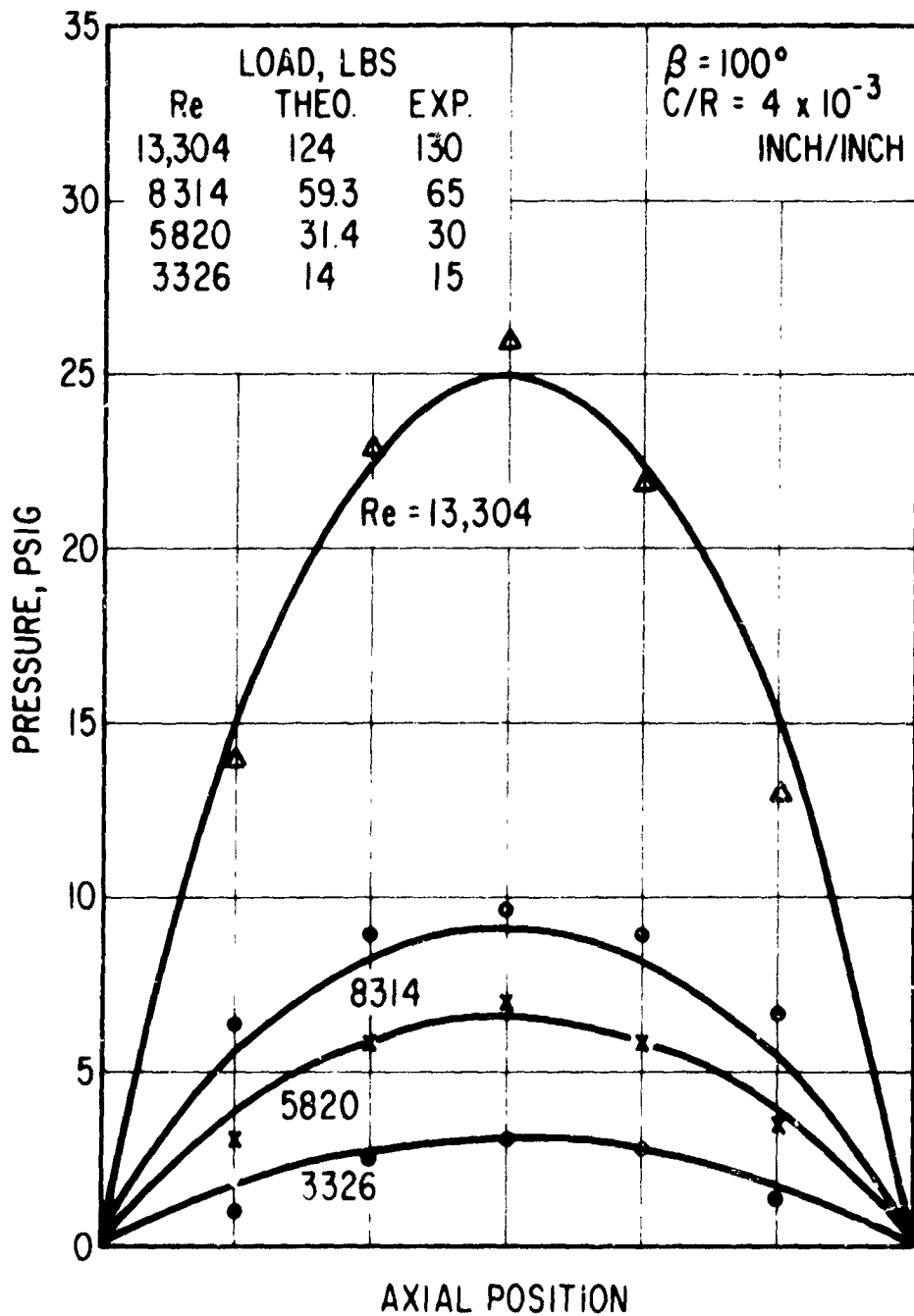


Fig. 54 Measured and Calculated Film Pressure in the Axial Direction - = .5

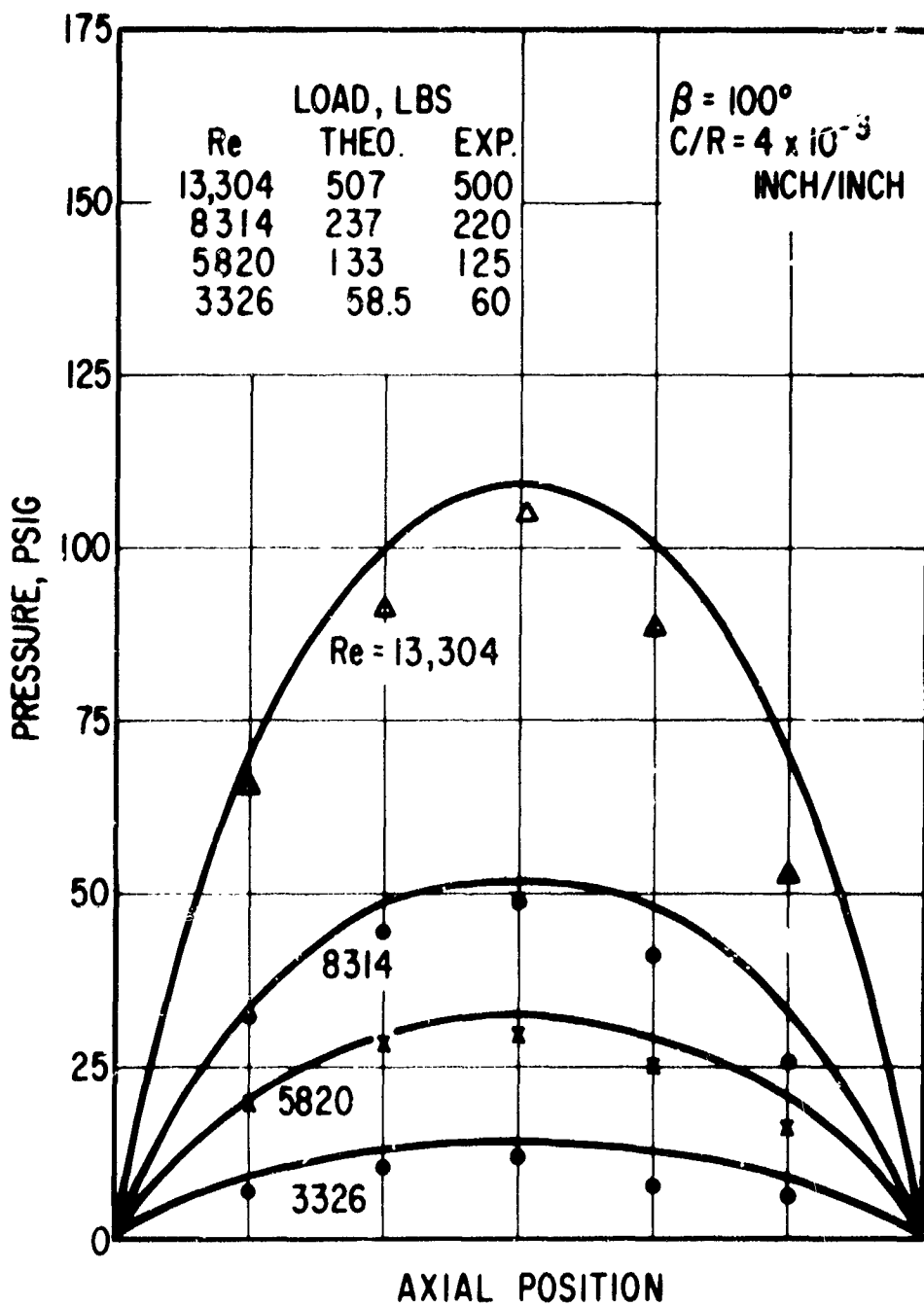


Fig. 55 Measured and Calculated Film Pressure in the Axial Direction - $\epsilon = .8$

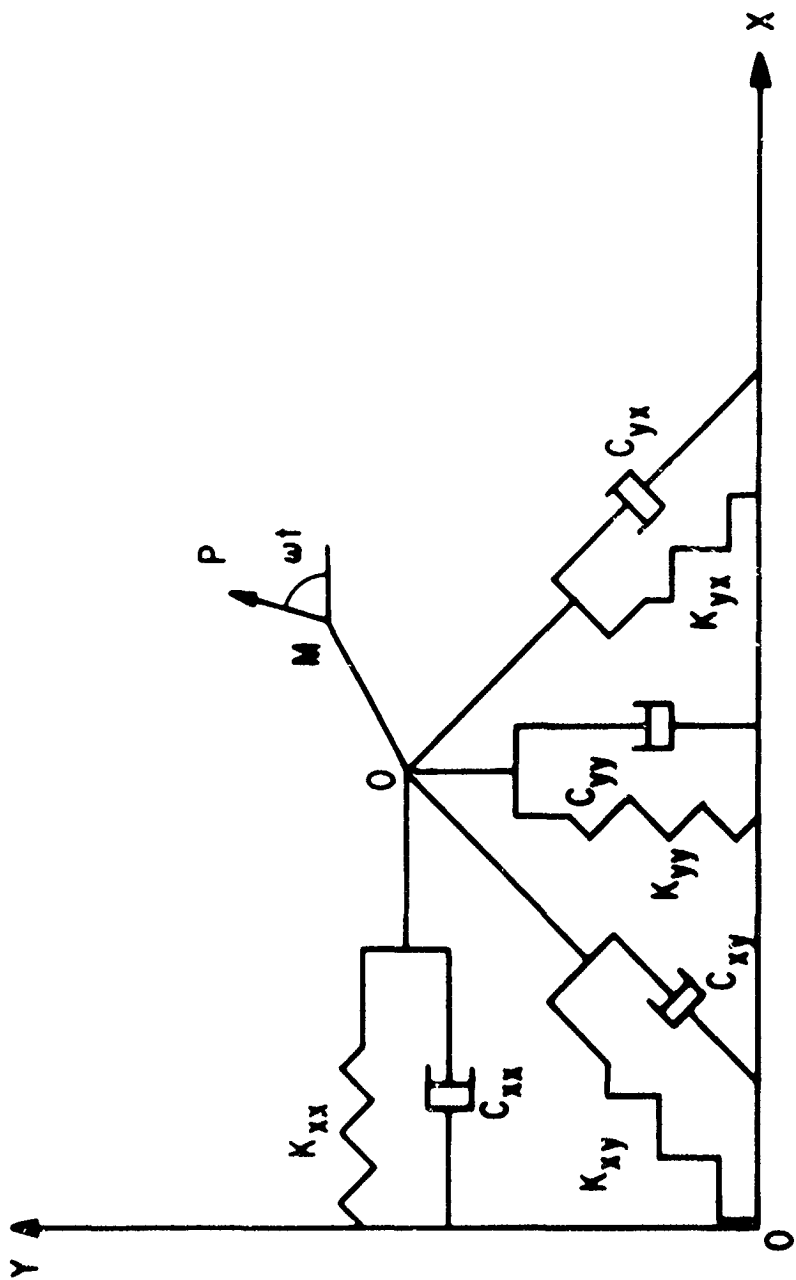


Fig. 56 Schematic Representation of Bearing Dynamic Properties

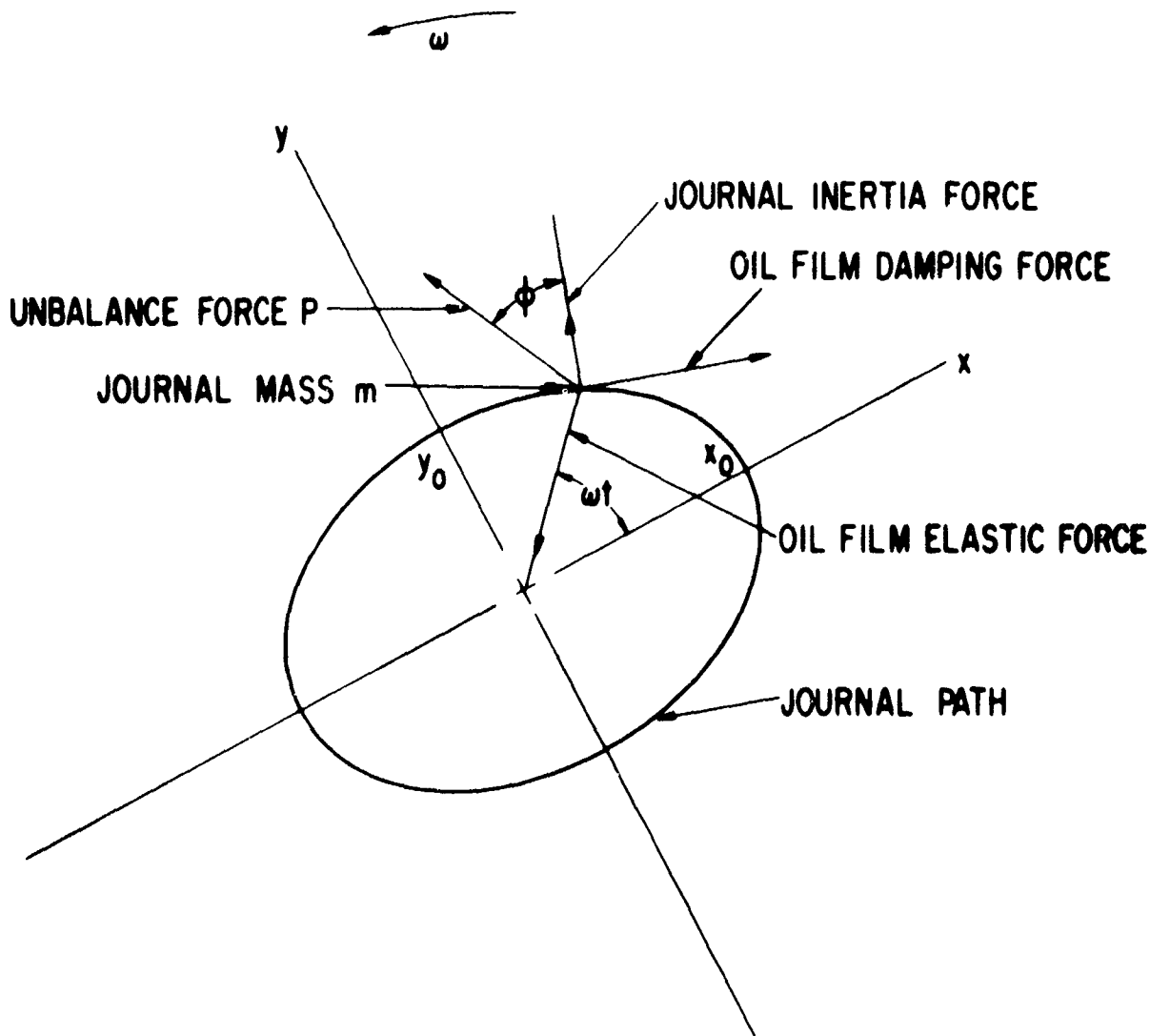


Fig. 57 Typical Shaft Locus Path Showing Force Equilibrium

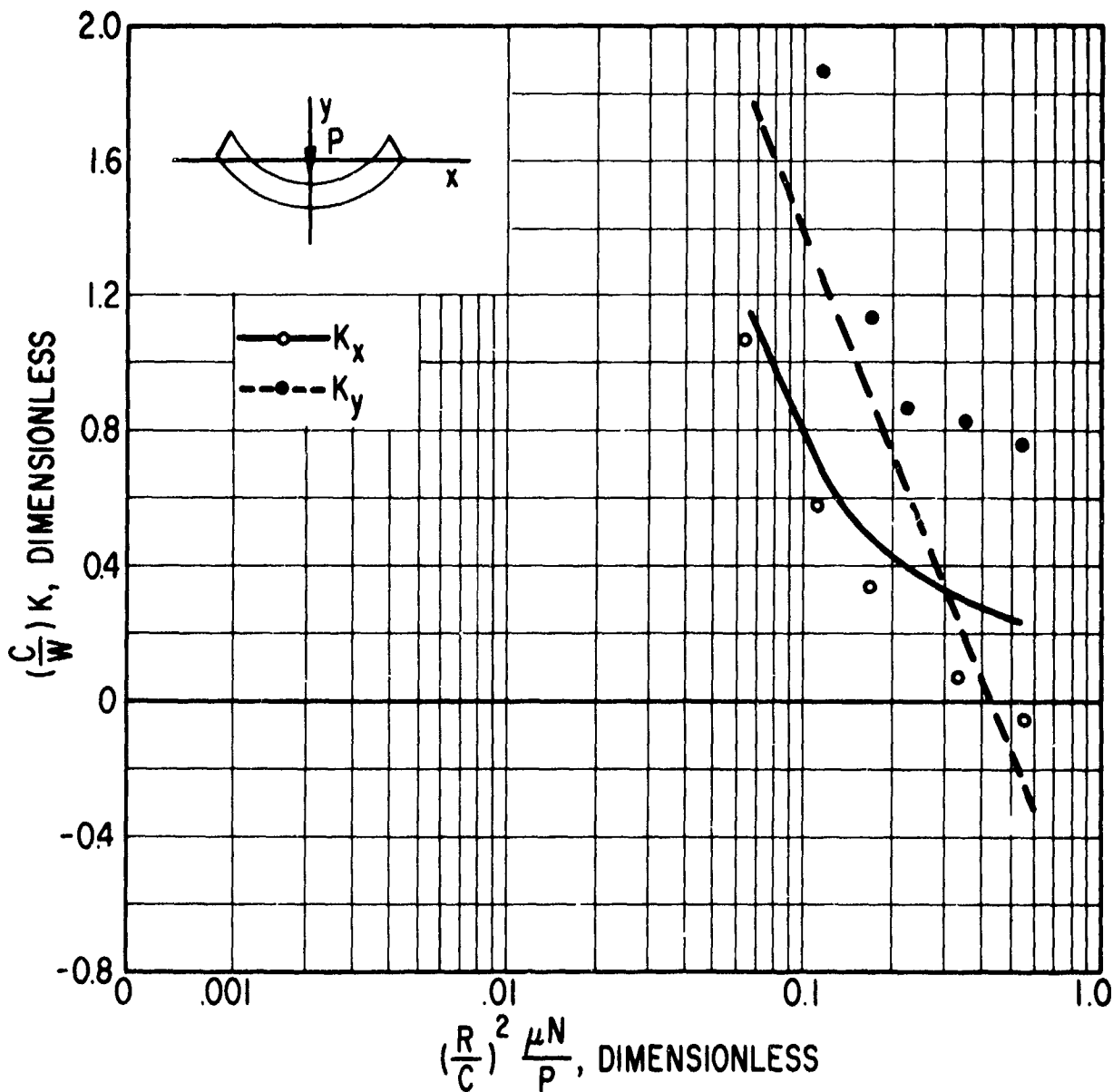


Fig. 58 Laminar Flow Stiffness Coefficients

$C/R = 4 \times 10^{-3}$ in/in., $\beta = 100^\circ$

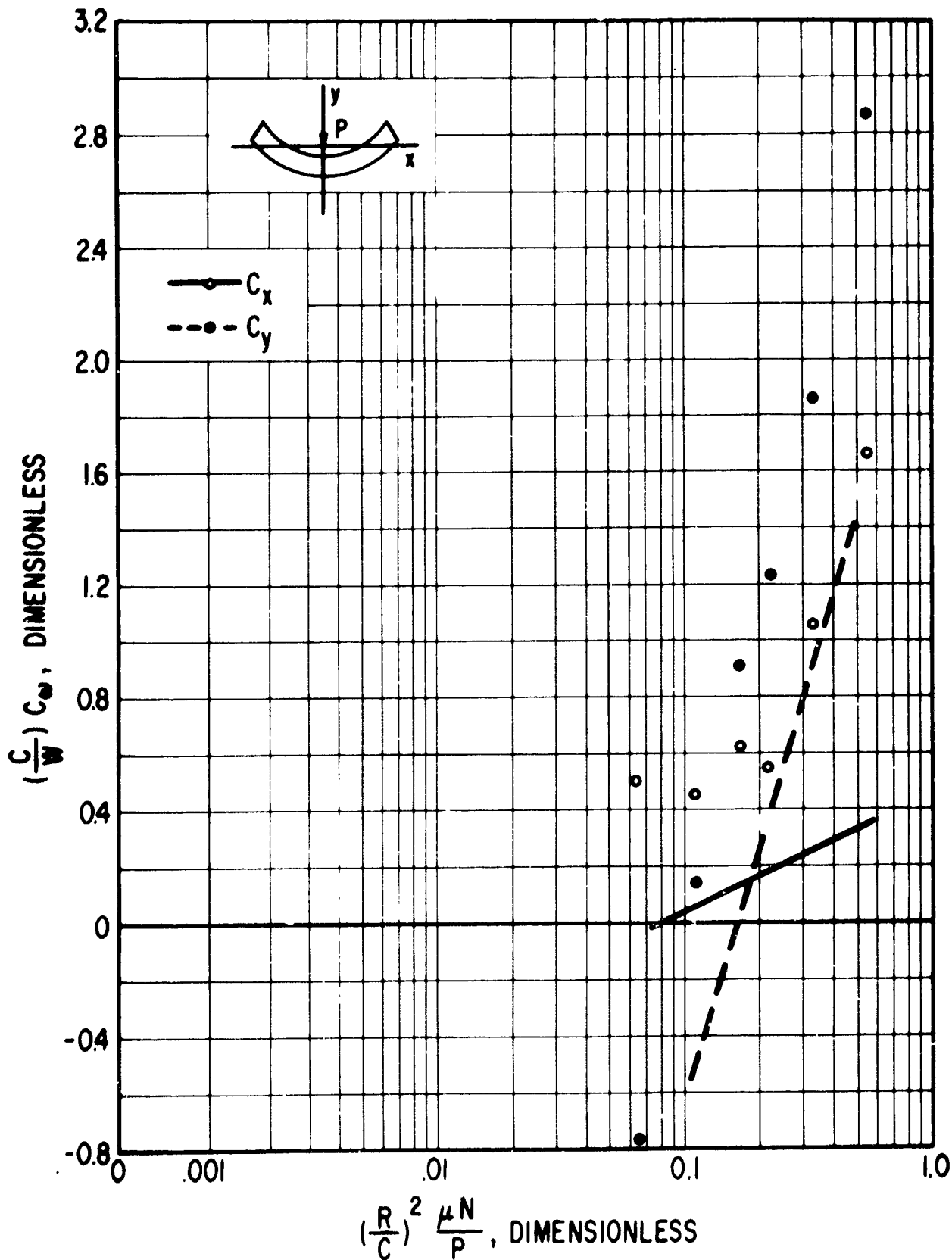


Fig. 59 Laminar Flow Damping Coefficients

$C/R = 4 \times 10^{-3}$ in/in., $\beta = 100^\circ$

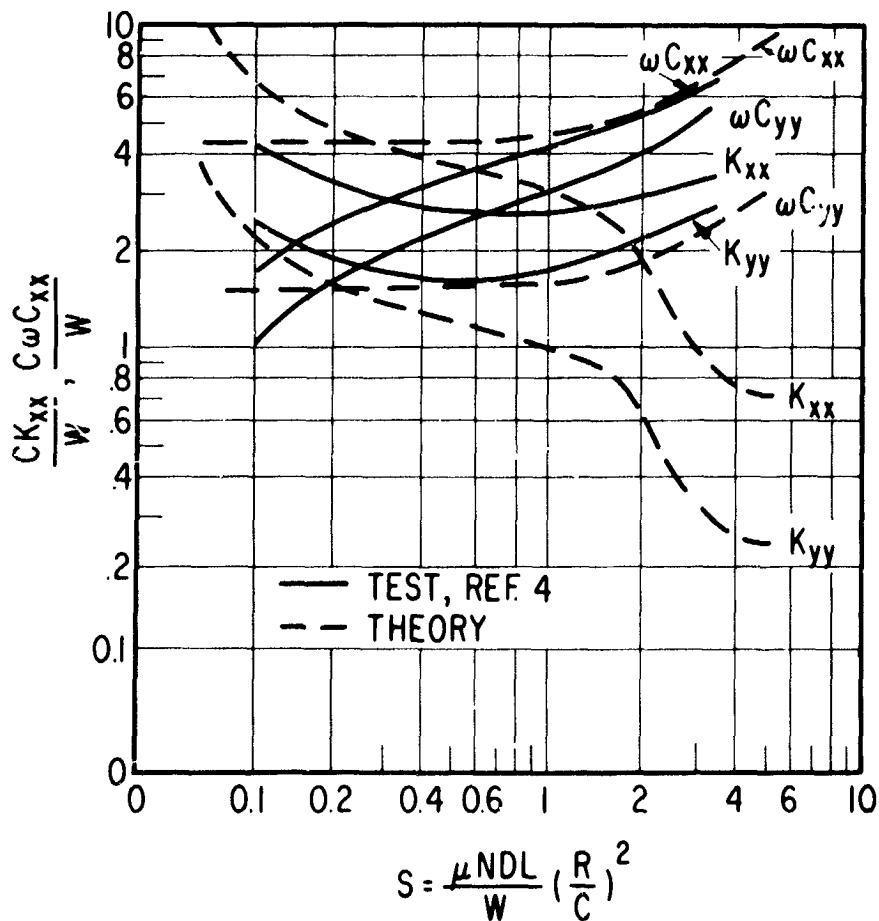


Fig. 60 Comparison of Experimental and Theoretical Dynamic Properties in Laminar Flow Regime from Ref. 2

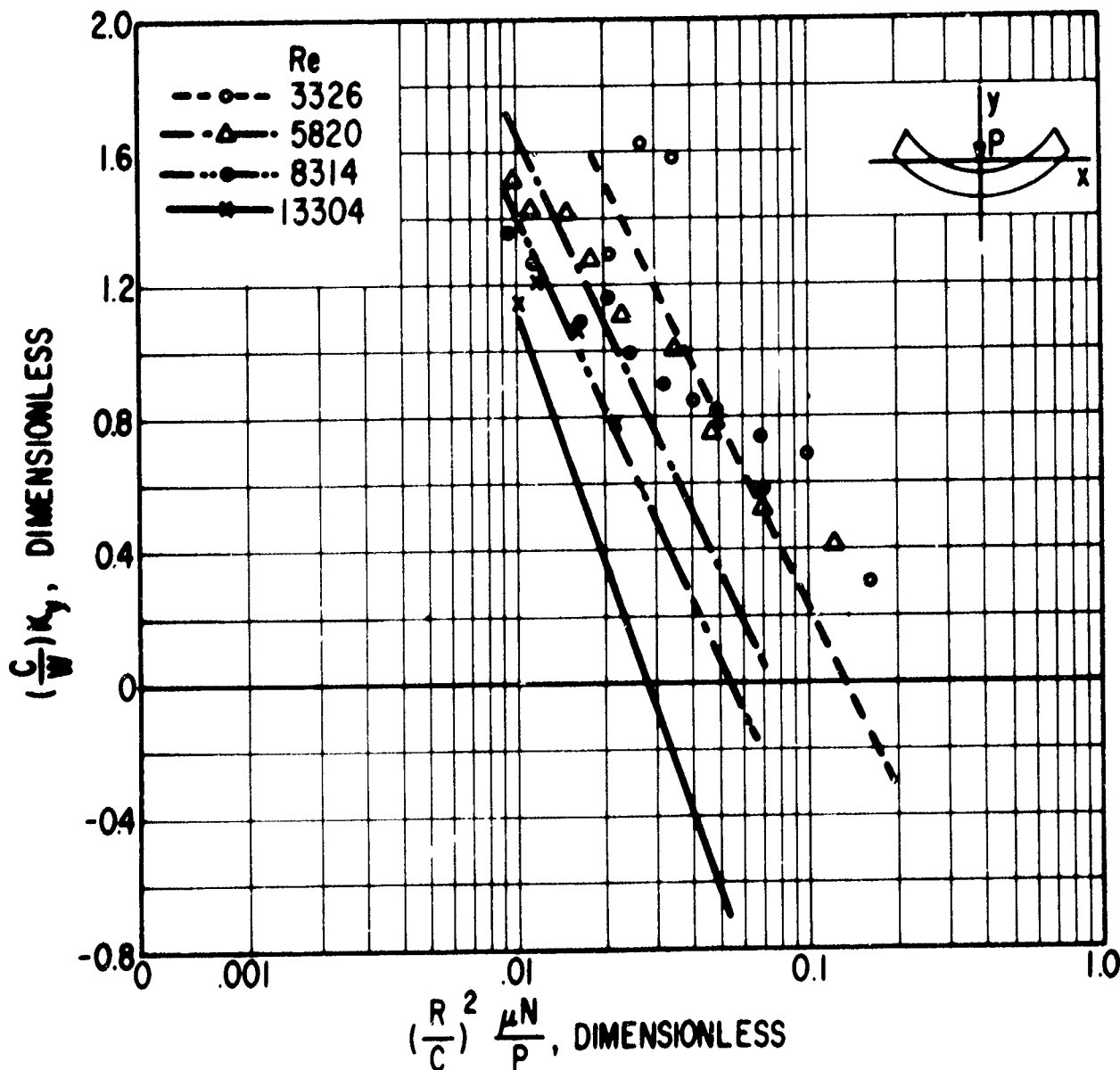


Fig. 61 Stiffness Coefficients in the Vertical Direction
 $C/R = 4 \times 10^{-3}$ in/in., $\beta = 100^\circ$

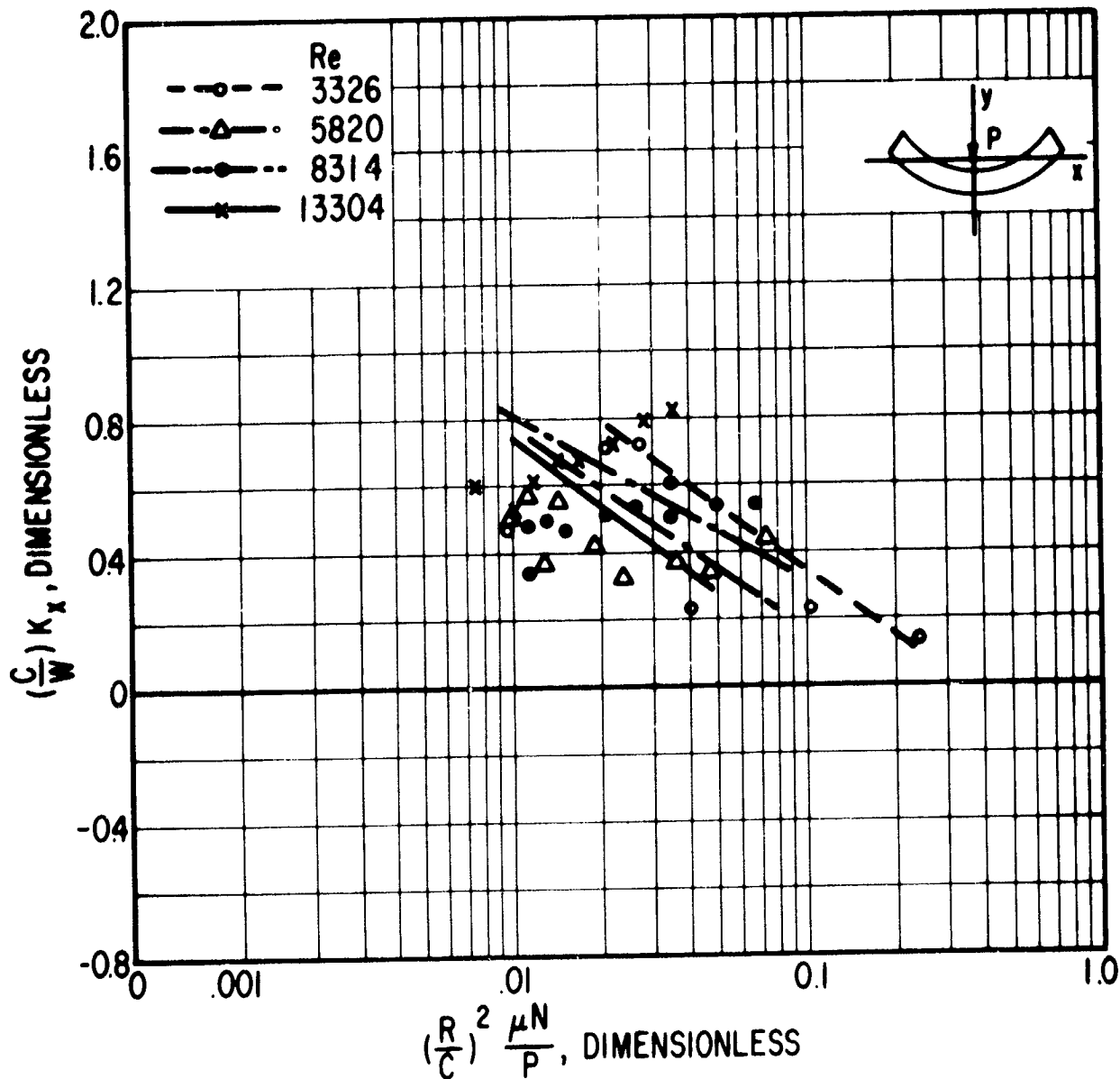


Fig. 62 Stiffness Coefficients in the Horizontal Direction
 $C/R = 4 \times 10^{-3}$ in/in., $\mu = 100^\circ$

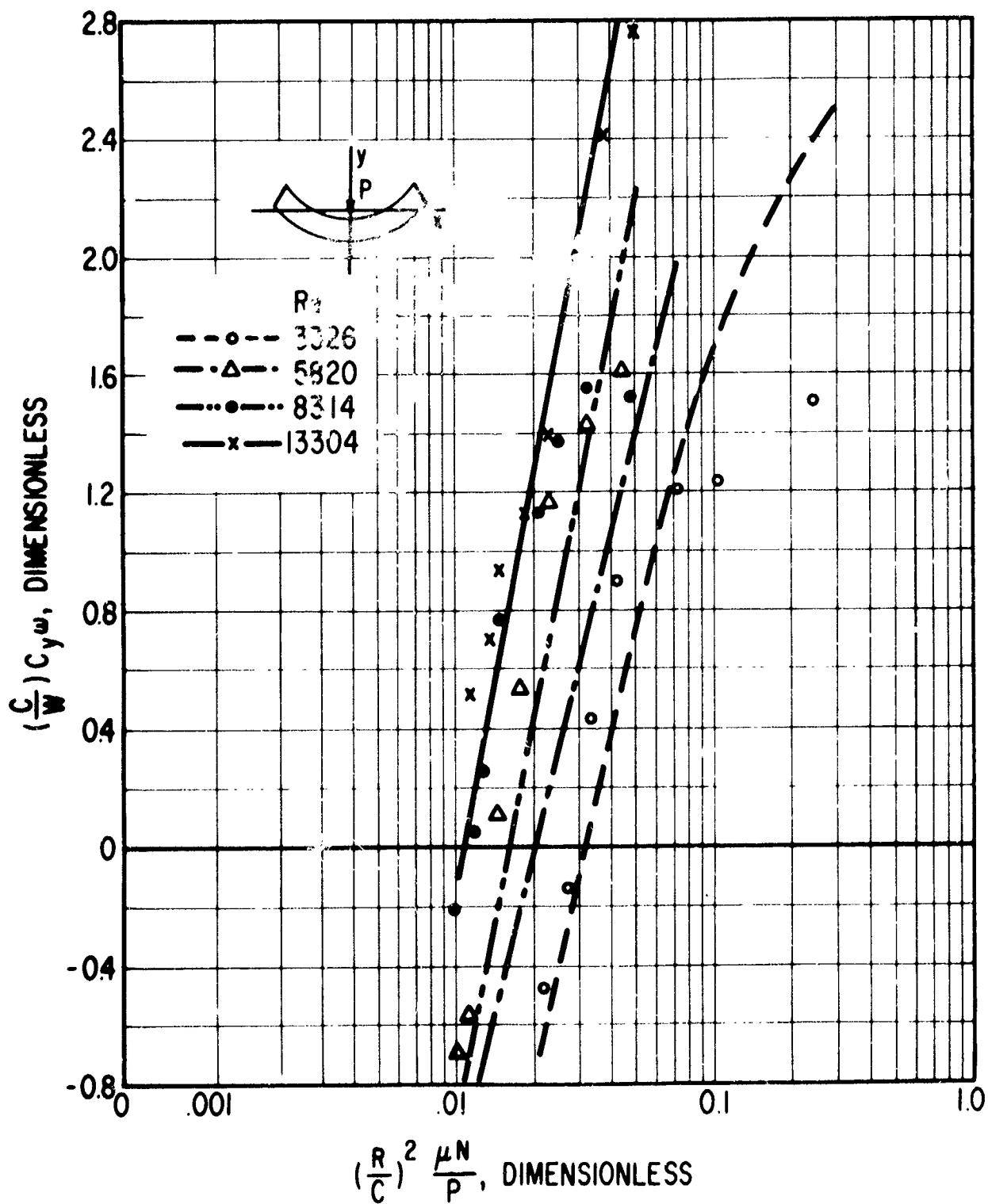


Fig. 63 Damping Coefficients in the Vertical Direction
 $C/R = 4 \times 10^{-3}$ in/in., $\mu = 100^\circ$

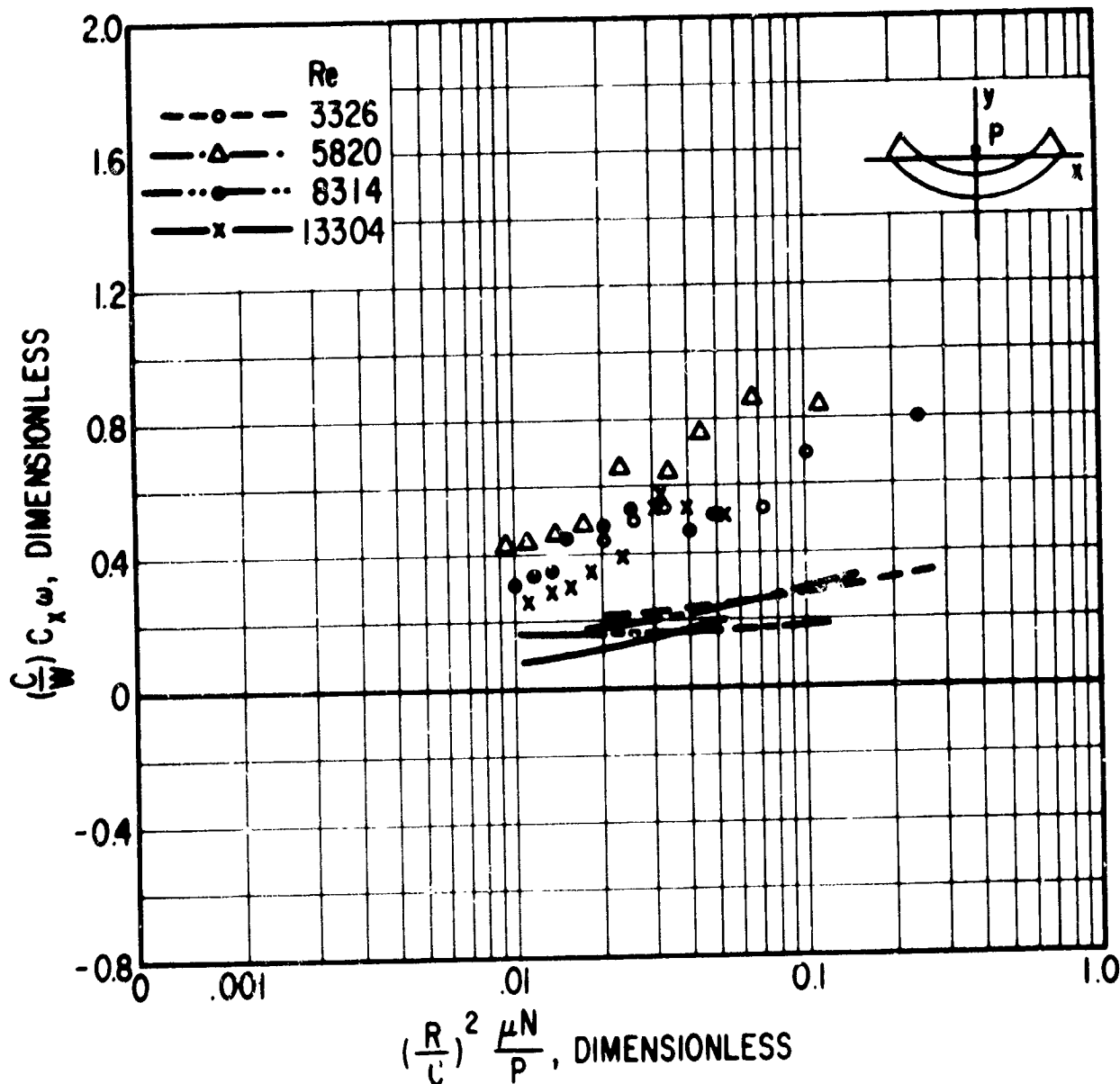


Fig. 64 Damping Coefficients in the Horizontal Direction
 $C/R = 4 \times 10^{-3}$ in/in., $\alpha = 100^\circ$

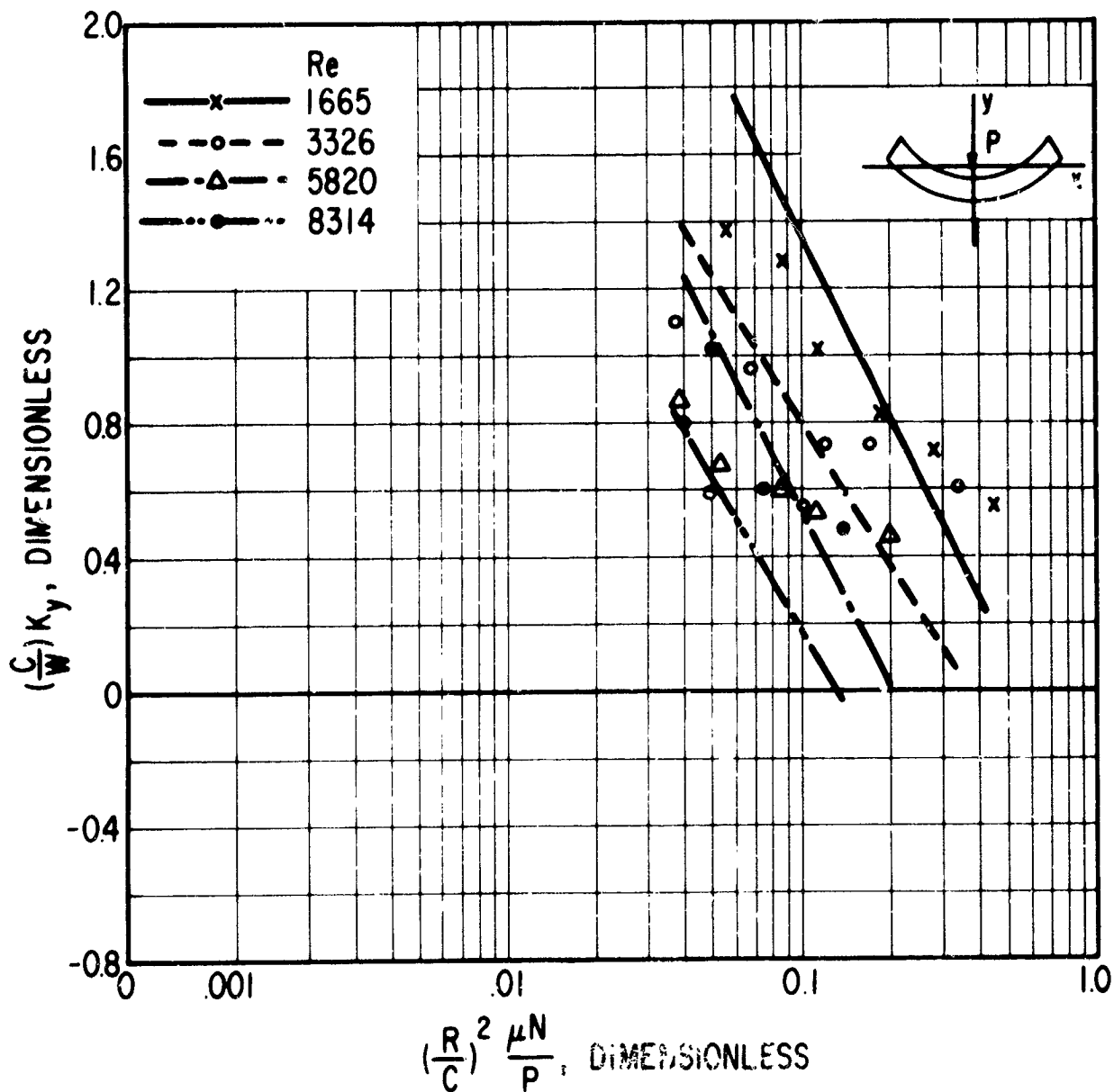


Fig. 65 Stiffness Coefficient in the Vertical Direction
 $C/R = 2 \times 10^{-3}$ in/in., $\mu = 100^\circ$

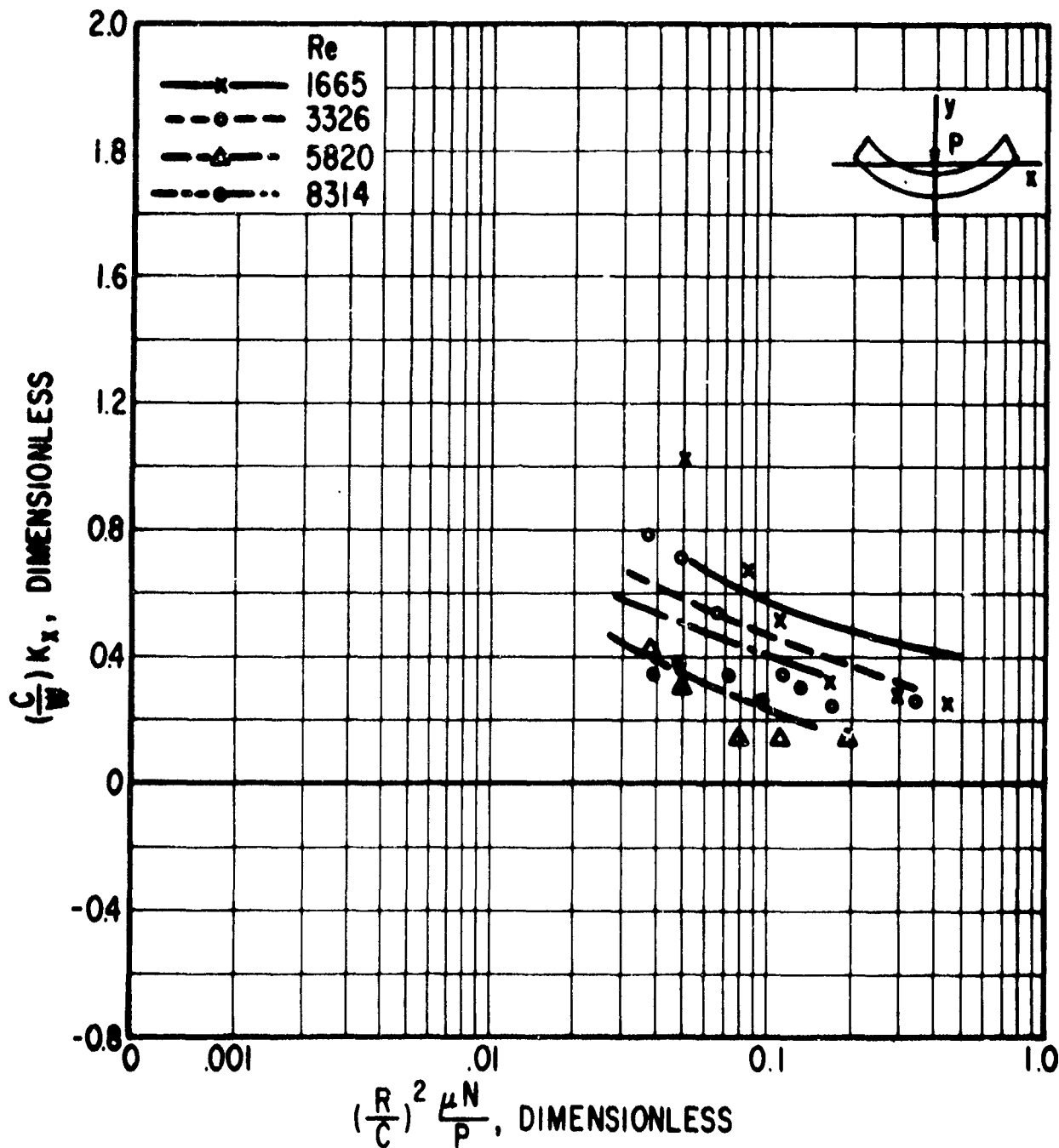


Fig. 66 Stiffness Coefficient in the Horizontal Direction
 $C/R = 2 \times 10^{-3}$ in/in., $\beta = 100^\circ$

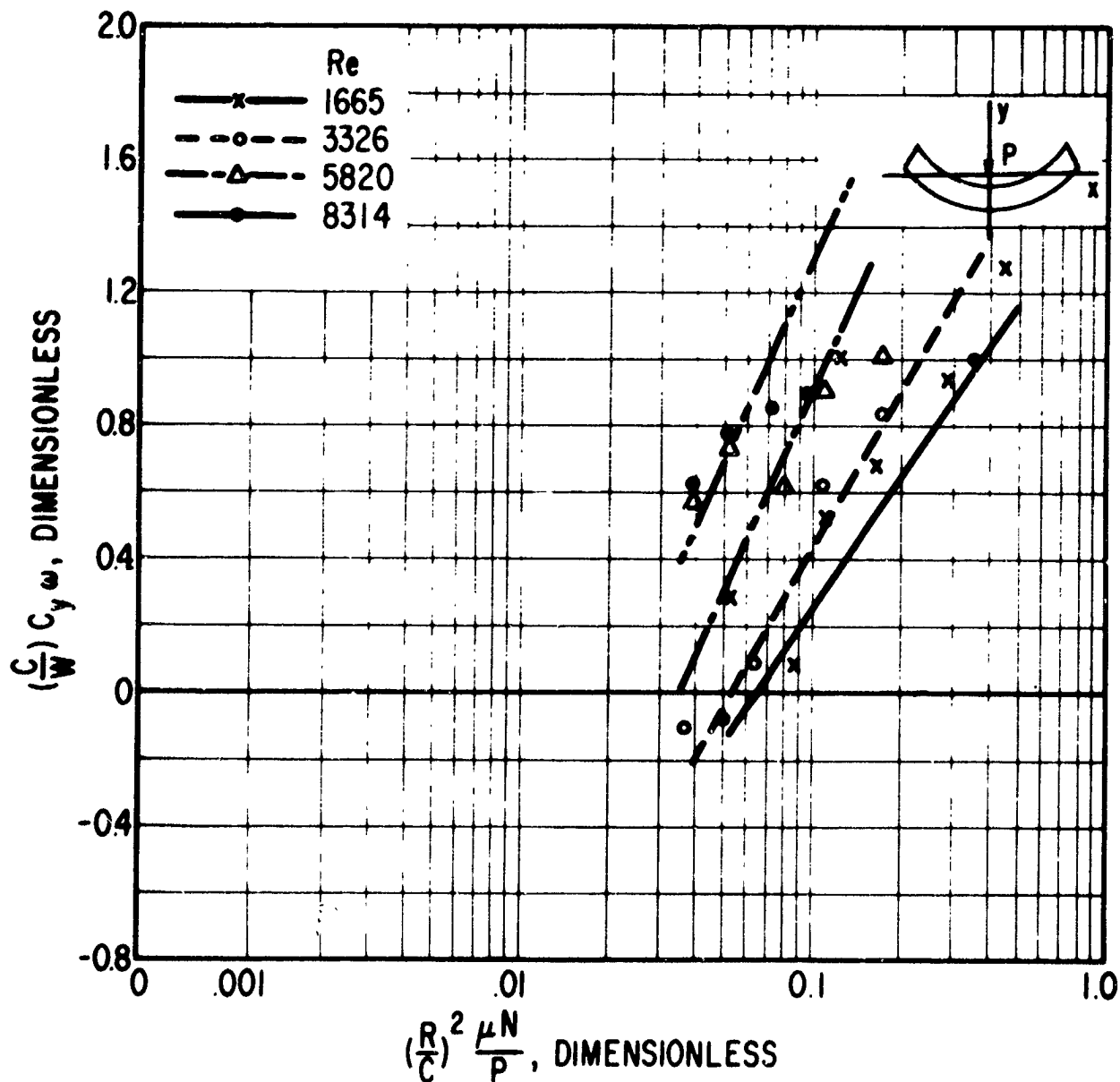


Fig. 67 Damping Coefficients in the Vertical Direction
 $C/R = 2 \times 10^{-3}$ in/in., $\alpha = 100^\circ$

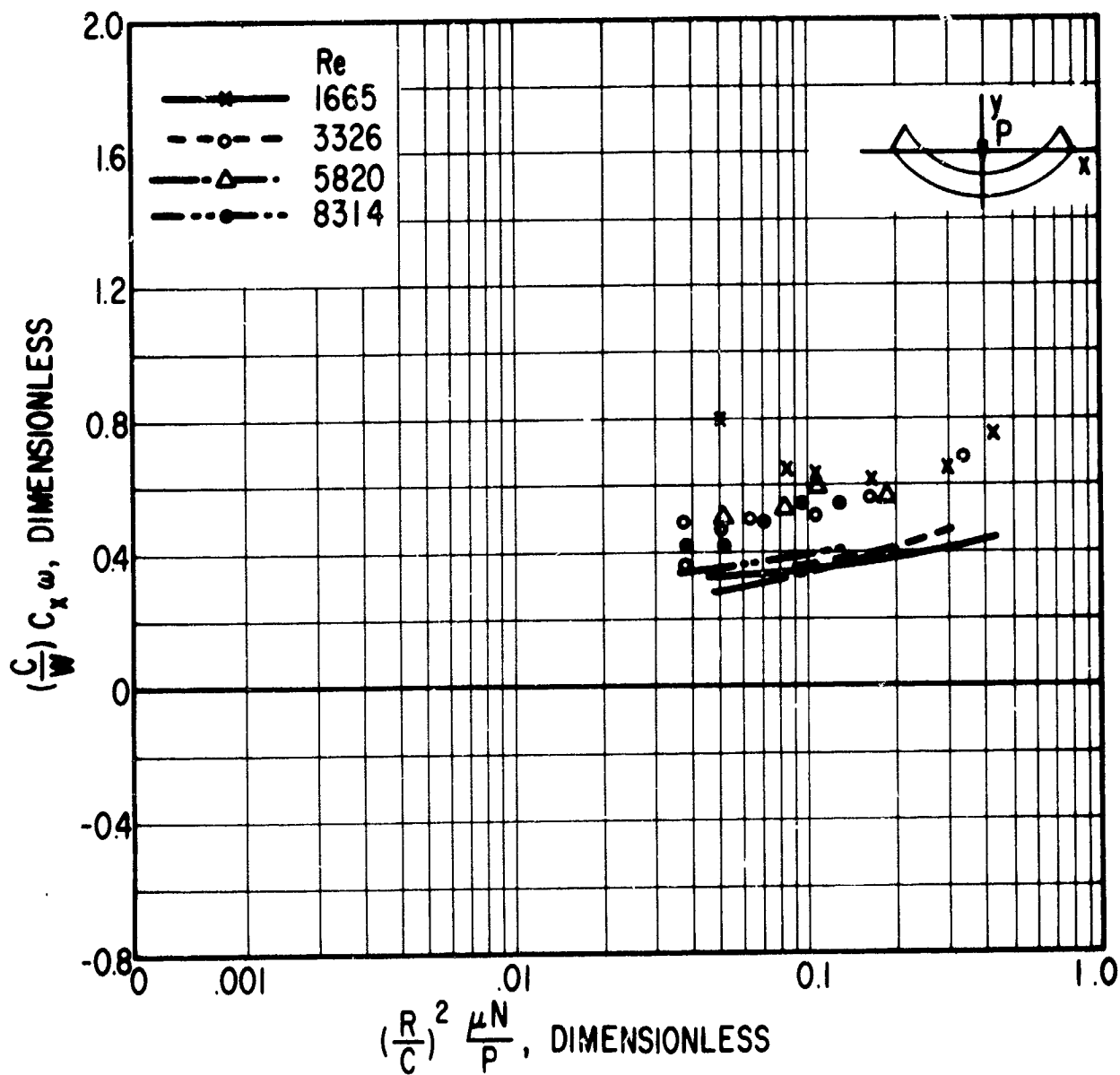


Fig. 68 Damping Coefficients in the Horizontal Direction
 $C/R = 2 \times 10^{-3}$ in/in., $\beta = 100^\circ$

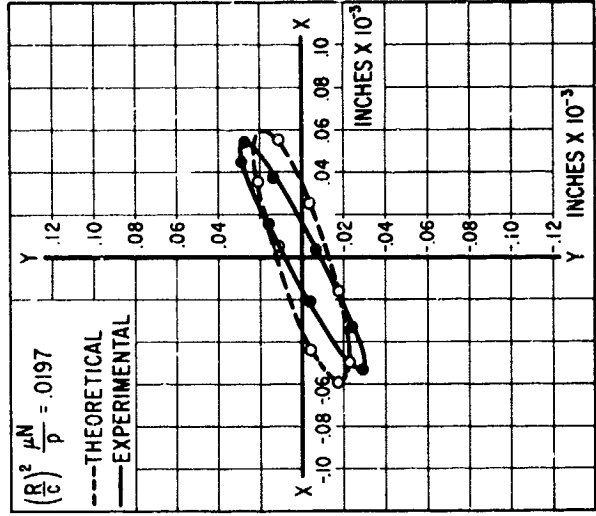
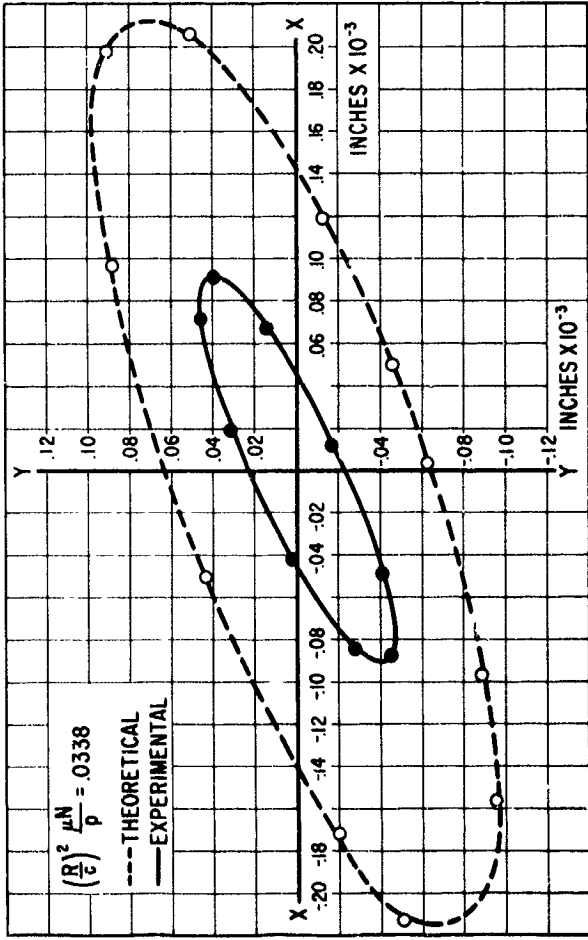
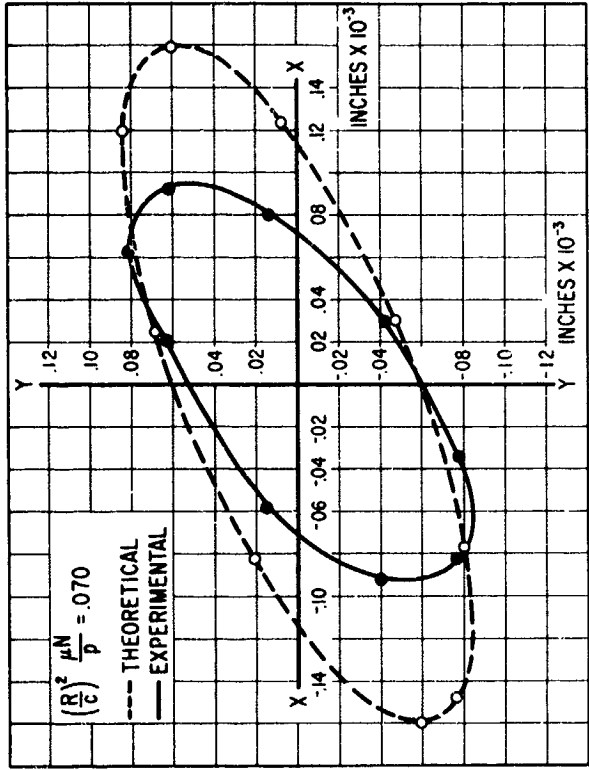
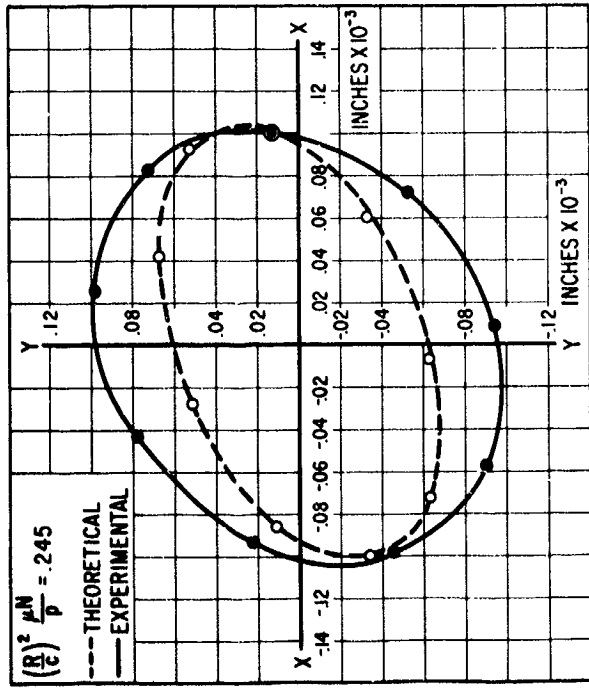


Fig. 69 Shaft Response as Determined from Theory and by Experiment

$C/R = 4 \times 10^{-3}$ in./in., $\beta = 100^\circ$, $Re \approx 3326$

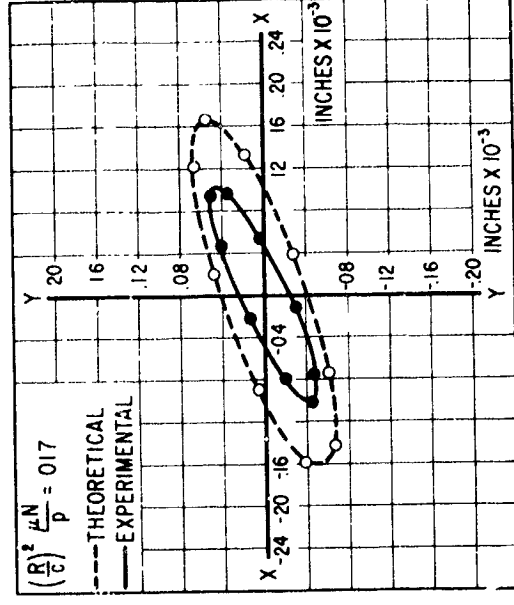
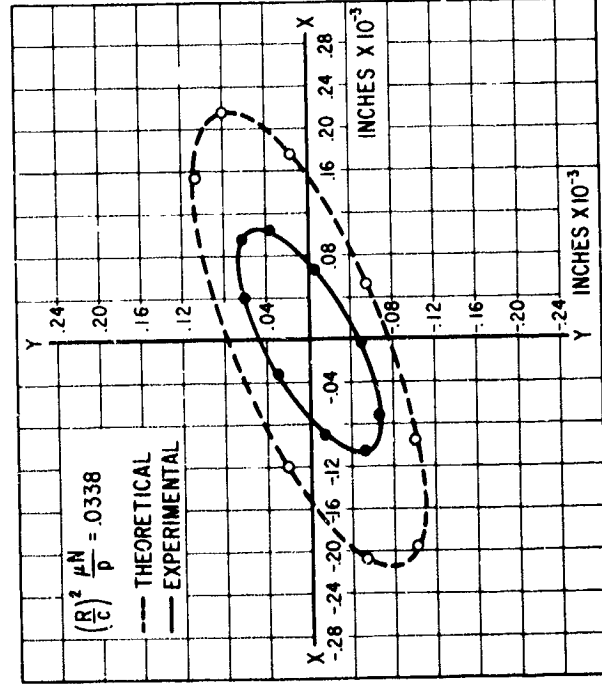
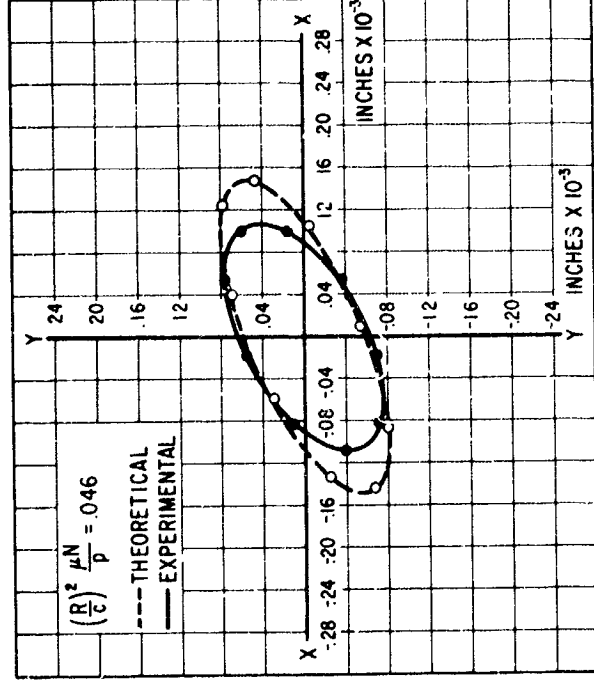
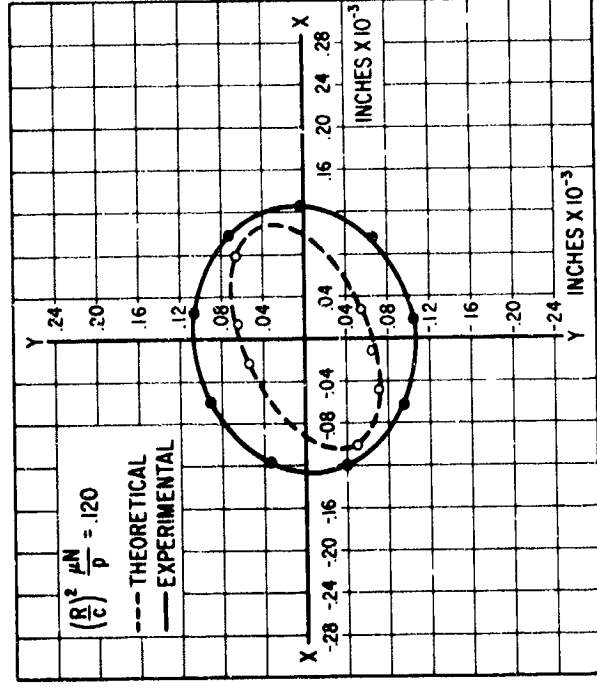


Fig. 70 Shaft Response Determined from Theory and by Experiment

$C/R = 4 \times 10^{-3}$ in/in., $\phi = 100^\circ$, $Re = 5820$

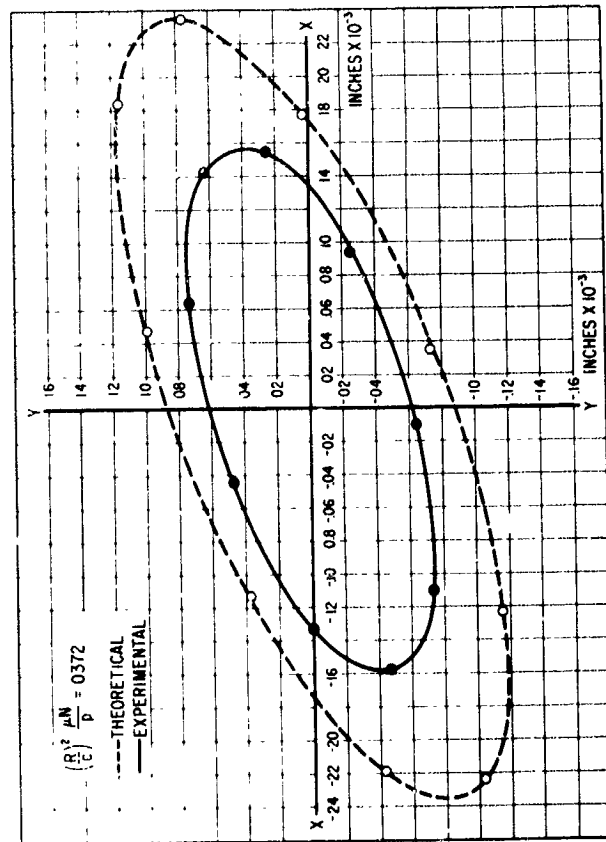
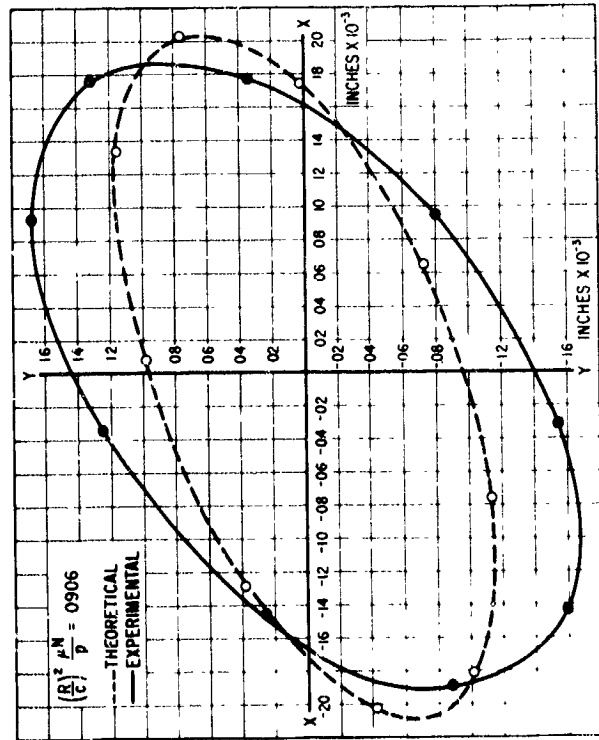
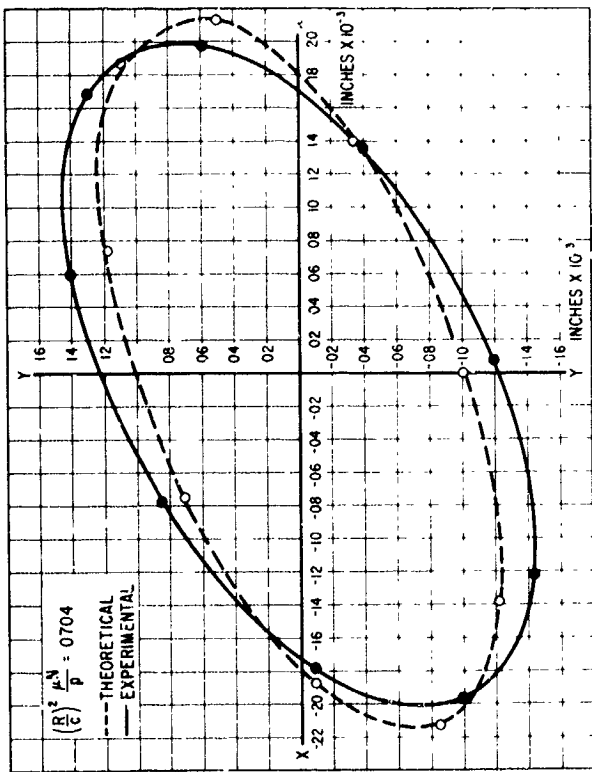


Fig. 71 Shaft Response as Determined from Theory and by Experiment
 $C/R = 2 \times 10^{-3}$ in/in., $\beta = 100^\circ$, $Re = 8314$

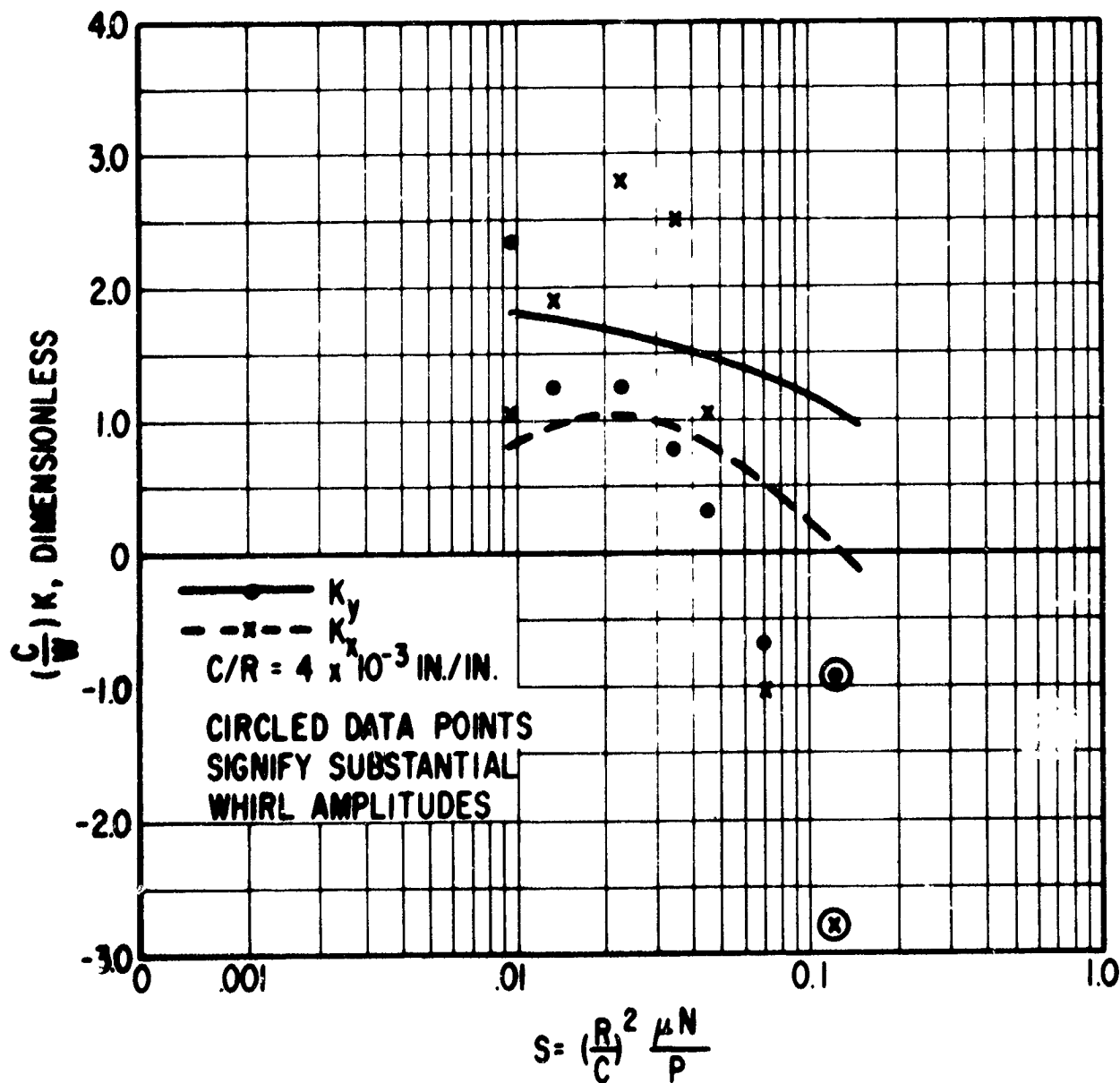


Fig. 72 Stiffness Coefficients - $Re = 5820$, $\beta = 360^\circ$

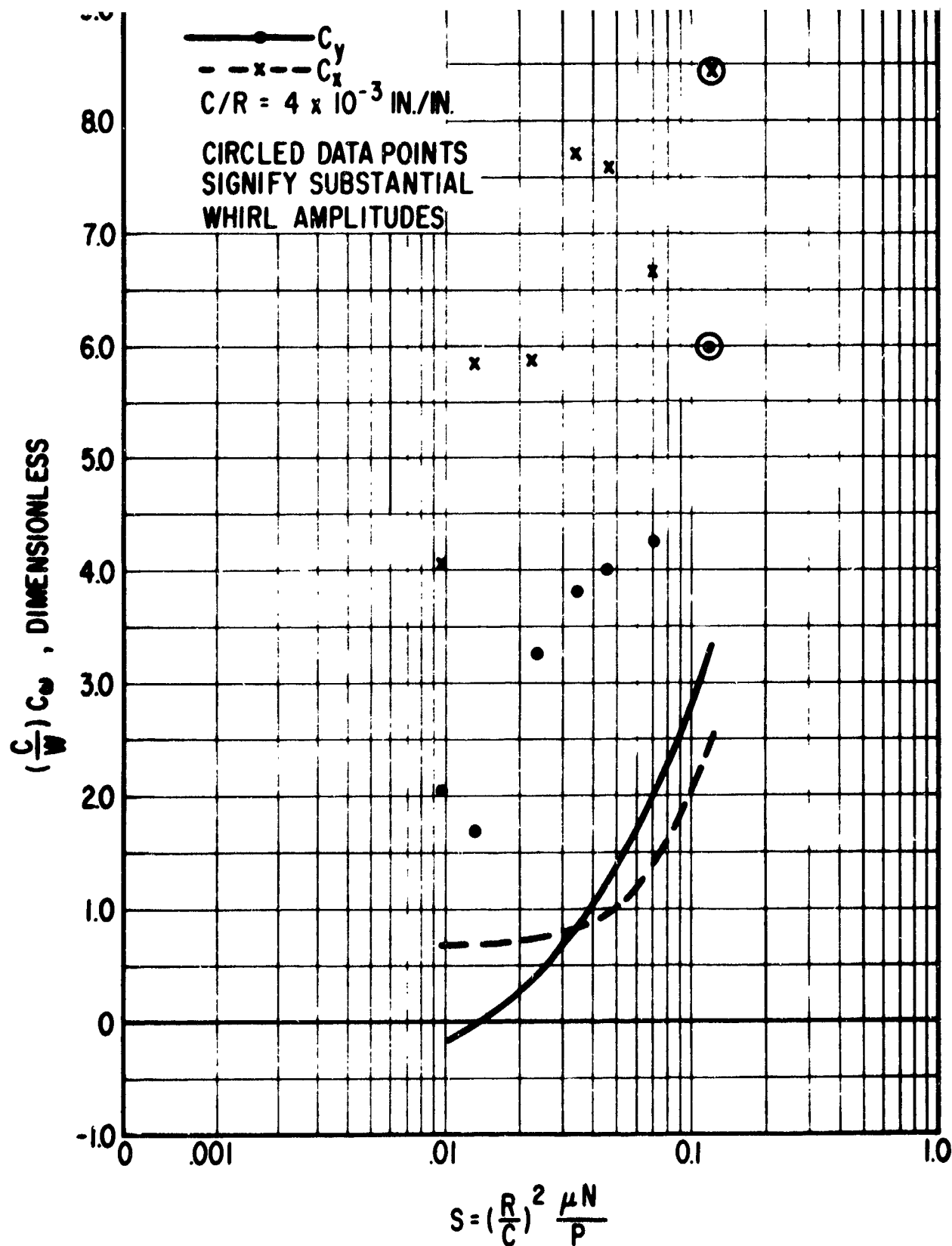


Fig. 73 Damping Coefficients - $Re = 5820$, $\beta = 360^\circ$

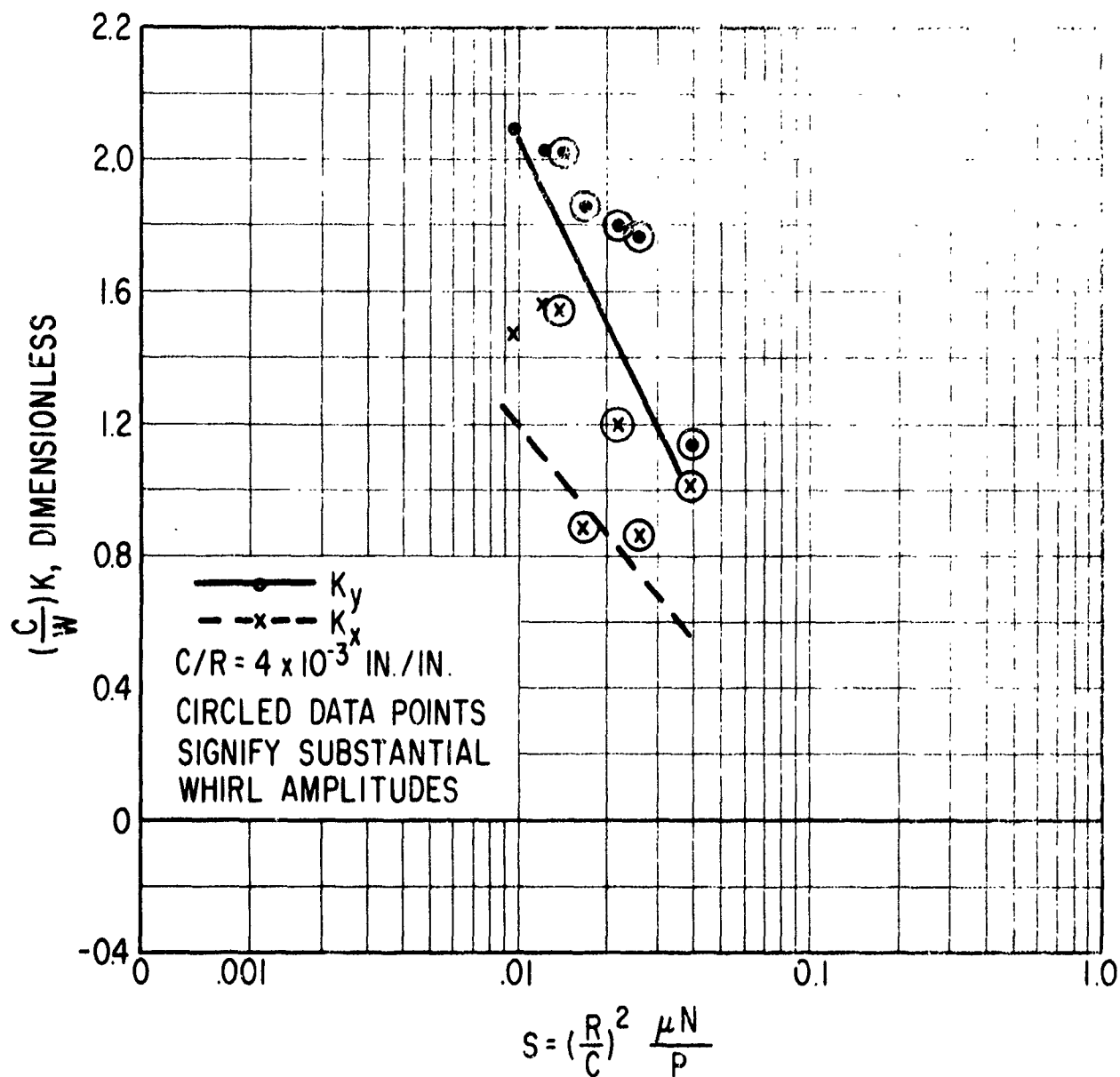


Fig. 74 Stiffness Coefficients - $Re = 13,303$, $\beta = 360^\circ$

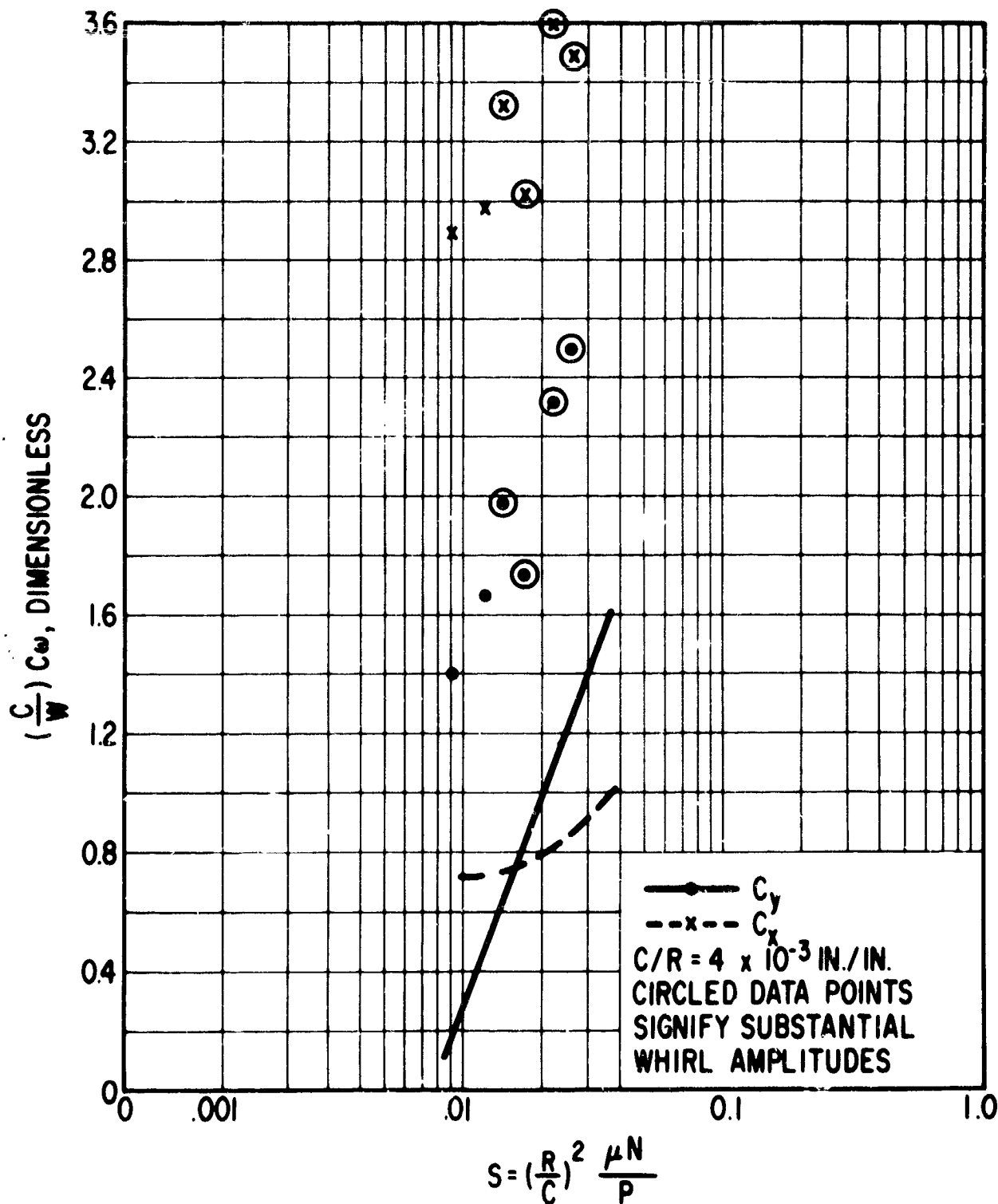


Fig. 75 Damping Coefficients - $Re = 13,303$, $\beta = 360^\circ$

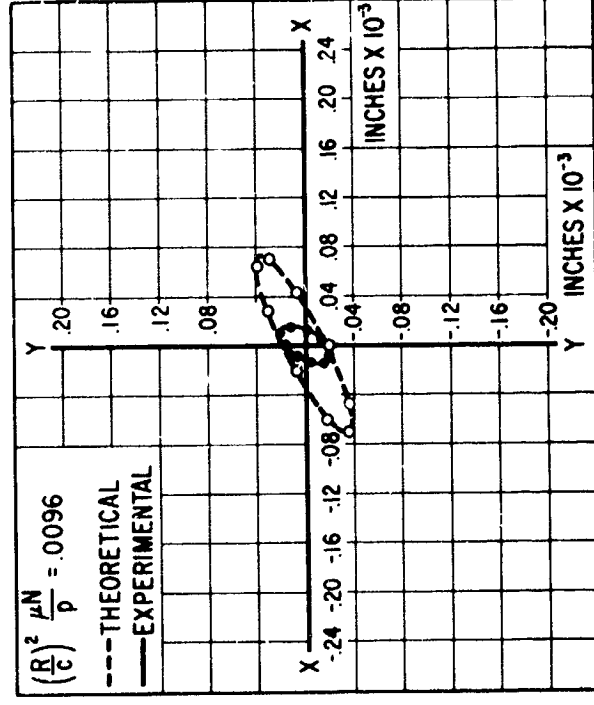
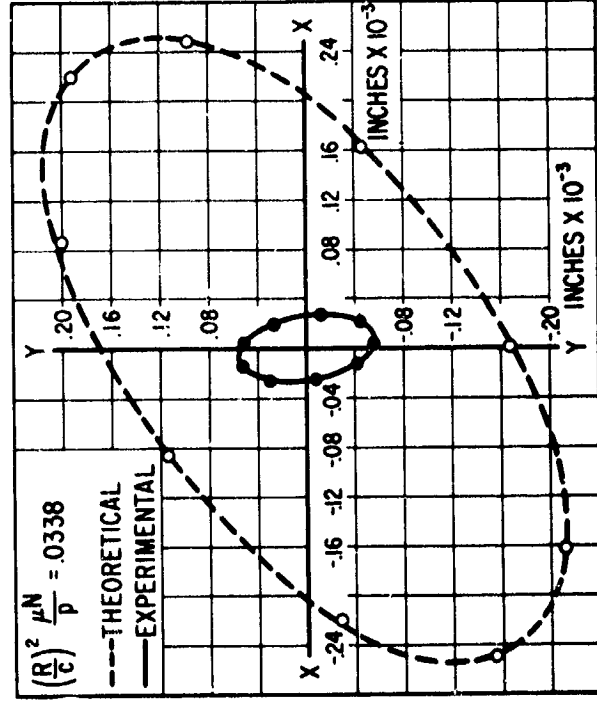
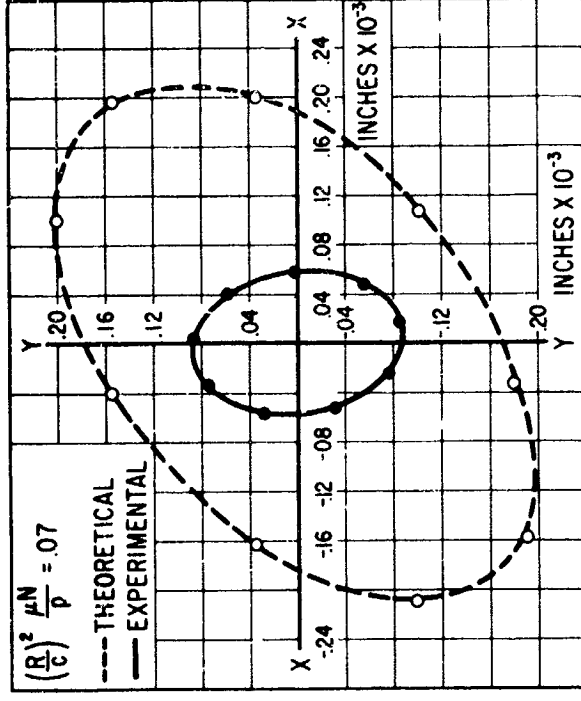
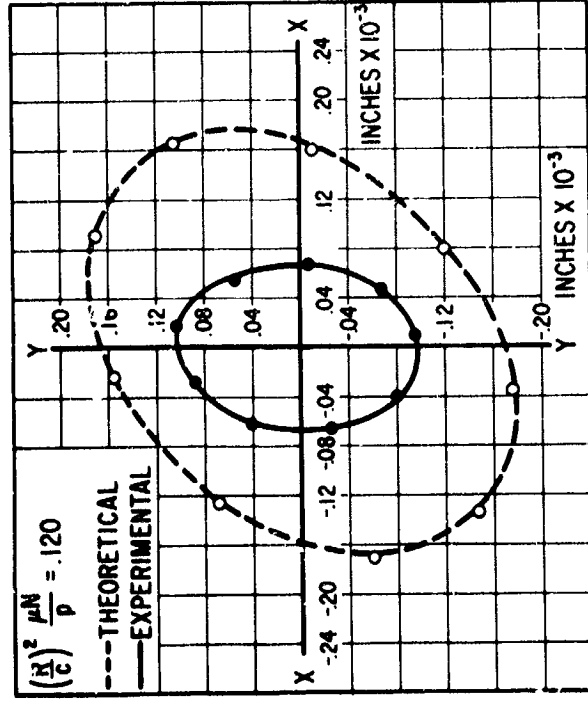


Fig. 76 Shaft Response as Determined from Theory and by Experiment



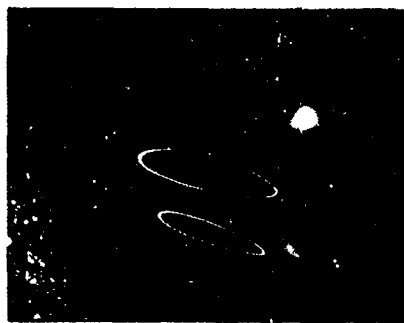
(a) 53 lb load, Shaft and Load Rotate CCW



(b) 53 lb load, Shaft Rotates CW Load, CCW



(c) 172 lb load, Shaft and Load Rotate CCW



(d) 172 lb load, Shaft Rotates CW Load, CCW

Fig. 77 Oscilloscope Photographs of Shaft Response with Forward and Counter Rotating Load. Two separate orbits are shown for counter rotation representing the extremes of a beat effect.

Speed = 3500 rpm (5820 Re), $\beta = 100^\circ$, $C/R = 4 \times 10^{-3}$ in/in., 1 Large Division = $.53 \times 10^{-3}$ inches.

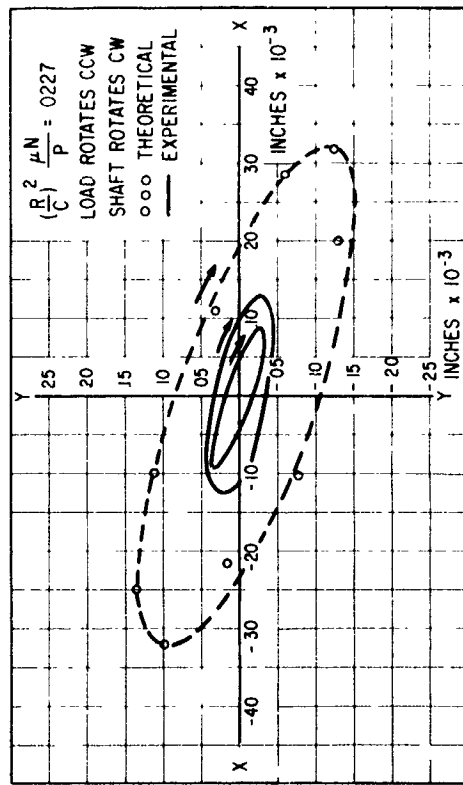
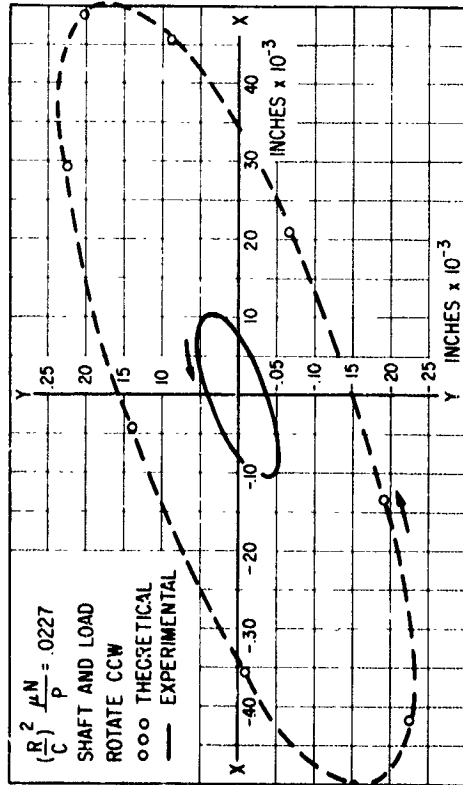
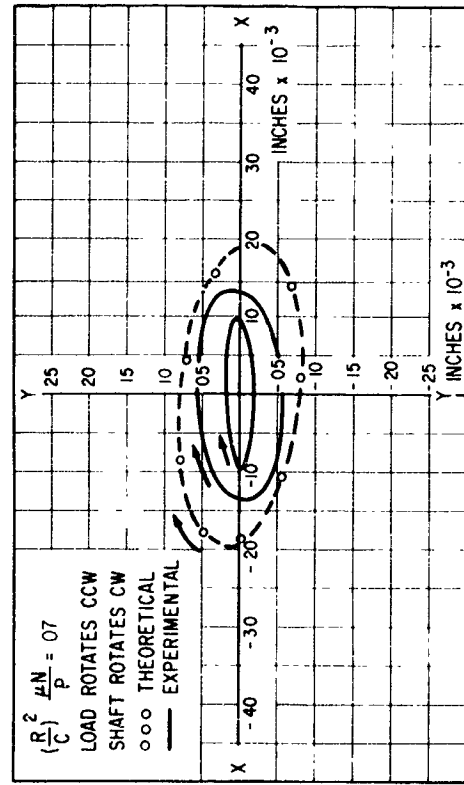
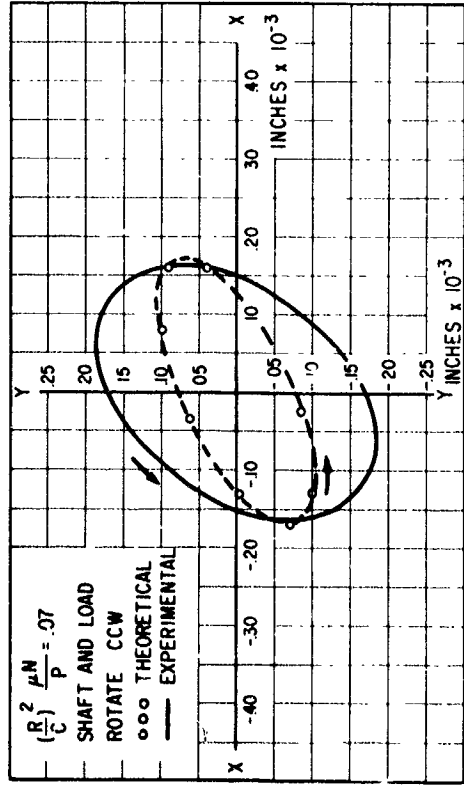


Fig. 78 Shaft Response for Forward and Counter Rotating Load as Determined by Theory and Experiment

$C/R = 4 \times 10^{-3}$ in/in., $\beta = 100^\circ$, Speed = 3500 rpm (5820 Re)

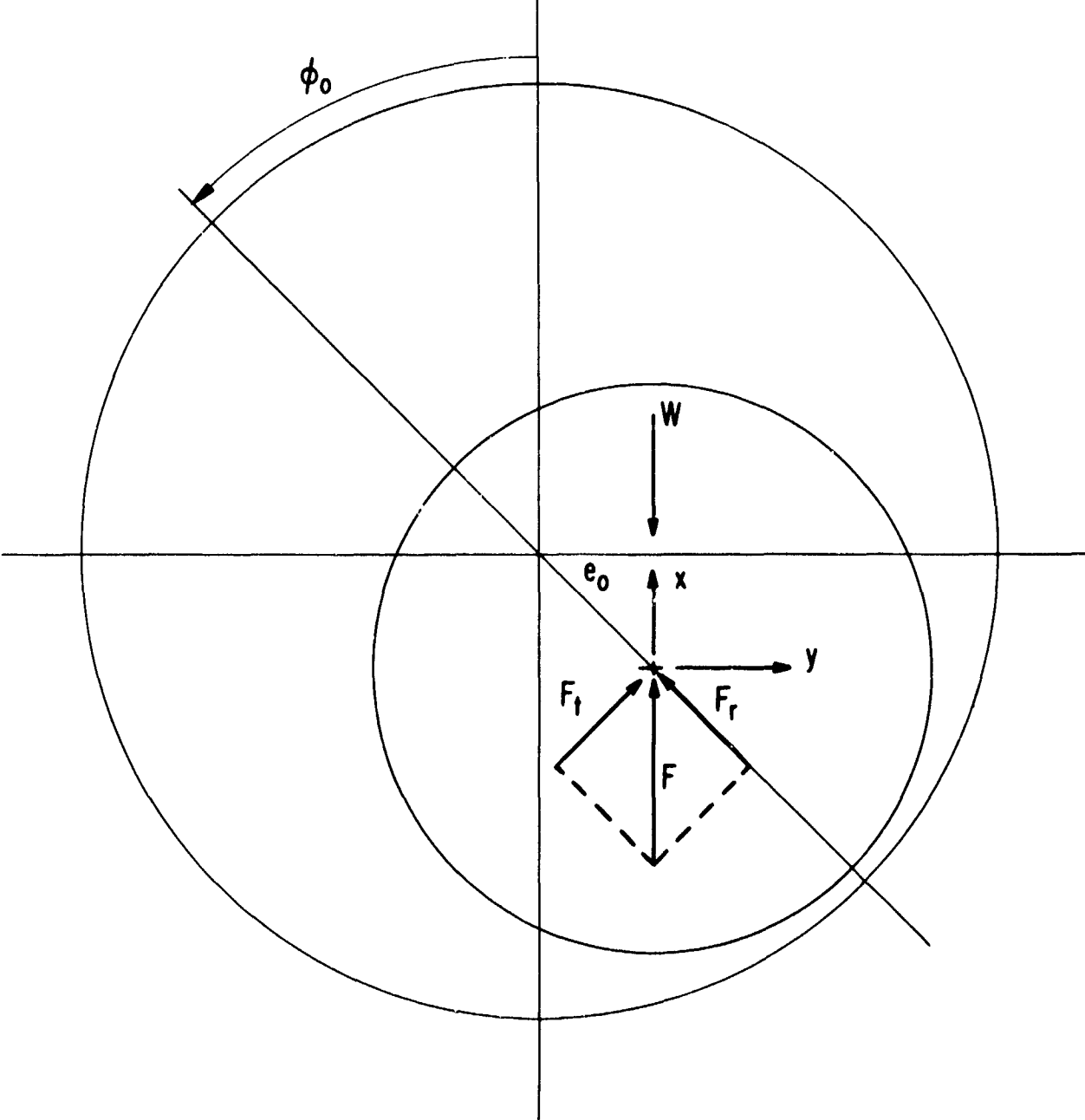


Fig. 79 Coordinate System

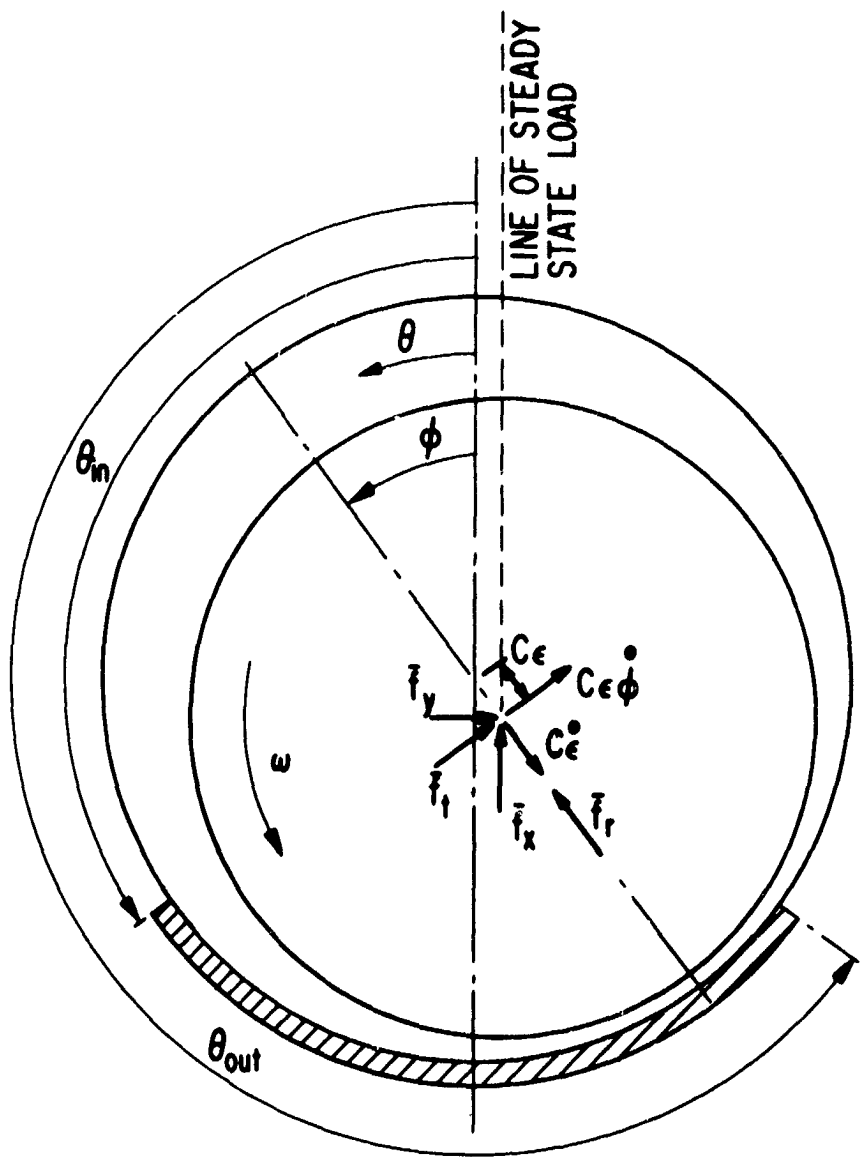


Fig. 80 Bearing Arc Nomenclature

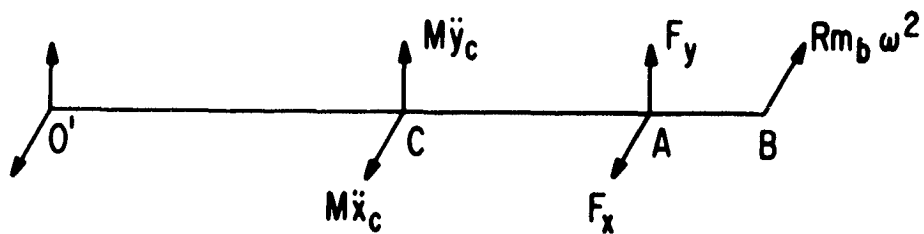


Fig. 81 Forces Acting on Experimental Rotor